UiT THE ARCTIC UNIVERSITY OF NORWAY

Faculty of Science and Technology
Department of Physics and Technology

Radar observations of space debris in polar orbits 2018–2021

A study on the evolution of the Microsat-R fragments

—

Martinius Ekeland Paulsen
FYS-3931 Master thesis in space physics 30 SP . . . July 2021

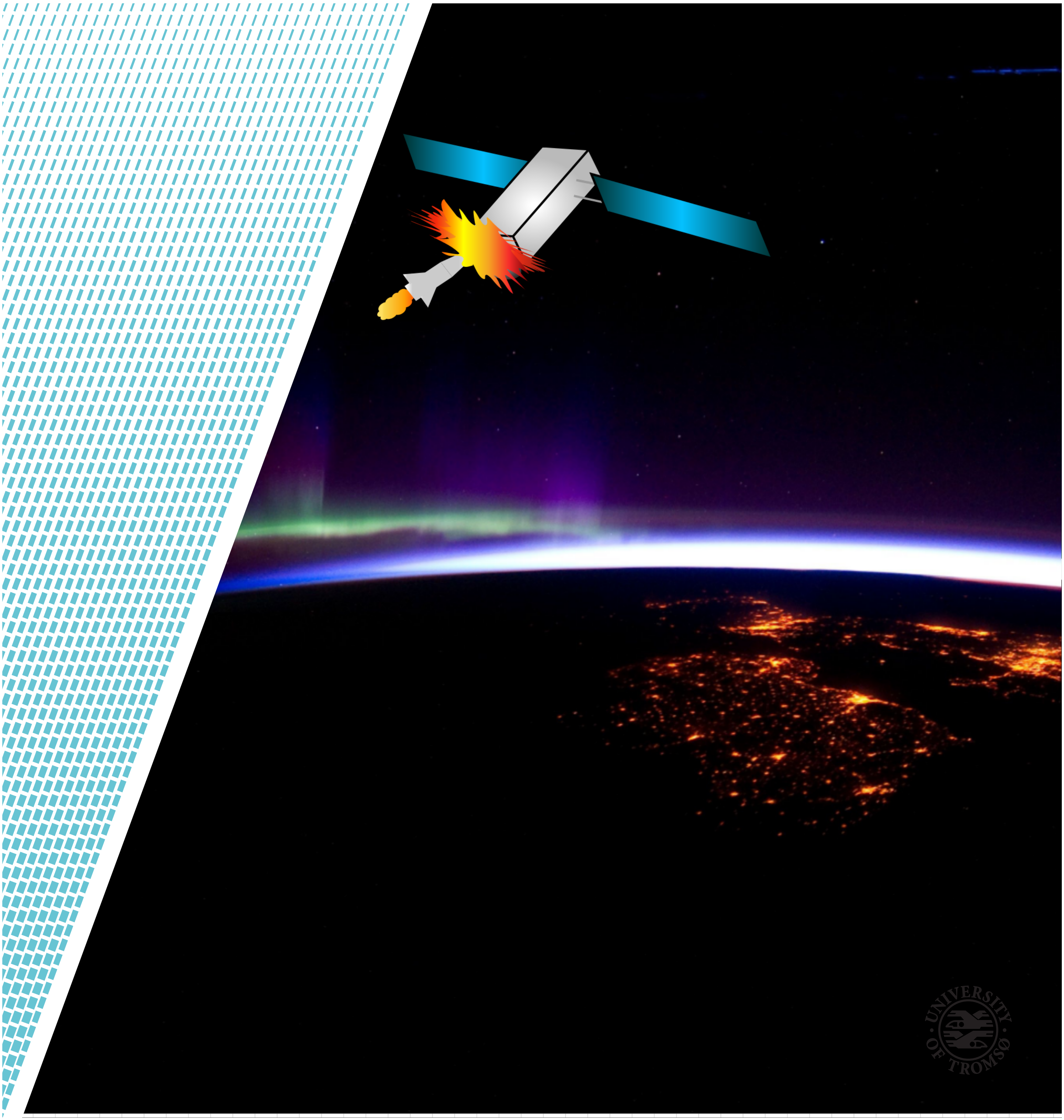

“Our problem is not that we aim too high and miss,
but that we aim too low and hit.”
–Aristotle

“There is nothing permanent except change.”
–Heraclitus

Abstract

Orbits are an invaluable resource for the global community. However, space pollution is becoming more pronounced as the accumulation of debris continues. Deliberate collisions are a relevant source contributing to this development. When *Microsat-R* was destroyed with a missile in 2019, it ejected numerous fragments into orbit. Based on observations made with EISCAT UHF, this thesis will investigate the evolution of this debris cloud. This is achieved using the results from four different measurement campaigns from 2018 to 2021.

Preface

When I started on this thesis, I had the ambition that it should be readable to everyone who master the English language – both dedicated scientists, and people encountering the subject for the first time. As to follow up this philosophy, I have used analogies as a tool to describe complex concepts that can be difficult to understand. The purpose of the analogies is to inform, rather than distract, while keeping the subject of conversation intact. Hopefully they will not come across as digressions. If anyone reading this thesis finds the topic of space debris half as interesting as I do, I would consider my intention to be accomplished.

Acknowledgements

This thesis would not have been finalized without the help obtained from several people. In an attempt to express my gratitude, this section is dedicated to you. First and foremost I want to thank my supreme supervisor Juha Vierinen for all great help you have provided me with the last year, and for opening the gateway into such an intriguing research area. Your ability to explain difficult concepts in a simplified, and enthusiastic way is unique. Thanks for always motivating me, particularly in periods when progression halted. It has been inspirational to work with you.

A big thanks goes out to Daniel Kastinen, for exceptional help with the correlation process of the thesis. In addition to being acquainted with the brilliant SORTS-program, I am grateful for the helpful discussions we had on Slack. Your assistance has been of essential importance.

Thanks to Jussi Markkanen for providing me with the measurement data from the EISCAT experiments. Especially for providing me with this year's results on a short notice. In that regard, I also send my gratitude to the rest of the EISCAT-crew for conducting the experiment in April, and for giving me the opportunity of being on site during the process. It was a fun experience.

Thank you to my fellow students and friends Aurora, Yoshiaki and Erik for keeping a good spirit in the office throughout. It has been a difficult semester for all of us, but your support is something that have carried me through. Much credit goes to my main study partners for five years, Martin and Håvard. Countless long nights spent at the university somehow became a less miserable experience due to your presence.

I want to thank all of my friends and family for your support through the year. A special acknowledgement goes out to my brothers, Mattis and Mikkel, for taking the time to proof-read my thesis the final week. Your feedback has proven very helpful.

Last but not least my, I want to thank my beloved girlfriend, Kine. Your amazing support through the course of five years, and the last one in particular, will I forever be grateful for. All the sacrifices that comes with me spending countless hours in the office, is not something I take for granted. You are a major part of the realization of this thesis.

List of Abbreviations

ASAT Anti-satellite

BPE beam-park experiment

CNSA China National Space Agency

DISCOS Database and Information System Characterising Objects in Space

DRDO Defense Research and Development Organization

EGO Extended Geostationary orbit

EM electromagnetic

ENR energy-to-noise ratio

ESA European Space Agency

FOV field-of-view

GEO Geosynchronous Equatorial orbit

GTO GEO Transfer orbit

HEO Highly Elliptical orbit

HPLA High Power Large Aperture-radars

IADC Inter-Agency Space Debris Coordination Committee

LEO Low Earth orbit

LMO LEO-MEO crossing orbit

LOS line-of-sight

MEO Medium Earth Orbit

MGO MEO-GEO crossing orbit

NASA National Aeronautics and Space Administration

NSO Navigation satellites orbit

PD Payload Debris

PF Payload Fragmentation Debris

PL Payload

PM Payload Mission Related Object

RAAN right ascension of the ascending node

RADAR RAdio Detection And Ranging

RB Rocket Body

RCS radar cross-section

RD Rocket Debris

RF Rocket Fragmentation Debris

RM Rocket Mission Related Debris

SIA Satellite Industry Association

SNR signal-to-noise ratio

SRM Solid Rocket Motor

SSN Space Surveillance Network

SSO Sun-synchronous orbit

TLE Two-Line Element

UHF	Ultra High Frequency
UI	Unidentified
USSTRATCOM	United States Strategic Command

Contents

List of Figures

List of Tables

1

Introduction

1.1 Motivation

The next decade will see more launches of space assets than ever before. New innovations and advancements in technology have lowered the total costs related to a single spacecraft. Launches are conducted more frequently, and an increasing number of payloads are deployed at each instance. This has caused the space industry to take a turn of events. In the past, space operations were limited to a small group of operators, usually funded by governments. At present time commercial actors, such as SpaceX, are becoming the dominant contributor to satellites in LEO, as shown in Figure 1.1.

Therefore, the topic of space debris is as relevant as ever, seeing how the orbit population are increasing. Avoidance maneuvers from spacecrafts are being performed on a regular basis. Thus operators have the ability of avoid accidental collisions with targets larger than 10 cm in size – as these are regularly tracked by the U.S Space Surveillance Network (SSN) and maintained in the catalog[1] [Uni21]. However, smaller debris than this can also pose significant damage to an operative spacecraft.

---

[1] This will be called the Spacetrack-catalog in the thesis. It is maintained by the 18 SPCS (Space Control Squadron). Responsible for the operations are the United States Space Command (USSPACECOM). This command was reestablished in 2019, taking over space operations from USSTRATCOM. However, since I only became aware of this change when finalizing the thesis, the latter term will be used in the text.

This makes High Power Large Aperture-radars (HPLA) radars – such as EISCAT UHF – so desirable to use for debris studies, as they are able to detect objects with smaller size than 10 cm. Therefore, beam-park experiments can offer valuable support to estimation models regarding this size regime [Kli10].

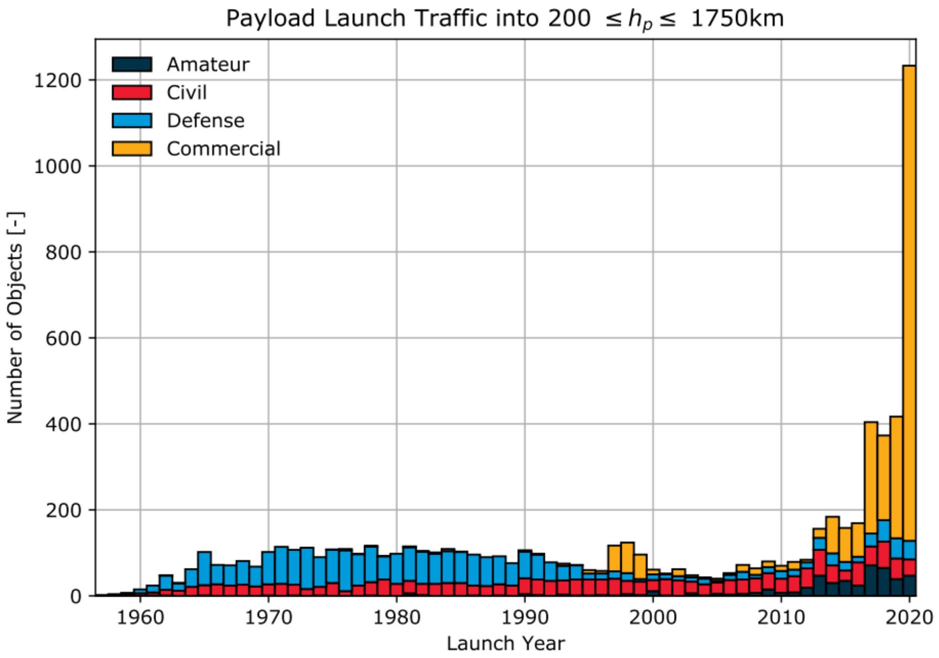

Figure 1.1: Annual number of objects launched into perigee altitudes between 250 and 1750 km, based on funding source. Figure is captured from [ESA21, p.26].

1.2 Goals

The main objective of the thesis is to establish an evolutionary overview of the fragments generated in the 2019 Indian satellite destruction, using results from four independent beam-park observations captured with EISCAT UHF.

On the way towards this, one of the goals will be to correlate the measurements with the catalog. This will help us identify observations coming from the familiar space population, and those associated with unknown objects. This distinction would make it possible to discover the presence of new fragmentation events. Another reason for doing the correlation is to recognize the potential small sized debris in the observations, since these will belong to the unknown category.

Having access to data from four experiments, a natural goal will be to evaluate the evolution of the overall orbital region that is measured.

1.3 Structure of thesis

The three main constituents entering this thesis can be summarized as follows; orbits, space debris, and radars. Collectively these form the baseline of the thesis theory, with each of the subjects being devoted their own chapter. Understanding orbits are important because they form the movement basis for the debris. Likewise, gaining knowledge of space debris itself is necessary since they are the targets we want to measure. These measurements are captured using a radar, therefore is it beneficial to gain insight on how this is performed.

After the theoretical outline is completed, the result part of the thesis will follow. They are structured over three chapters divided with logical intersections. First off some general results from the radar observations are set forth. These are presented prior to the chapter considering the catalog correlation – which thoroughly outlines how we can divide the radar detections into two categories. The results containing this distinction are presented in the final chapter of the result segment. The discussion appears alongside the results.

Finishing the thesis are the conclusions highlighting the key results of our research, before ending with some proposals for future work.

Every chapter begins with a brief introduction to the relevant subject. The purpose of these are to *guide* the reader into the topic before kicking off the main conversation of the chapter.

A short summary of each chapter is listed below.

Chapter 2: Orbit fundamentals are covered. The focus will be on Earth orbits. We consider how orbits are classified, the perturbations that apply, in addition to a brief description on the most utilized orbital regimes.

Chapter 3: Here the space debris theme are given increased attention. Since this is the main topic of investigation, there is devoted substantial effort in providing a thorough description of it. Given the vastness of the subject, many more things could surely be covered here. However, given the restricted time we had to limit our discussion. The chapter starts off by discussing the concept of space debris, its genesis, and how we discriminate between different sorts of debris and other artificial objects in orbit. We then proceed to talk about how debris have evolved with time. With the main focus on some of the largest debris generating events on record. Further it is provided information on the distribution of space objects with respect to size, orbit regime and inclination. Wrapping up this chapter is a discussion on why debris are considered dangerous, and how it may harm the global infrastructure.

Chapter 4: Here we make acquaintance with some radar theory. After introducing some fundamentals, a description on certain radar types will be given. The focus will then turn to consider the EISCAT UHF radar. Following this we will describe the properties of the radar equation and its components. The importance of the signal-to-noise ratio, in addition to the radar cross-section will be highlighted. After going through what quantities can be measured in debris studies, we will describe the specific radar mode called *beam-park experiment*.

Chapter 5: Results from the four EISCAT campaigns are presented. The most important results in this chapter are the estimated inclination distributions.

Chapter 6: The correlation method is covered. A thorough outline on the process, as well as a discussion on the threshold choice is provided.

Chapter 7: In this chapter we primarily investigate the evolution of the leftovers from the 2019 Indian Anti-satellite (ASAT) mission. Additional observed remnants from other notable breakup events will be described in parallel. We present the data in various formats, including *range vs time*, *Doppler velocity vs time*, and *Range vs Doppler velocity*.

Chapter 8: Includes the conclusion and future research topics.

2

Orbital Theory

In an ever-expanding universe where the void of "nothing" gets continuously bigger, gravity acts as the fundamental force of *gluing* matter together in subsystems within this vast emptiness. Mutual gravitational attraction between enormous celestial bodies is the very foundation of why orbits exist. Across a certain distance these bodies form a system orbiting around their collective center of mass. Just as billions of stars within a galaxy orbit a central black hole, planets orbit around their local star within the interplanetary medium of a solar system. Further, satellites orbit their closest planet. For most planets, their associated orbiting satellites include smaller astronomical bodies such as moons, asteroids and meteoroids. This is also the case for our own planetary home – the Earth. However, ever since humanity cracked the code of launching our own creations into space, Earth’s neighbourhood has also become occupied by artificial satellites. Today, this has evolved into a quite sophisticated network of structures – each of them orbiting the planet in a specified manner. As this web of orbits form the foundation of investigations in this thesis, we start off by looking into some of the features that apply.

2.1 Characterising orbits

In order to accurately specify the location of an object in space, for instance a payload, or a debris object, one needs to know its six Keplerian elements.[1] In the remainder of this section we consider the orbiting object to be a satellite, I.e. its nature is not specified, nor is it required, as the following apply to satellites in general. The contents of this section are primarily captured from [Kli10, p.317-325].

If we gather the Keplerian elements in a parameter χ, it can be expressed as

$$\chi = [a, e, i, \Omega, \omega, \nu]^T. \tag{2.1}$$

The two first elements appearing on the right-hand side of this equation, is the orbit's semi-major axis a, and its eccentricity, e. Together, these two parameters describe the size and shape of the orbit. These quantities are quite straightforward to derive using simple geometric relations, and can be expressed as

$$a = \frac{r_a + r_p}{2},$$

and

$$e = \frac{r_a - r_p}{r_a + r_p}.$$

Here, the term r_a is the *apogee* distance, while r_p is the *perigee* distance.[2] Both are measured from the center of the Earth. When $r_a = r_p$, we see that the eccentricity, e, becomes zero, and that the semi-major axis a, can be replaced with a radius, r. In this special case the shape of the orbit will be circular. However, in the more general scenario where $0 < e < 1$, the orbit shape is elliptic.[3] This governs the majority of satellites in geocentric orbits. For orbits that have an eccentricity close to zero, the term *near-circular* may be used to describe their shape. Many satellites are located in such orbits.

The next two terms in Eq. 2.1 are the inclination, i, and the right ascension of the ascending node (RAAN), Ω. Together these determine the orientation

---

[1] The term *orbital elements* is also frequently used.

[2] Perigee is the point along the orbit where the object is closest to Earth. Whereas the apogee is the position in the orbit located furthest from the Earth. The suffix "-gee" is a replacement for the more general "-apsis", implying that we are considering geocentric orbits. The latter is just a more convenient way of saying that we are regarding orbits bound to Earth.

[3] Two other cases exist. For $e = 1$ the trajectory takes the shape of a parabola, while for $e > 1$ the trajectory is hyperbolic. Neither of these cases will be encountered in this thesis.

of the orbit. The inclination is defined as the angle between the equatorial and the orbital plane. Intuitively, when $i = 0°$, the two planes are parallel, and when $i = 90°$, the orbital plane is perpendicular to the equatorial plane.[4] The RAAN is the angle from some reference direction,[5] to the position of the ascending node [6] – measured inside the equatorial plane.

The two remaining elements in Eq. 2.1 are the argument of perigee, ω, and the true anomaly ν. Both are angles measured in the satellite's travelling direction. Together, they let us determine the true position of the satellite along its orbit. The argument of perigee is defined as the angle that spans from the ascending node to the perigee – measured in the orbital plane. Lastly, the true anomaly is defined as the angle between the perigee and the true position of the orbiting body. The true position of a satellite is continuously changing, making ν a time dependent parameter. In place of the true anomaly, we can alternatively use the eccentric anomaly E, or the mean anomaly M, yielding the relations

$$E = 2 \arctan\left(\sqrt{\frac{1-e}{1+e}} \tan\left(\frac{\nu}{2}\right)\right),$$

and

$$M = E - e \sin E = n t_{pe},$$

where t_{pe} is the time since passing the perigee, and n is the mean orbital motion. The mean orbital motion is inversely proportional to the orbital period T, since

$$n = \frac{2\pi}{T},$$

whereas T in itself can be expressed as

$$T = 2\pi \sqrt{\frac{a^3}{G M_E}}, \tag{2.2}$$

with G being the universal gravitational constant, and M_E being the mass of the Earth.

If we use the mean anomaly M as the sixth orbital element instead of the true anomaly ν, we see that for an unperturbed orbit, the mean anomaly is the only

---

[4] Furthermore, when $i \in [0°, 90°)$ we have a *prograde* orbit, meaning that the satellite is moving in the same direction as the rotation of Earth. On the other hand, if $i \in (90°, 180°]$, the orbit is *retrograde*, and the satellite moves in a relative direction opposite to the Earth rotation.

[5] Known as the vernal equinox, or *The First Point of Aries*.

[6] The ascending node is the point where the satellite crosses the equatorial plane from south to north. When crossing this plane going north-to-south, the intersection point is called the descending node.

parameter of χ that changes with time. This rate of change is equal to the mean motion n, since

$$\frac{dM}{dt} = n = \sqrt{\frac{a^3}{GM_E}}.$$

However, satellite orbits bound to Earth should not be regarded as an unperturbed system. In fact, these orbits are subject to several types of perturbations. How they can be distinguished, are listed in the following paragraphs.

Aerodynamic perturbations arise as the satellite propagates through the Earth's atmosphere, where the satellite will be influenced by lift and drag forces, with the second being the most dominant. The effect of these perturbations are in particular dependent on the local air density of the atmosphere – which increases exponentially with decreasing height – as well as the satellite's area-to-mass ratio, and its velocity. Since the drag force is non-conservative, its influence will reduce the kinetic energy of the satellite, which can be related to a decline in its velocity. This decline forces the satellite to decrease its altitude. If the atmosphere is sufficiently dense, the frictional heat imposed by the drag may become too substantial to withstand for the satellite, in which it will disintegrate and burn up in the atmosphere. Most space objects are removed from orbit in this manner, and this natural process, called *de-orbiting*, is our primary weapon against accumulation of space debris. Some pieces of particularly large objects, may survive the atmospheric reentry, however, since the bulk of the globe are covered with oceans, or wilderness, the probability of it injuring any people is infinitesimal.

Geopotential perturbations are caused by asymmetries, and imperfections, in the Earth's gravitational field. To accurately model this, one needs to conduct a harmonical expansion which takes in different sorts of harmonic functions, all of which are described with different sets of coefficients, and have a distinct dependency on the geodetic latitude, λ, and longitude, ϕ, as well as the geocentric distance r, to the satellite. The complexity of this process prevents us from elaborating this further. The point is that Earth is not a perfect sphere, further is its gravitational field not uniform, and these discrepancies pose influential effects on a satellite's trajectory. The most dominant of the these is the first order perturbation term, J_2, which is caused by the oblateness[7] of the Earth.

Third body perturbations govern the gravitational pull experienced by the satellite, coming from other celestial bodies than the Earth. These perturbations are dominated by pull from the Sun and the Moon.

[7] The fact that Earth is not perfectly spherical, due to the equatorial diameter being greater than the diameter connecting the poles.

Radiation pressure perturbations arise as the satellite interacts with photons emitted by the Sun. The effect of photons reflected off the Earth can be regarded as negligible for space debris, and thus only the direct solar radiation pressure plays a decisive role. Thus, the solar activity will be included in the equation that determines the orbital lifetime of a space object.[8]

In the general case, all of the above listed – except aerodynamic perturbations – can be regarded as conservative perturbation forces, with some exceptions. In real life applications, and precise orbit modelling, it is important to take these effects into account, as they will alter the orbit of a satellite over time.[9] How the orbital elements of a satellite change with time, can be expressed by the Gauss perturbation equations, or the Lagrange perturbation equations, which can be found on p. 325 and p.326 in [Kli10].

2.2 Orbital regimes

The geocentric orbital environment is comprised of several different regions. How one distinguish between them varies, but the most common approach is to do so with respect to the altitude of the orbits. Within each domain, one may discriminate between different kinds of orbits using their inclination, as it is important for many applications that this is chosen appropriately. However, in this section we only consider orbit regimes divided with respect to height. As it is more appropriate to describe the inclination-specific orbits when these are encountered.

The main orbital regions are Low Earth orbit (LEO), Medium Earth Orbit (MEO) and Geosynchronous Equatorial orbit (GEO). Even though we provide a brief description of all three in this section, it should be pointed out that the primary region of interest for our research, is LEO.

LEO is the orbital regime located closest to Earth, with the altitudes ranging from 200 to about 2000 km above the surface. The relative low altitude is beneficial in multiple satellite applications, which include meteorology, Earth observation, and what has become more common in recent time; internet services. The latter will be increasingly exploited in the near future, as commercial actors such as *SpaceX* and *OneWeb*, are launching large satellite constellations into LEO. The broad spectrum of applications serves as an explanation for why this regime has become the most populated region among geocentric orbits.

---

[8] Also because the density of the atmosphere at higher altitudes varies with the solar activity.
[9] Generally, such trajectories are called *osculating Keplerian orbits*.

MEO extends from altitudes of about 2000 km to about 31570 km. Navigation satellites are mainly found within this region, often configured in constellations. To maximize their coverage, navigation satellites are usually located at high altitudes – mainly between 18100 km and 24300 km above mean sea level.[10]

The GEO region contains objects at altitudes of 35586 km to about 35986 km, with the most common choice of altitude being 35786 km. The great advantage of satellites located here, is that they typically have an orbital period that matches the rotational period of the Earth.[11] To achieve this, the satellite's orbital plane needs to be parallel to the equatorial plane, and the orbits need to be circular.[12] If the satellite fulfils these requirements, they appear fixed on the sky when viewed from the Earth. This allows the associated ground station to have a permanent pointing direction when communicating with the satellite. The great altitude also opens up for a large geographical coverage for the spaceborne sensors in GEO. These attributes are especially valuable in communication services, which is why many of the spacecrafts situated here belongs to major broadcasting companies [ESA20b].

In some of the figures that appear in this thesis, additional orbit abbreviations are introduced. Although these orbits are outside of our scope, it may be useful to understand their meaning. These are listed below, with h_p and h_a denoting the perigee and apogee height given in kilometers. Whereas a is the semimajor axis, e is the eccentricity, and i is the inclination.

- LEO-MEO crossing orbit (LMO):
  $h_p \in [0, 2000]$, $h_a \in [2000, 31570]$.
- Navigation satellites orbit (NSO):
  $h_p \in [18100, 24300]$, $h_a \in [18100, 24300]$, $i \in [50, 70]$.
- MEO-GEO crossing orbit (MGO):
  $h_p \in [2000, 31570]$, $h_a \in [31570, 40002]$.
- GEO Transfer orbit (GTO):
  $h_p \in [0, 2000]$, $h_a \in [31570, 40002]$, $i \in [0, 90]$.
- Highly Elliptical orbit (HEO):
  $h_p \in [0, 31570]$, $h_a > 40002$.

---

[10] Sometimes this exact type of orbit are specified as Navigation satellites orbit (NSO).
[11] Which equals 23 hours, 56 minutes, and 4 seconds, to be precise.
[12] I.e. satellites residing in GEO usually have zero inclination, i, and zero eccentricity, e.

- Extended Geostationary orbit (EGO):
  $a \in [37948, 46380]$, $e \in [0.00, 0.25]$, $i \in [0, 25]$

All of the values presented within this section are those used in [ESA21].

3

Space debris

Satellites, rockets, and space shuttles – these are terms that the interested layman, presumably, associate with the magnificent field of space exploration. If we travel a century back in time, few people would have created this association. Nor could you blame them, since at the time space still remained a heavenly frontier untouched by mankind. Almost four more decades would go by, before human space exploration would commence.[1]

Since then, the global community has undergone a technological revolution that permeates all aspects of modern society. A manifestation of this development is the astonishing network of space assets continuously passing over our heads. Due to an ever-expanding space industry, words like *satellite* and *rocket* has now entered the vocabulary of people across the globe, much due to prime contributors within the field, such as National Aeronautics and Space Administration (NASA). Indeed, the acronym NASA in itself, sparks clear associations to space operations, thanks to the organization's many media appearances during the last decades.

This thesis is not going to focus on the topics of the global media, nor is it a linguistic article. However, the reason why people have gained perception of the mentioned concepts, is because of the substantial attention they have received in the past. Hopefully, in the future, another term can be added to this list, namely because it deserves more attention. Presumably, only a small

---

[1] The launch of Sputnik 1 in 1957 serves as the beginning of the *space age*.

fraction of the global population are familiar with the concept of *space debris*. Consequently, is it not well-established in the international community that this is becoming an issue – with growing concern. Raising the global awareness on the subject, should work as a first step towards reducing this concern, as recently stated in [UNO21]. Before we elaborate further on the danger with space debris, we need some background information.

3.1 What is space debris?

Space debris, or space junk, is exactly what the name implies – the garbage left in space. It is a collective term that applies to all artificial objects in orbit, which no longer fulfill any useful purpose.

Opposed to operative spacecrafts, we cannot remotely control space debris, and therefore we have no way to directly influence their trajectories. This is a fundamental challenge with all debris, which makes their presence problematic. Moreover, if a debris object should collide with a satellite, it may very well destroy the satellite altogether.

3.2 Composition

One can think of space debris as the undesired heritage resulting from more than 60 years of orbital operations. Several types exist, but they all share the fact of being placed into orbit by mankind. What is now considered debris, once played some useful function for a previous operational mission. The leftovers remaining in orbit after a spacecraft has reached its end-of-operations, are deemed to be debris stemming from that particular spacecraft. And since a spacecraft consists hundreds of different parts and compounds, so does the debris environment. It holds a vast pool of objects – with significant variations in size, structure and composition. Ranging from large decommissioned satellites, down to micro-sized drops of propellant, the realm of space debris carries great diversity.

Materials used in spacecraft construction needs to withstand extreme conditions, in addition to being light and easy to shape. A material that fulfills these requirements is aluminium. For this reason, aluminium has been a popular choice in spacecraft design over the years. Specifically, it is common to construct the body of a spacecraft out of aluminium alloys. Other common materials being used, include magnesium alloys, titanium alloys and ferrous alloys [Hou11]. A natural consequence of this is that a large mass fraction of the space infrastructure – including space debris – consist of these materials.

The area of application for the different materials is dependents on their properties, and is chosen after careful inspection of the numerous physical factors that a space structure needs to withstand. This is not something that is going to be detailed here, but can be found in [Hou11]. At the end of the day, the composition should secure safe operations for the spacecraft in line with its specific mission objectives.

3.3 Space object and debris categories

With every launch executed, new objects are added to the space environment, and with it – a new source of potential space debris is put into orbit. This logic is not unique within the field of space flight – ship launching for instance, also serves the risk of creating additional shipwrecks. Thus, if humans never had put boats on the ocean, we would never had shipwrecks. Likewise, if we never had launched anything into space – space debris would not exist. On the other hand, living in this risk-free fashion would prevent us to evolve as a species, and to pursue our curious and intelligent minds – the very essence of human nature. Therefore, the existence of space debris is not negative in every sense, as it paints a picture of an ambitious species that has clear futuristic visions. Let it be understated that the physical presence of space debris yield few positive effects.

Tracking and cataloguing space objects, particularly debris, is a complicated exercise. There are various methods to characterise space objects, but a common approach is to trace the objects back to a launch event, which enables categorisation in terms of a parent body. If an unfamiliar object yields sufficient correlation with already cataloged objects, it can get classified accordingly. Extensive datasets has been developed for this purpose, containing information about the orbital and physical properties for an abundance of space objects. Among the most comprehensive of these sources, we find the Two-Line Element (TLE) datasets provided by the United States Strategic Command (USSTRATCOM), and the Database and Information System Characterising Objects in Space (DISCOS) – maintained by the European Space Agency (ESA) [Kli10, Uni21, ESA20c].

When considering space applications, it is convenient to separate the parent structures into two main categories – payloads and rockets. In relation to both of these we have four subcategories, when following the nomenclature used by ESA. These are listed in Table 3.1, where the example column provides suggestions of possible objects associated with each category. Note that there is a fine line between PF and PD, and an object may go from the latter to the former type, once additional information about its properties are obtained. The same goes for RF and RD. The last category – which is not included in the table – is called Unidentified (UI). These objects have not been possible to classify due to insufficient data associated with them [ESA20c].

Table 3.1: Space object types that ESA distinguishes between. Types and description are adapted from [ESA20c].

Type (abbrev.)	Description	Examples
Payload (PL)	Object with scientific objective	Include active and inactive satellites
Payload Fragmentation Debris (PF)	Debris arising from collision or explosion of PL, genesis known.	Fragments of payloads
Payload Debris (PD)	Unclear genesis, but have properties that match with a PL	Paint flakes, etc.
Payload Mission Related Object (PM)	Previous parts of PL, intentionally released during mission.	Replaced solar panels, astronaut tools, etc.
Rocket Body (RB)	Object with launch-related function	Orbital stages
Rocket Fragmentation Debris (RF)	Resulting from in-orbit explosions of rockets, known genesis.	Fragments of rocket bodies.
Rocket Debris (RD)	Unclear genesis, but have properties that match with a rocket.	Various ejecta from engine firings
Rocket Mission Related Debris (RM)	Previous parts of RB, intentionally released during mission.	Engines, shrouds etc.

Figure 3.1 illustrates how the orbital population has evolved since the beginning of the space age until current time. The contribution from each of the described categories are shown. The plot only considers the objects contained in catalogs, which is mainly comprised of structures larger than 10 cm in size. Thus, the true numbers of objects are expected to be much higher.

It is evident that the on-orbit population is expanding at an increasing annual rate, and it appears that the number of objects has tripled over the previous 15 years. Going back to the first decade of the 2000's, two distinct *jumps* are visible in the graph. The first of these increases is due to the destruction of the Chinese weather satellite, *Fengyun-1C*, occurring in 2007. While the second jump, taking place in 2009, is related to a collision between a functional satellite, *Iridium-33*, and a derelict satellite, *Cosmos-2251*. Both of these events will be revisited in Section 3.4. At the time, these events caused a substantial increase to the amount of Payload Fragmentation Debris (PF)-debris, raising the overall population accordingly. Since then, fragmentation debris – PF and Rocket Fragmentation Debris (RF) in particular – have been the most numerous type of objects in orbit, outnumbering the population of functional payloads, Payload (PL), by a landslide.

Moreover, the occurrence of Unidentified (UI) objects are noteworthy over the last few years. The typical reason for this, is that it can take up to several years from a breakup event occurs, until sufficient data is gathered to accurately catalog the associated objects [ESA21]. However, it is also evident that if these unidentified objects were to enter another class, it would still indicate a notable rise in the total population – particularly in the last two years. And since we can assume payloads to get reported, and thereby cataloged close to its launch – it implies that these surges are predominantly caused by an increase in debris.

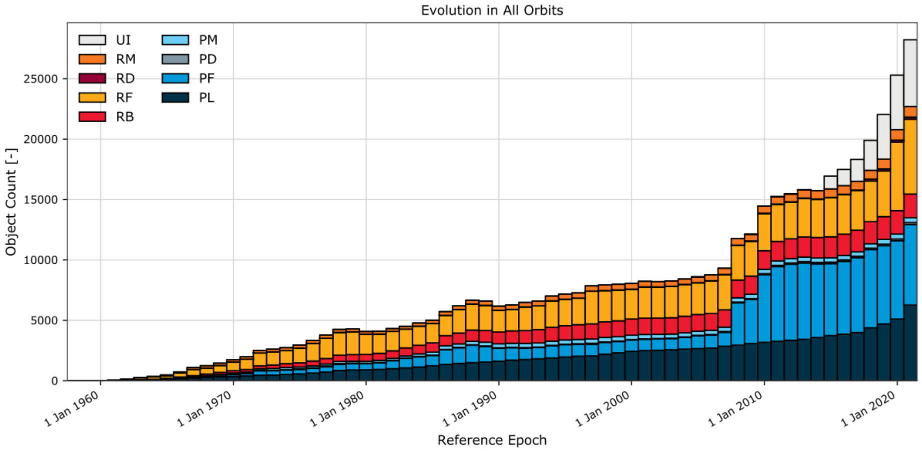

Figure 3.1: Evolution of the cataloged space object population, discriminated by type. The figure is captured from [ESA21].

3.4 Creation of debris

There are several causes for how debris has been generated up through the years. Something that was more prominent in the past – when the use of Solid Rocket Motor (SRM) boosters was more common – is the generation of slag and dust particles, mostly composed of aluminum oxide (Al_2O_3). Peaking in the 1980s and 90s, the total amount of SRM firings accounted for several tons of these particles, making it a significant contributor to the debris environment at the time. The size of these particles can vary from a few micrometers up to a couple of centimeters, making them small enough to elude conventional tracking methods. However, cm-sized particles are still large enough to cause severe damage to a spacecraft upon collision, which makes such slag particles dangerous inhabitants in the orbital environment. Fortunately, the use of solid propellant in rocket engines has declined significantly during the last two decades – reducing the presence of slag particles in orbit [Kli10].

Another type of small-sized debris is paint flakes. These particles arise as a result of surface degradation of the spacecraft. Just like the paint on a house flakes off after a long-term exposure to wind and weather – so does the thermal coating of a spacecraft. Only for the latter, the conditions are a bit more extreme, so the time that elapses prior to flaking, is a lot shorter than for a house on Earth.

Several causes for debris can be mentioned, but for the remainder of this section we will focus on the most influential of all causes – namely fragmentation events (also called breakup events). These events are the far most productive source of space debris, and can be held accountable for the worst contamination that have occurred in the history of space flight. A fragmentation event can be an explosion of a launch vehicle or payload, often caused by an engine failure, or it can be a collision of the deliberate or accidental kind. An accidental collision may involve two payloads in different orbits that cross paths at the exact same time, or it may – more likely – involve a payload which collides with a smaller debris object. Deliberate collisions exist as well, and are commonly referred to as ASAT tests. This involves launching a rocket equipped with a missile into orbit, with the objective of shooting the missile weapon into a targeted satellite – purposely destroying it. According to [ESA20a], the overall number of events yielding fragmentations are currently more than 560, when considering all breakups, collisions, explosions and anomalous events that has occurred through the history of space flight. The remainder of this section is devoted to describe some of the worst of these events.

3.4.1 Desctruction of Fengyun-1C

The Fengyun-1C was a Chinese weather satellite residing in a LEO at an altitude of 845–865 km above mean sea level, orbiting with an inclination of 98.6°– a so-called Sun-synchronous orbit (SSO). On the 11th of January 2007, the satellite became the target of a successful ASAT test, conducted by China National Space Agency (CNSA). At an estimated altitude of 850 km, a ballistic missile was shot into the satellite – immediately destroying it – generating an extensive debris cloud. The collision triggered the satellite's initial mass of 960 kg to be scattered over a huge altitude regime – ranging from 200 km up to 4000 km – according to estimates derived short time after the collision. To put this into perspective, the distance is equivalent to the one between Tromsø and Lisbon, a range that all of a sudden got an increased amount of debris, with the main fraction distributed around the original altitude of 850 km. Objects situated at this height are less affected by perturbation forces than objects situated at lower altitudes, and may take over a century to de-orbit. By 2016, the Fengyun-1C constituted, with its 3428 debris fragments, nearly 20 % of all objects cataloged by the U.S SSN. At this time, 90 % of the cataloged Fengyun-1C fragments were still in orbit, yielding a population of 2880 objects [Nat07, Nat12, Nat16]. Note that this number only regard objects with a minimum size of 5 cm. The portion of the population which the SSN can reliably track, consist of targets larger than 10 cm. However, a lower size limit has been achieved for this particular case, using special assistance from the Haystack Radar for the smaller debris [JSL+08]. The true size distribution extends even further down, thus the actual fragment population are assumed to be even more numerous.

At the time, the event marked the first ASAT test conducted in more than 20 years[2], and was a clear violation to the mitigation guidelines[3], which the CNSA had officially accepted five years prior to this event. We are not going to focus on the political aspects here, but it is safe to say that the experiment did not receive much applause from the international space community. As this event has, undoubtedly, increased the collision threat for hundreds of satellites in the LEO-environment [Nat07, Int20].

Going to the current year (2021), it is a substantial amount of leftovers from this event, that still orbits the globe. A quick search in the spacetrack-catalog [Uni21], using the international designator[4] of Fengyun-1C, as a keyword, tells us that 662 out of 3535 cataloged objects of this debris cloud, have de-orbited by now.[5] I.e. over 81% of the Fengyun-fragments still pose a collisional threat to other spacecrafts, 14 years after the breakup occurred. Moreover, the inclination of these pieces spans from 94.67° to 106.19°, implying a notable variability across the orbital environment. The highest residing fragment has an apogee height of 3320 km, thus, one can expect some of the debris to still be in orbit at multiple generations ahead in time, presumably for several centuries.

[2] The former was performed by the U.S in 1985.

[3] Guidelines put in place by the Inter-Agency Space Debris Coordination Committee (IADC), with the objective of reducing the amount of debris in orbit.

[4] International designator of FY-1C: *1999-025*.

[5] With the latest occurring on 31/03/2021 [Uni21].

3.4.2 Collision between Iridium-33 and Cosmos-2251

The 10th of February, 2009, mark the date of the first ever collision between two intact spacecrafts in orbit. At approximately 16.56 UTC, the U.S operational communication satellite, Iridium-33, collided with the inoperative Russian communication satellite, Cosmos-2251, at an altitude of 790 km. Both satellites were moving in near-circular orbits, with their orbital planes having an inclination of 86.4° and 74.0°, respectively. A slight difference in inclination together with an equal altitude, calls for conflicting points along the two trajectories. But for a collision to happen, both objects need to be at one of these locations at the same time, which is a quite improbable (but not impossible) scenario. Nonetheless, this became the reality for these two payloads. As both satellites were to make an overhead pass over northern Siberia – their paths crossed – causing an extremely powerful collision which shattered both payloads into pieces. The satellites collided at near right angles with each other, indicating a relative collision velocity well above 11 km/s. Since the Russian satellite and the American satellite had a respective mass of 900, and 560 kg, it is expected that close to 1.5 tons of debris particles were generated in this event. Moreover, this mass gets distributed over a vast amount of smaller objects, all of which have different size and shapes. This random nature is a problematic feature with all debris, as deviations in area-to-mass ratio will make the fragments respond differently to perturbations, which cause the debris cloud to diffuse along its orbit, presumably, at a rather rapid pace [Nat09, NAS12]. Since this aspect is of great importance, it deserves additional explanation. Therefore, we step away from the particular collision for a brief moment, before returning to it in the subsequent paragraph.

Diffusion of debris When a satellite disintegrates, numerous fragments are generated. The fragments will have a great variation in shapes and sizes, where each fragment can be expected to exhibit a unique characteristic.[6] To be precise, every fragment can be identified by a certain area A, and a certain mass m, which in turn gives the debris cloud distinct variations in area-to-mass ratio, A/m. The magnitude of this ratio specifies how sensitive the object is to perturbation forces, such as aerodynamic drag. An object with high area-

---

[6] To support this, imagine throwing a glass to the floor. The fragile glass will not be able to withstand the impact from the solid surface, and as a consequence it will break into numerous pieces. The amount of small pieces that emerge would likely outnumber the amount of large ones. Moreover, you will hardly find two pieces that are identical. This serves as a consequence of slight differences in the molecular structure of the material, and the fact that every point on the glass are located at different distances to the point of impact, resulting in dissimilar impulse responses. This is only a simplified example, and the validity of the statements might be rightfully questioned. Nevertheless, the concept is transferable to the outcome of a satellite breakup.

to-mass ratio will experience significant "resistance" from the atmosphere, resulting in a rapid decrease in the kinetic energy of the object, ultimately slowing the object down, reducing its velocity. This velocity reduction will happen a lot slower for an object with a low area-to-mass ratio. This makes the debris cloud distribute itself randomly along its orbital ring, as time passes. After some period the debris will have diffused over the entire orbit. The amount of time it takes for the particular debris cloud to encircle the Earth, is dependent on the altitude where breakup occurs, due to the height-variation of the atmospheric density.

The short-term diffusion of the debris created in the Iridium–Cosmos collision can be seen in Figure 3.2 [NAS12].

By the beginning of 2016, the U.S SSN had cataloged 2296 debris objects originating from the Iridium-Cosmos collision, with 1668 of these coming from Cosmos 2251, and 628 objects from Iridium-33. Of these, the number of objects still in orbit were 1141, and 364, respectively. Hence, only 32 % of the Cosmos particles, together with 42 % of the Iridium debris, had de-orbited over the course of seven years. Thus, the main portion of the debris continues to be a threat to missions operating in LEO [Nat16, NAS12].

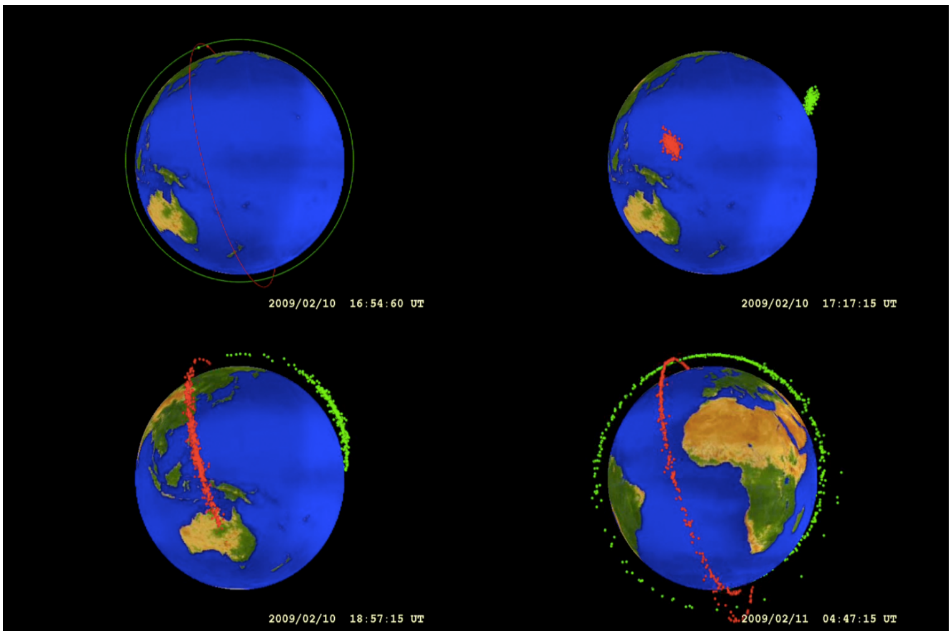

Figure 3.2: An illustration of the time evolution of the debris arising from the collision between Iridium-33 (green) and Cosmos-2251 (red). It shows the objects 1 min prior to collision, along with 20 min, 2 h, and 12 hours after the collision (from top left to bottom right). Figures captured from [NAS12], credit: NASA.

3.4.3 Destruction of Microsat-R

Among the most recent, and controversial, breakup events, we find the intentional destruction of Microsat-R. On the 27th of March 2019, the Indian Defense Research and Development Organization (DRDO) conducted a successful ASAT-test on their own satellite. Their objective is believed to be a pure demonstration of the country's military powers. With this, India became the fourth nation to conduct such a mission, following in the footsteps of USA, Russia and China. At the time of the collision, the satellite was in an orbit with apogee altitude of 294 km, perigee altitude of 265 km, and an inclination of 96.63°. Its mass was 740 kg. The advantage of the low altitude is that the debris can decay faster at the hands of the denser atmosphere. On the downside, the low altitude makes the tracking of the debris more difficult, since it puts a limitation on the maximum distance from which a radar site is able to detect the objects. Over 400 objects related to the event were initially tracked by the U.S SSN facilities, however, only 101 fragments entered the public catalog, as a result of inconclusive data. Out of the cataloged objects, only 49 remained in orbit less than four months later – as of 15 July, 2019 [Nat19a, UJO20].

Although we shall limit the political aspects in this thesis, it serves to our purpose to inform that the Indian DRDO stated that all of the debris created in the event would have de-orbited within 45 days – of which most should decay after only two days. This was based on their own claim that the interceptor hit the satellite *head-on*. However, as investigated by [Lan19], it seems to be some discrepancy between this statement and the true circumstances of the event. Video footage were released by the DRDO shortly after the event – showing both images captured on-board the missile moments before impact, as well as ground-captured images of the collision containing relevant telemetry data. The latter made [Lan19] conduct a thorough review of the event, with a result revealing that the interceptor must have hit Microsat-R from below – forming an angle of $\approx 48°$ with the local horizon. With a collision angle of this kind, it increases the risk of ejecting fragments into higher altitudes, and thus more eccentric orbits. This serves as a natural consequence of the interceptor's momentum vector pointing upwards away from the Earth surface.

More knowledge of this debris has been collected since 2019, and additional fragments related to this event have entered the public catalog. By present time (June 2021), the catalog contains 130 objects[7] associated with the breakup of Microsat-R [Uni21]. However, this value may be highly underestimated due to the above mentioned challenges, and does only comprise objects larger than 10 cm.

[7] It needs to pointed out that almost all of these have decayed by now, in fact, only one of these fragments are currently in orbit.

Obtaining better knowledge about the distribution and evolution of this debris cloud is the primary goal of this thesis.

More on Anti-satellite tests

Both Fengyun-1C and Microsat-R were victims of ASAT-tests. A visualization of the end-sequence of such a mission is included in Figure 3.3. In a matter of seconds, it goes from being a rather well-behaved system constituted of two intact objects, to be a chaotic system holding an uncountable number of fragments. One can expect a lot of these pieces to take modified paths deviating from the original trajectory. Consequently, the fragments will occupy a much larger area than their parent body. The collective area covered by the debris expands further with time, because the perturbations influence each fragment differently – due to the variable area-to-mass ratio of the debris. Only when the pieces start to de-orbit, will this trend be reversed.

When it comes to ASAT-tests, there is another factor which needs to be addressed, namely the generation of secondary debris stemming from the *kill vehicle*. The mass of the kill vehicle, or missile, will not evaporate altogether in the impact process. Rather, it also disintegrates in the collision, and thereby continue to orbit the planet for a period of time. It is however, challenging to classify the distinct contribution that comes from the kinetic kill vehicle, as information about it is rarely released to the public. Since such vehicles are launched short time before impact occurs – usually without alerting the public beforehand – it is not possible for sensor systems to capture the data necessary to catalog them. Without reliable information on the missile's mass and trajectory, the short- and long-term assessment of the secondary debris cloud, becomes a very complicated drill. In addition, it is hard to distinguish between the fragments coming from the spacecraft, and what originates from the missile. As a result, all debris which can be traced back to the collision, are typically classified as appearing from the spacecraft alone. For example, all debris stemming from the Indian ASAT test are called *MICROSAT-R DEB* in the Spacetack-catalog [Uni21]. In reality one can expect a good portion of these to be fragments from the missile.

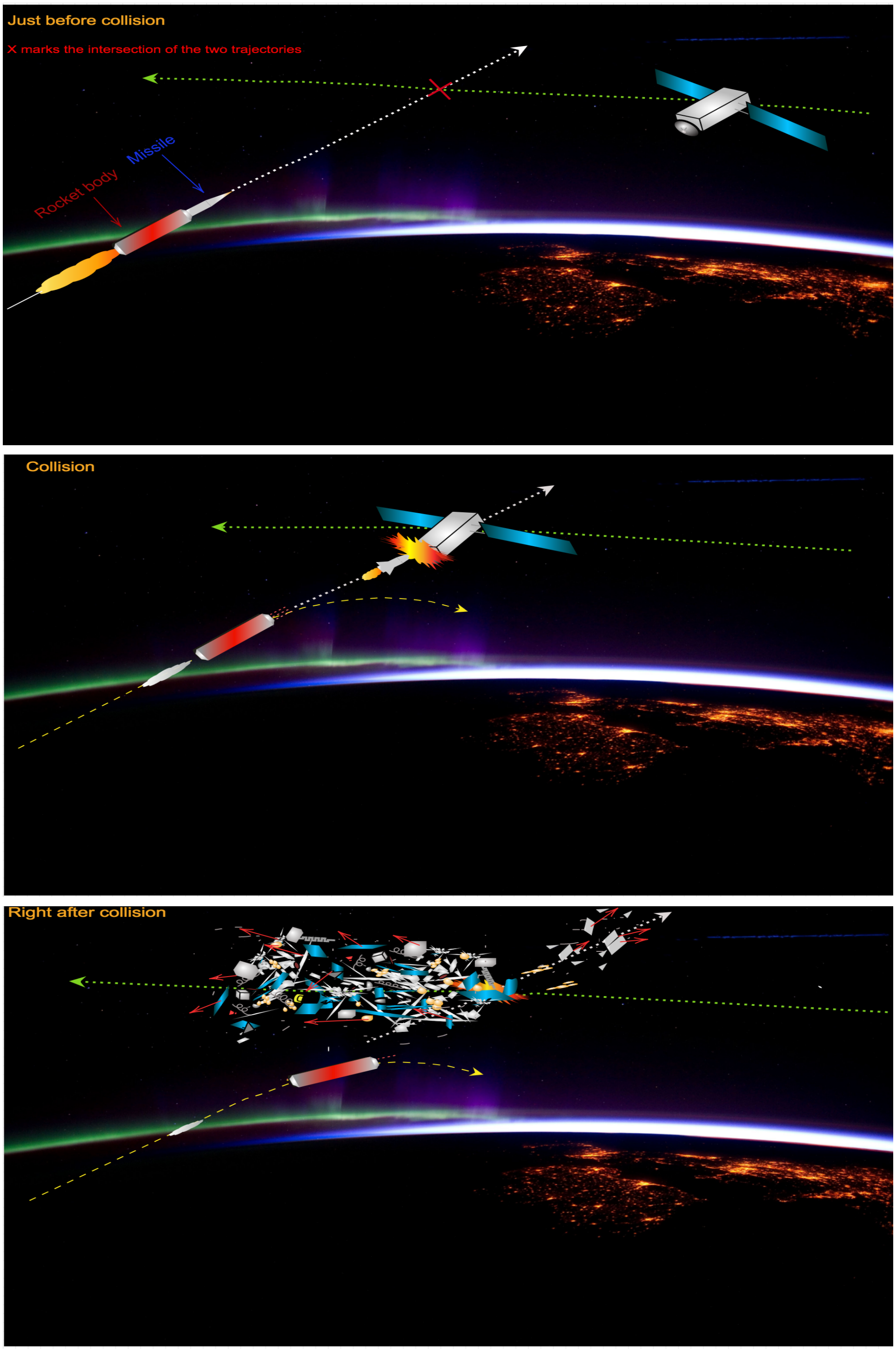

Figure 3.3: Illustration of how an ASAT-test may elapse. The arrows indicate the approximate trajectories of the bodies. Note that the explosion "flame" is not necessarily adaptable to true circumstances, since the amount of oxygen is limited at satellite altitudes. (The background image used is an image taken from the international space station, provided by NASA).

3.5 Size distribution

In prior sections, it has been mentioned that space debris varies greatly in size and shape. A simple explanation for this, is that debris is not something designed and formed by people, and therefore lacks the symmetry that we humans desire. Debris is rather something shaped by the physical forces of nature – a creator which do not care too much about such trivialities.[8] However, the size distribution of space debris reflects a pattern we find everywhere else in the universe as well, which states that we got a lot more of the small stuff, than we do of the big stuff. Or to put it in a more scientific way; the number of debris particles increase with decreasing size. Intuitively, this is simple logic – you need smaller things to construct a bigger thing.[9] Although we can extend this logic all the way down to the elementary particles, we will limit ourselves to how it translates to the creation of debris. When fragmentation occurs, nature will ensure that the product contains loads of tiny objects, many small objects, and some large objects. To reflect this fact, we can look at the number of debris objects that exist within different size regimes – as estimated using statistical models. The current number of objects in orbit, according to [ESA20a], are

$$N(d) \approx \begin{cases} 3.40 \times 10^4 & d > 10 \text{ cm}, \\ 9.00 \times 10^5 & 1 \text{ cm} < d \leq 10 \text{ cm}, \\ 1.28 \times 10^8 & 1 \text{ mm} < d \leq 1 \text{ cm}, \end{cases} \tag{3.1}$$

with N being the number of objects, and d denoting the size of the object. The reason d is used to denote the size, is because most statistical models approximate debris objects as spheres, in which d represent the diameter of the object.

Earlier in this section, we used the terms *tiny*, *small*, and *large*, to distinguish between object size. For convenience, we will stick with these terms. Hence, in the remainder of this section, we will refer to objects larger than 10 cm as *large debris*, between 1 cm and 10 cm as *small debris* and fragments between 1 mm and 1 cm as *tiny debris*.

In an attempt to provide a more intuitive picture of the ratios between the numbers in Eq. 3.1, we can compare them with similar numbers in terms of human populations.[10] The population of *large debris*, is similar to the number of inhabitants in Ringsaker.[11] This is a quite moderate value compared to the

[8] That is if we rule out the largest astronomical bodies (e.g. stars and planets), which usually has a sphere-like symmetry.

[9] Every person that has purchased a piece of furniture from IKEA would know this.

[10] Apart from simple statistics, I would discourage any attempt to otherwise compare space debris with human beings. Such things can come across as quite controversial.

[11] The 30th largest municipality of Norway.

amount of *small debris* – comparable in magnitude to the combined population of Oslo and Trondheim[12] [Sta21]. Whilst the number of *tiny debris* particles is in turn 142 times bigger – similar to the population of Mexico[13] [Wor21].

It is worth stressing that the numbers in Eq. 3.1 are estimates produced by statistical models, which differs greatly from the amount of objects that we actually keep track of. In fact, the number of debris objects that is regularly tracked by the SSN and maintained in their catalog are about 28 200 [ESA20a]. About all of these objects are large debris fragments, which is the size this radar-network are able to confidently detect. Hence, due to technological limitations, we need to rely on models when it comes to identifying the trajectories of the debris in the lower size regimes. However, High Power Large Aperture-radars (HPLA) are able to detect small debris as well, and we can therefore use these radars to assist the data from statistical models, but this is a fact that we will return to later.

If we consider sizes smaller than one millimeter, the space debris population is even larger. We will not focus too much on this size regime in this thesis, partly because particles of this size are too small to inflict any substantial damage upon impact with a spacecraft – because their bodies are equipped with shields as to withstand impacts from this type of debris. That includes much of the debris in the sub-centimeter regime as well. Do note however, that also these particles can inflict some damage to spacecraft surfaces which are not effectively shielded against them. Among these are the solar panels, which is the prime power source of orbiting vehicles. Solar panels has a large collective area as to gather sufficient solar radiation. This also makes the panels more exposed for impacts with debris, which can cause the panels to degrade faster than expected. The panels then need to be replaced if one wants to preserve the operational lifetime of the mission. A particular mission that has undergone such replacements on several occasions, is the Hubble Space Telescope. Because this has been performed using the space shuttles, it enabled retrieval of (some of) the replaced panels. During on-ground analysis of these panels several holes and damages were found, which one could relate to impacts from sub-centimeter sized debris. Hence, albeit their tiny size[14], this type of debris carry enough energy to inflict costly damages to orbiting vehicles. Although most modern spacecrafts are effectively shielded against such small particles, it paints a picture of the hostility of debris [Kli10].

---

[12] Norway's most, and 3rd most populous municipalities.

[13] The 10th most populous country in the world.

[14] Comparable to the size of snow flakes.

3.6 Altitude distribution

When an operator launches a spacecraft into orbit, the choice is not arbitrary. As described in Section 2.2, the mission objective is highly dependent on the orbit. Thus, it is not surprising that the population within different domains vary.

This distinct variation is confirmed by Figure 3.4, which displays the annual distribution in individual orbits, dating back to the very first launch in 1957. The abbreviations included in the plot were briefly described in Section 2.2. One can clearly see that the space population is growing, as all orbital bands show an increase in residents, with the most abrupt surges happening during the three latest years.

The rise is not that noteworthy in GEO though. The reason for this is that the valuable orbital period[15] is restricted to one particular altitude, thereby putting a limitation on the amount of spacecrafts that can co-exist in this ring. Just before mission termination, the spacecraft performs a so-called *end-of-life maneuver*[16], so as to free up its "GEO-slot" in which a new satellite can occupy. This is in compliance with the mitigation guidelines initiated by the IADC [Int20]. As a matter of fact, the recent replacements of spacecrafts in GEO, are reflected by the growth in EGO in Figure 3.4 – since this is the orbit where the *old* structures are brought to *die.*[17] It is evident that the bulk of the space object population are residing at altitudes below 2, 000 km. Out of all cataloged objects found in orbit by the end of 2020, 55%[18] belonged to LEO. However, less than 29% of these objects were payloads,[19] with the remaining portion covered by the other classifications appearing in Table 3.1. This means that 71 of every 100th object orbiting in LEO are, strictly speaking, space debris. Among these, 82% are – according to European Space Agency (ESA) – fragmentation debris [ESA21].

Note that the presented numbers only governs the orbiting structures with a minimum size of 10 cm, since the conventional systems are not able to track objects smaller than this. However, we know that the amount of objects increase substantially with decreasing size, as seen in Eq. 3.1. As good as every object with sizes below 10 cm are expected to be debris. Thus, including lower size regimes in the calculations would increase the relative ratio of debris

---

[15] Matching that of the sidereal day of the Earth.

[16] The remaining fuel is used to thrust the spacecraft into an orbit located further out from Earth.

[17] The choice of words is not random, as a frequently used term in place of EGO is *graveyard orbits*.

[18] 15, 540 objects out of an overall population of 28, 218 are located in LEO.

[19] 4, 407 of 15, 540 items are payloads.

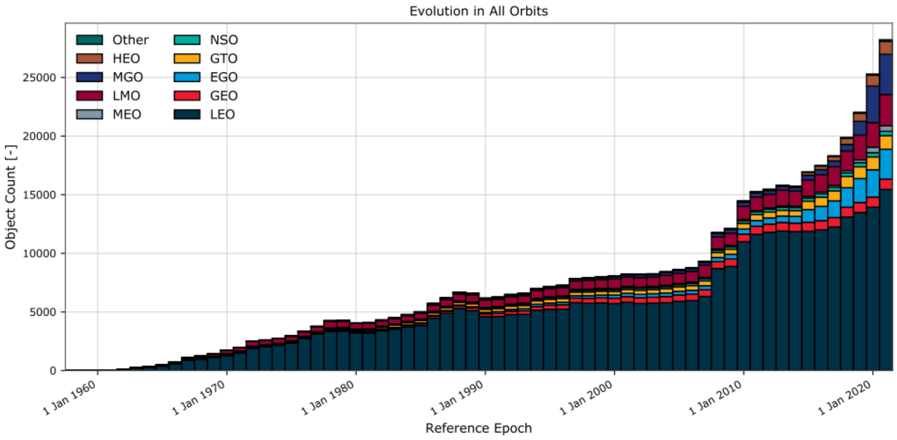

Figure 3.4: The graph shows how the distribution of objects in different orbits have changed over time. At least for the cataloged part of the space infrastructure. Plot taken from [ESA21].

tremendously.

Let us do a simplified estimate of this. If we assume the amount of debris ranging in size from 1 to 10 cm to be about 900, 000, in agreement with Eq. 3.1. The ratio of small-sized debris between LEO, excluding rocket bodies and uidentified objects, and all other orbits, is

$$\frac{\text{LEO debris}}{\text{Total debris}} = \frac{10,099}{14,485} \approx 0.697,$$

which is derived from the numbers found in [ESA21, p.44]. Assuming that this ratio is maintained for the smaller size regime as well, we estimate the amount of small-sized debris in LEO to be

$$0.697 \cdot 900,000 \approx 627,483.$$

From this we can compute the relative payload population to be

$$\frac{4,407}{(627,483 + 15,540)} \approx 6.85 \times 10^{-3},$$

which is about 0.69%. I.e. more than 99% of all LEO objects could be considered to be debris if the estimates are adaptable to the true scenario. The values used in the estimates are captured from [ESA21, ESA20a].

Some orbits have perigee heights that are below 2, 000 km and apogee altitudes well above. Meaning that a portion of the trajectories intersect with the LEO-environment. However, we have not included objects in these orbits in the previous outline – only those fully residing at altitudes below 2, 000 km. Hence, those identified with the darkest color in Figure 3.4.

3.6.1 Inclination density in LEO

Figure 3.5 shows how structures orbiting in LEO are distributed with respect to perigee altitude, h_p, and inclination, i.

The subscript entering "LEO_{IADC}" implies that the Low-Earth orbit are acknowledged as a protected region, as officially stated by the IADC.[20] Thus, the orbital region should be recognized by its unique nature, and as a irreplaceable resource, by anyone who decides to place their spacecrafts herein. Within this region operators are strongly encouraged to follow the mitigation guidelines that apply, as to minimize further generation of space debris, and to ensure a sustainable use of the LEO-environment [Int20].

Upon inspection of Figure 3.4 it is clear that some regions are more favored than others. In terms of height, the interval extending from 500 km to 1, 000 contains the majority of the population, in particular for inclinations greater than 60°. The general understanding is that satellites in LEO are most often placed in *polar orbits*, meaning that their inclination are typically set to $i = 90 \pm 20°$. The primary reason being that satellites in such orbits are capable of covering a bulk of the Earth surface within a relatively short time frame[21], since their movement form a large angle with respect to the rotation of Earth [ESA20b].

There are distinctive object occurrences found at inclinations of $i = 100 \pm 5°$. These are called Sun-synchronous orbit (SSO), and are particularly exploited for Earth Observation satellites. Here, the secular variation of the RAAN, matches the Earth's rotation rate around the Sun. As a result, satellites in these orbits pass over the same geographic location at similar times each day, which is advantageous when monitoring the short-term, as well as the long-term, change of the same surface areas.[22] It is worth stressing that the inclination which provides this *sun-synchronous*-property is dependent on the altitude of the orbit. E.g. an inclination of 96° is a SSO if the height of the orbit is about 176 km. Meanwhile, an altitude of 800 km offers this feature if the inclination is ≈ 98.6°. In terms of minimizing aerodynamic perturbations – and thereby extending the lifetime of the mission – the higher altitude is the superior choice of the two. Typically, Earth Observation satellites are found within the altitude range of 600–1000 km, corresponding to inclinations of ≈ 97.8° to ≈ 99.5°. This is

---

[20] GEO is also regarded as a *protected* region.

[21] If you were to unfold the Earth into a 2D-diagram (also known as a map..), the satellite trajectory would manifest itself, along the North–South-axis, in the shape of a sinusoidal curve.

[22] Earth observation satellites typically complete 14 to 15 orbits per day, enabling extensive ground coverage for a short amount of time. This allows a single satellite to provide accurate intel on the geological progression of numerous individual surface areas, during its mission period.

in agreement with what we observe in Figure 3.5. Evidently, the inclination needs to be larger when the altitude of the orbit is raised [Kli10, ESA21].

Other high-populated inclinations include $i \approx 82°$, $i \approx 75°$, $i \approx 64 \pm 1°$, and $i \approx 55°$. The latter two we do not expect to observe in the measurements,[23] but we can point out that $i \approx 63.4°$, is called the *critical inclination*. Any further elaboration will not be provided here, thus for more details about this, the reader is asked to consult with [Kli10].

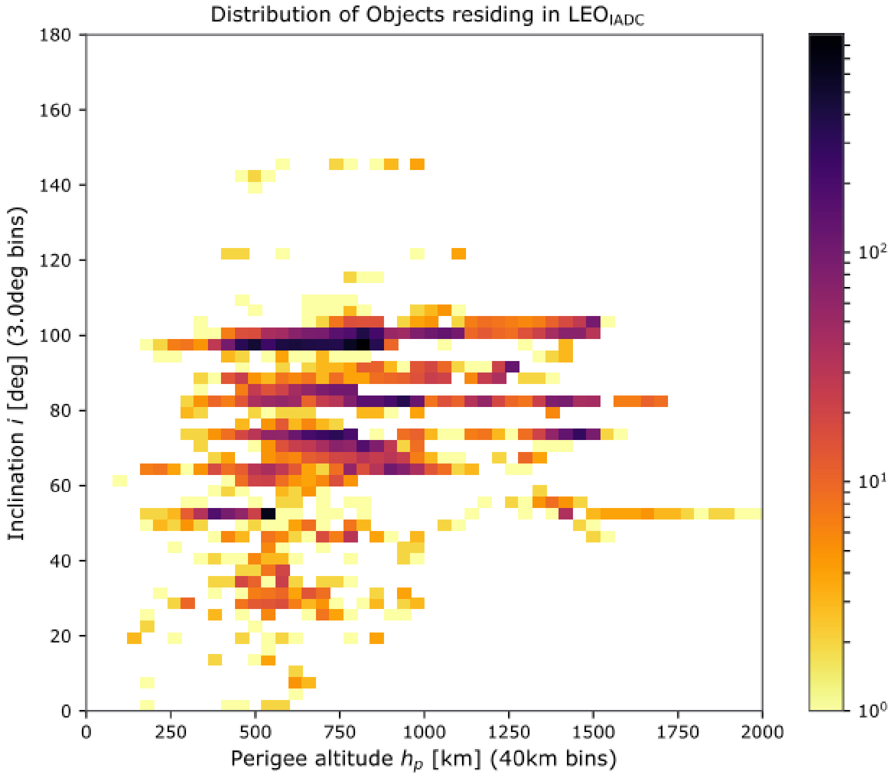

Figure 3.5: Object distribution in LEO, as a function of perigee altitude and inclination. The figure is captured from [ESA21].

---

[23] Since the latitude of EISCAT UHF Tromsø is about 69°, and we are pointing the radar antenna directly eastwards. Thus, objects in lower inclinations are not expected to traverse through the radar beam. The sidelobes of the antenna beam may detect some objects at slight lower latitudes, but this will only be possible if the object is large enough.

3.7 Consequences of space debris

It might not seem evident why space debris is so dangerous, given that the majority of them is below a size of ten centimetres in diameter – a length that is less than the height of a conventional 33 cl soda can. For instance, a spherical debris particle of this size ($d = 10$ cm) solely made of aluminium[24] would have a mass of

$$m = \frac{4\pi}{3} r^3 \rho_{\text{al}}$$
$$m \approx 1.4 \text{ kg},$$

since the radius $r = 0.5d$, and the mass density of aluminium, $\rho_{\text{al}} = 2.7 \text{ gcm}^{-3}$. The first term is the volume of a sphere. In an Earth reference frame this is not a very massive object. But space debris travels at extraordinary high velocities, at so-called *hypervelocities*.[25] For circular orbits, the orbital velocity, v, of an object at height, h, can be found by

$$v = \sqrt{\frac{GM_E}{R_E + h}},$$

where G is the universal gravitational constant, M_E is the mass of Earth, and R_E the average Earth radius. [26] An object residing in an orbital height of 800 km for instance, would then have a velocity of approximately 7.5 km/s, which is equal to 27000 km/h.

If a collision takes place between a target, e.g. a satellite, and a debris particle, the impact velocity Δv is the relative velocity shared between them. This can potentially exceed both object's independent velocities. For the time being, let us assume that the target velocity v_t, is the same as the debris velocity v_d, and that the two objects are located in circular orbits at an altitude of 800 km. Further, we let their orbital inclination be dissimilar, such that they can collide where their orbits intersect. The impact velocity can then be estimated as

$$\Delta v = 2v_d \cos(A), \tag{3.2}$$

where A is the impact azimuth angle. When $v_d = v_t = 7.5$ km/s, as we found before, and choosing an arbitrary azimuth angle, say $A = 48°$, we would have an impact velocity of about 10 km/s. The only way the two objects on circular orbits can collide is if $A \in (-90°, +90°)$. Based on Eq. 3.2, the smaller the relative collision angle A is in this case, the larger is the impact velocity [Kli10]. That is, for smaller absolute values of the azimuth angle, $|A|$.

---

[24] A material frequently used in soda cans as well.

[25] Velocities that are exceeding the speed of sound in solid materials, typically higher than 4 km/s.

[26] $G \approx 6.67 \times 10^{-11}$ m^{3}kg^{-1}s^{-2}. $M_E \approx 5.97 \times 10^{24}$ kg. $R_E \approx 6371$ km.

To obtain an impression of the energy extent that comes into play when hypervelocity collisions occur, one can view Table 3.2. This table holds the mass and kinetic energy of a selection of space debris sizes. Here we have assumed that all particles are solely composed of aluminium, and that they are in the shape of a sphere. In these computations, the mass of the target has not been considered, as this table is merely put in place to highlight how much the energy input changes with respect to the size of the debris particle. To calculate the energy, we have used the equation for kinetic energy

$$E_k = \frac{1}{2} m \Delta v^2.$$

The impact speed is $\Delta v = 10$ km/s, and m is the mass of the debris particle. To obtain an impression of the associated energy magnitudes, a column of Table 3.2 containing rather informal energy comparisons is included.[27]

---

[27] The accuracy of these comparisons may be questioned, and should in any case be regarded as ball-park estimates of the listed energies. I will not claim that I possess all of this weird knowledge before-hand, as many questionable online search words such as "what is the mass of a car" have been used in its making. The credibility of the sources has not been given a lot of emphasis in the making, thus the validity of the values should be taken with a pinch of salt.

Table 3.2: The table holds masses and energies for different sizes of space debris, including energy comparisons of other objects.

d	mass (kg)	Kinetic energy	This is an energy similar to....
1 mm	1.4×10^{-6}	71 J	A golf ball travelling at 200 km/h.
5 mm	1.8×10^{-4}	8.8 kJ	An obese Usain Bolt (114 kg) running at his top speed (45 km/h).
1 cm	1.4×10^{-3}	71 kJ	A car traveling at 30 km/h
5 cm	0.18	8.8 MJ	A medium-sized bus driving at 100 km/h
10 cm	1.4	71 MJ	17 kg of TNT (≈300 hand grenades)
20 cm	11.3	566 MJ	135 kg of TNT

3.8 Breakup Model

To estimate the number of debris objects generated in a fragmentation event, a breakup model needs to be applied. Here we will use NASA's EVOLVE 4.0, covered in [JKLAM01], to make ball-park estimates of the size distribution of objects stemming from the destruction of Microsat-R. EVOLVE covers explosions as well, but we only regard the collision model here. Results from numerous laboratory tests of hypervelocity impacts form the basis of the model.

When a hypervelocity collison takes place between two objects, the generated fragments follow a power law distribution.[28] It can be expressed as follows

$$N_f(d \geq l_c) = 0.1(M_T)^{0.75} l_c^{-1.71}, \tag{3.3}$$

---

[28] If two quantities, x and y, are depending one another as $x = y^p$, their relation yields a *power law*. Since a relative change in y, will cause a proportional change in x – determined by the power p. The volume of a cube, $V = l^3$, is an example of this. Doubling the length, l, of the cube sides, will expand the volume by a factor of eight (2^3).

meaning that a cumulative number of fragments, N_f, having a size d, which are larger or equal to a characteristic length, l_c, are produced upon impact. The characteristic length (given in meters) is the average of the three principal axes of the particle, i.e. $l_c = (l_x + l_y + l_z)/3$. However, when assuming the debris objects to be spheres, l_c can be regarded as an *equivalent diameter* [Kli10, p.68]. When considering a catastrophic collision, the last term in Eq. 3.3, represents the total mass, M_T, entering the collision, given in kilograms (kg). Hence

$$M_T = m_t + m_p, \tag{3.4}$$

where m_t is the mass of the target, and m_p is the mass of the projectile. The term *catastrophic collision* applies when both objects are completely fragmented in the process. Whereas in a *non-catastrophic collision* only parts of the spacecraft gets damaged, yielding partial fragmentation. For a catastrophic outcome, the relative kinetic energy of the smaller object divided by the mass of the larger one, needs to exceed a specific energy threshold of 40 kJ/kg [JKLAM01]. In an ASAT test, the relative kinetic energy is expected to be substantially larger than this.[29] Thus Microsat-R, and the missile, were totally disintegrated in the impact, and we thereby label it as a catastrophic collision.

We know that the dry mass of Microsat-R was 740 kg. The mass of the interceptor is a bit trickier to obtain. Some sources[30] state that the missile was as massive as 18 tons. How much of this mass actually collided with the satellite, is somewhat ambiguous. But a lot of propulsion is needed to launch a vehicle up to an height of 280 km. Therefore, we will assume that the fuel – along with any booster stages that get detached off during flight – makes up the bulk portion of the total mass, say $\approx$ 90%. This leaves us with a rough estimate for the mass of the kill vehicle of about 1800 kg, i.e. 10%. Hence, the total mass entering the collision can be estimated as

$$M_T = 2540 \text{ kg},$$

when using Eq. 3.4. Inserting this number into Eq. 3.3, we can estimate the distribution of fragments generated in the ASAT-mission:

$$N_f(d \geq l_c) \approx \begin{cases} 1.83 \times 10^3 & \text{for } l_c = 10 \text{ cm}, \\ 9.41 \times 10^4 & \text{for } l_c = 1.0 \text{ cm}, \\ 4.83 \times 10^6 & \text{for } l_c = 1.0 \text{ mm}. \end{cases} \tag{3.5}$$

Once again, it is evident that the fragment population increase substantially when including lower size regimes. It is worth stressing that Eq. 3.5 considers the cumulative number distribution of objects, i.e. all size regimes above (and

---

[29] As a missile typically has a mass of several hundred kilograms.

[30] Such as [PK19].

including) the lower bound, l_c. This differs from the estimates in Eq. 3.1 for instance, where an upper bound are used to limit the populations to distinct size regimes.

How well the estimates in Eq. 3.5 adapt to the true circumstances of the Indian ASAT-test may be argued. The breakup model of EVOLVE 4.0 are implemented empirically [JKLAM01]. Out of the experiments forming the basis of this model, the most massive projectile is on the order of ≈ 0.2 kg. This mass fits well for debris particles. However, for an ASAT-test, the projectile is tremendously more massive – on the order of 9000 in the case of the interceptor considered in this section. The question is if the accuracy of the model is preserved, albeit this monumental mass difference? We are not going to appraise this here, as it is simply beyond the scope of this thesis. However, for a more thorough analysis, additional models may need to be included which address this aspect.

3.9 The Kessler Syndrome

The misfortune of a spacecraft getting destroyed by a hypervelocity collision can be seen as two-folded. **(1)** the operator loses one of its beloved spacecrafts ahead of schedule, which is financially costly in terms of losing valuable income associated with this data source – and expensive in the sense that it would require years to replace.[31] **(2)** The spacecraft is fragmented into numerous objects – each one having a finite probability to collide with additional orbiting structures, and consequently running the risk of repeating the destructive process that lead to their very origin as debris. An event initially harming just the one operator, has evolved into a problem for all operators. Obtaining such a repetitive cycle of collisions can ultimately lead up to one of the most frighted effects within the field of space flight – *The Kessler Syndrome*.

The Kessler Syndrome is named after the scientist Donald J. Kessler. In 1978, he – along with Burton G. Cour-Palais – proposed that an increased space debris population could eventually lead to the formation of a debris belt orbiting our planet, rendering entire orbital regimes useless for operative space missions [KCP78].

As described in the previous section, each debris particle generated in a fragmentation event has a certain probability of colliding, and destroying, a larger orbiting structure. If destroyed, the debris arising from this structure can in

---

[31] replace is here a placeholder covering the entire process of planning, building, launching and placing the vehicle into orbit. Taking into account the salary for the employees as well, it is evident that the economical upset becomes substantial for the operator.

turn collide with yet another satellite, potentially creating even more debris, and so on.

The main issue is that the generated debris will continue to orbit the Earth for a long period of time, especially when located at higher altitudes where the atmospheric density – and consequently the atmospheric drag – is low. As the debris spread in heights, and diffuse across its orbital ring, their associated collision threat is raised. It is evident that the consequence of a collision-cascade is not only probable, but also very dangerous. Such an effect would lead to an exponential growth in objects. This production would be self-sustained if certain orbital bands get overpopulated, meaning that all operative spacecrafts situated here would eventually get destroyed, and transformed into a collective cloud of space garbage.

If this happens it will be impossible to place any new spacecrafts into these regions. Access to valuable orbital regimes will get lost for years, decades, or even centuries of time, depending on the altitude of the orbit. With modern methods, active removal of debris still remains to be a relevant option.

Let us put some numbers to it. An object at an altitude of 500 km use roughly 25 years to deorbit. If we move up to 800 km altitude, its decay time is extended to 150 years. Further, at 1200 km heights, the natural reentry phase for the object can be about 2000 years.[32] Above 2000 km, the decay period can be considered to be indefinite [UNO21].

Based on these numbers, it should be quite obvious that any incident of a Kessler Syndrome would mean a major setback in space technology. Although space is vast, certain orbits offer unique attributes that are invaluable to modern society. As opposed to spacecrafts, these orbits are irreplaceable [GY15].

Analogy

One can think of orbits as the highways of the space infrastructure [GY15]. Just like we need roads to drive our ground-situated vehicles, we need orbits to operate our space-situated vehicles. To extend this analogy, an orbit overcrowded with debris, would have a somewhat similar threat to its operating structures, as a highway randomly equipped with landmines. Driving on this road for a short period of time might leave your vehicle unharmed, however, with every extended time you continue your travel, you increase the risk of driving your vehicle towards destruction.[33] Analogously, a spacecraft placed into an orbit

[32] By this time, the satellite operator may have replaced its crew..

[33] No humans were harmed in the making of this example.

plunging with debris, is not synonymous with immediate destruction, but the risk of impact – continuously increasing – will simply be too high to ensure profitable operation.

Should we be worried?

Presumably, no orbits have currently reached the extreme levels of contamination that is exhibited in a Kessler Syndrome. I say ’presumably’, because this is a debated subject on which scientists disagree. The reason is the difficulty in predicting whether or not such a collision cascade is currently elapsing, since we do not know the timeframe of such an event, nor what the exact capacity of an orbit is, before it is overpopulated. Since most debris are too small to be tracked, the exact population of objects in orbits cannot be determined precisely. It can very well be that certain orbits are beyond the tipping point[34] already, and that a collision cascade has thus begun to elapse. However, we will not be making this conclusion here. With that being said, the thickest belts of debris are currently found at 650–1000 km, and towards 1400 km altitude. This is evident from Figure 3.5. Thus, these regions in LEO pose as the most likely candidates to be disrupted by a Kessler Syndrome [UJO20].

One thing that is certain, is that the current launch rate will make Low-Earth Orbits a much more crowded place. As the new mega-constellations of *Starlink* and *OneWeb* are currently in the making, the amount of satellites at certain altitudes are expected to grow substantially in the near future. Although these constellations will be useful resources to society, it does not suppress the fact that their presence may increase the accumulation of space debris. In fact, a recent study conducted by [BB21], estimated that the planned Starlink configuration at an orbital shell of 550 km, may have a collision risk of 50%, if an amount of 230 untracked debris fragments were to travel through this shell at any given time. Given the large breakup events (covered in Section 3.4) occurring at altitudes a bit higher over a decade ago, it is reasonable to suspect that some of these fragments – or other debris for that matter – may decent through this region any time soon. It should be pointed out that operators are aware of the growing threat that space debris impose, and are generally designing their missions according to debris mitigation guidelines, in order to maintain sustainable space operations when heading into the future [Int20].

---

[34] The tipping point refers to the maximum amount of objects that can coexist in an orbit, before a collision-cascade is inevitable.

3.9.1 Potential costs of giving up valuable orbits

A lot of money goes into space activity, and the bulk of it is connected to the satellite industry. According to the Satellite Industry Association (SIA), the global revenues of this industry were 271 billion USD in 2019. This accounts for 74 % of the entire space economy[35]. Of these revenues, 48 % are bound up in ground equipment, and 45 % of the values go to financing satellite services [SIA20]. Thus, rendering satellites useless comes with a financial penalty for ground stations – as they lose the very sources that provide them with data. A long-term evolution of this would ultimately lead to retirement of the ground station, which would cause people to lose their jobs. However, the major societal penalty is the loss of data in itself.

The tendency of society becoming increasingly reliant on the satellites services is evident. Through smart phones and other high-technological components, a large portion of the human population have continuously access to an immense flow of information. A lot of this information comes from interactive communication with satellites. Numerous services are provided by these orbiting structures, and their associated features are always expanding. However, some of these applications may diminish, as their associated satellites are facing a considerable threat of destruction. This is because their main operational domain may involve orbits where the space debris population are growing.

Polar-orbiting satellites providing weather forecasting[36] and Earth observation,[37] are particularly vulnerable to debris. The attributes provided by these satellites are invaluable. These include prediction of extreme weather, avalanches, wildfires, or other natural disasters; monitoring glaciers and polar caps, detecting oil spills, etc. Based on this list, we can see that some of these services help to save human lives[38] – in that case these satellites act as suppliers of life-aiding support. Getting deprived of these functionalities would not only entail a financial upset, but inherit societal and ecological consequences as well. Taking into account the environmental and climatic crisis the world is facing, it is paramount that these assets get preserved [UJO20].

Only a fraction of the potential debris consequences has been mentioned in this section. For a further discussion on the topic, the reader is encouraged to consult with [UJO20].

---

35. The remainder is covered by the non-satellite industry; commercial human spaceflight etc.
36. Usually situated at altitudes between 800 and 830 km.
37. The typical operational regimes for Earth observation includes altitudes of 600-900 km, with the lower 100 km of this interval being the most common for this purpose.
38. E.g. in fragile neighbourhoods, timely warnings of hurricanes, may serve as the difference between life and death.

4

Radar

The term RADAR is actually an acronym for RAdio Detection And Ranging – which is an accurate description of the technique that many modern remote sensing systems exploits. Nowadays, the word *radar* is more associated with the actual systems (or devices) that make use of this technique, rather than the technique itself. Therefore, we will from this stage forward refer to radars as the detection systems, and consequently drop the capitalization of the word (unless we explicitly talk about the technique).

Radars are used in several instances of society, as it provides valuable support to many fields of operations – in scientific studies, military services, as well as for navigation purposes, to mention some. Moreover, radars are essential attributes in the investigation, and monitoring, of the space environment and infrastructure – both onboard satellites, and as key installations at ground stations. For the purpose of this thesis, the focus will be on the latter. In this chapter we will go through some of the basics of radar technology, and discuss how radars are used to monitor the space debris environment.

4.1 The Radio Window

Just like the pupil of a human eye, radars use electromagnetic (EM) radiation to gather information. Unlike the human eye, many radars can generate and transmit this radiation as well. Moreover, these two sensors operate in different portions of the EM-spectrum – which in fact is, to some extent, an explanation for why these two sensors are so different in size.[1] A human eye are only able to see radiation that has wavelengths, λ, stretching from 0.38 µm to 0.78 µm – called visible light. Whereas a radar operates at much higher wavelengths, typically at either the microwave or the radiowave portion of the spectrum. The wavelength(s) chosen, depends on the application the particular radar should have, as different wavelengths offers different attributes. Common for most ground based-radars, is that they operate inside the so-called radio window of the EM-spectrum – named such because the atmosphere remains nearly transparent for transmission at these wavelengths. That is, the transmission experience almost no limitation caused by atmospheric attenuation (negligible compared to other wavelengths). This makes the radar a reliable detection device, since it can operate all hours of the day regardless of the weather conditions.[2]

4.2 Frequency bands

The portion of the radio window that is most useful for the purpose of debris studies is the wavelength band of $\lambda \in [1\text{cm}, 10\text{m}]$ [Kli10]. This also applies to debris studies conducted with the Tromsø EISCAT UHF radar system, as it transmits signals with a wavelength of about 32.2 cm, which translates to a frequency of $\approx$ 931 MHz. These values relates to the UHF-band of the radio spectrum, hence the name of the radar. The UHF-band, along with other designated frequency bands useful for debris studies, are included in Table 4.1.

Although it is conventional to use the frequency to designate radio bands, Table 4.1 are sorted by ascending orders of wavelengths, as displayed in the middle column of the table. The corresponding frequency ranges are included in the right column. Logically, these occur in descending order due to the transmission frequency, f, being inversely proportional to the wavelength, λ. This relation is expressed as

$$f = \frac{c}{\lambda}, \tag{4.1}$$

where $c = 2.998 \times 10^8$ m/s is the speed of light in vacuum.[3] Eq. 4.1 is not

---

1. More complex factors do apply of course, but the angular resolution for any sensor device can be stated to be proportional to the ratio between the wavelength λ and the diameter of the aperture D. Thus, since radio waves are much longer than visible light, a radar needs to be significantly larger than an eye in order to obtain the same resolution. However, the resolution of an eye is superior to that of modern radars.
2. Since most radio transmission are not limited with resonances from water vapor molecules, clouds do not pose any significant challenge.
3. The speed of light depends on the medium it propagates in, and therefore can be a bit

unique for radio signals, as it is a fundamental property describing all forms of electromagnetic waves.

Table 4.1: The frequency bands in the radio window which are useful for debris studies, sorted by ascending order of wavelengths. Values are captured from [Kli10, p.35].

Band designation	Wavelength range (cm)	Frequency range (GHz)
K_u	1.67 – 2.5	18 – 12
X	2.5 – 3.75	12 – 8.0
C	3.75 – 7.5	8.0 – 4.0
S	7.5 – 15	4.0 – 2.0
L	15 – 30	2.0 – 1.0
UHF	30 – 100	1.0 – 0.3
VHF	100 – 1000	0.3 – 0.03

4.3 Type and structure of Radars

Numerous radar systems are located around the globe. All of which can be divided into two basic types, phased array, and the traditional reflector antenna. Since the EISCAT UHF belongs to the second category, our main focus will be on the reflector antenna, before moving on to talk about the specifics of the EISCAT UHF. A brief explanation of the phased array antenna will be given, but first we will provide a short description on the basic parts found in most radar systems.

4.3.1 Radar hardware

Among the essential parts making up a radar, we have; the transmitter, the duplexer, the antenna, and the receiver. A radar may be a transmit-only or a receive-only site, in which case it will lack a receiver, or a transmitter. Consequently, such a radar will not need a duplexer. However, this is included here, since we are using a monostatic radar in our measurements.

Transmitter. The role of the radar transmitter is to generate the signal going to be transmitted – often in the form of short successive high power pulses. The basic waveform is generated at low power by a waveform generator,

---

smaller than the respective value. However, in air the radiation speed is estimated as $\approx 0.9997 \cdot c$. Across relatively short distances, such as in debris detection, this yields an insignificant effect. Thus, we can safely disregard it.

before entering the power amplifier of the transmitter. The amplification can be done in several ways, but a popular choice involves the use of klystrons – high power vaccuum tubes which amplifies the signal by injecting electron beams. Apart from being able to generate high power signals with stable waveforms, it is essential for a transmitter to provide high efficiency [Sko08, ch.1.1].

Duplexer. The duplexer enables a radar to alternate between transmission and reception mode during measurements. When the transmitter is on, the duplexer protects the radar receiver, by preventing the high-power transmission to accidentally enter the radar receiver.[4] Turning off the transmitter switches the radar to reception mode, and the duplexer work to guide the echo into the receiver. Some sort of gas-discharge device is often used as a duplexer [Sko08, ch.1.1].

Antenna. The role of a radar antenna is two-folded. During transmission the antenna concentrates the energy into a narrow beam, which is directed along the antennas line-of-sight (LOS). Upon reception, the signal is collected by the antenna aperture reflected back to the radar receiver. The performance and capabilities of a radar are highly influenced by the antenna structure and characteristics.

Receiver. In the radar receiver one tries to separate the desired signal from the noise, followed by sufficient amplification of the signal such that one can decide whether or not a detection has been made [Sko08]. For measurements of space debris, the desired signal is the radar echo that has been back-scattered by an object. The radar receiver is somewhat more complex in its outline, and a detailed description of it is beyond the scope of this thesis. For this reason, the reader is referred to [Sko08, ch.1.1] for a thorough explanation of what is called a *superheterodyne receiver*, which is the most common type. Likewise, to read upon the receiver system used in the EISCAT UHF, an accurate description is provided in [MLHV02, ch.3.1].

4.3.2 Phased Array Antenna

A phased array antenna is composed of several thousand sub-radiators, arranged in a planar array. Combining the elements into sub-arrays, one can produce a synthetic beam through interference, i.e. superposition, of the phased outputs of the radiators. The planar configuration limits the beam pointing capability to be about 60° from the vertical of the plane, giving a single array

---

[4] If the transmission – which can be on the order of megawatts – were to enter the receiver, it would instantly destroy its electrical components, as these are not designed to withstand such powerful radiation. The role of the duplexer is therefore of paramount importance.

about 120° coverage. Thus, combining three equally spaced array – a 360° coverage is possible to obtain. The phase and amplitude of each radiator can be controlled individually, implying that the antenna beam is possible to steer electronically, rather than mechanical. Some benefits related to the phased array antenna include; rapid change of the beam's pointing direction, and the opportunity of tracking multiple objects at the same time. A downside with the phased array antenna is the quite expensive manufacturing cost. Nevertheless, most of the USSTRATCOM surveillance radars use phased array antennas, as they provide great advantages in monitoring the space object environment [Kli10, Sko08].

4.3.3 Reflector Antennas

The other main type of antennas is the reflector antenna. Named such because it reflects the electromagnetic radiation – coming from a feed system – in the form of a guided-wave, which propagates along the pointing direction of the antenna. Thus, upon transmission, the antenna (here assumed to be in the form of a parabolic dish) concentrates the radiation energy into a narrow beam around its on-axis position, with all parts of the electric field travelling in parallel paths. However, this is only in the idealized case of a pencil beam – a case which never holds true in real-life applications, due to imperfections in the antenna structure and symmetry, among else. Upon reception, the reflector – still assumed to be parabolic – collects and circularize the incoming planar wave echo, reflecting the signal back to the focal point of the reflector, where the antenna feed system is mounted. One can think of the feed system as what connects the transmitter and receiver to the antenna, and thus they can generally be regarded as co-located [Sko08, Chr].

One can distinguish between different reflectors by the geometry of the aperture, along with the feed system used to illuminate the surface. The reflector type are carefully chosen with respect to the field of research for the particular radar. Simple sketches for several kinds of reflectors are illustrated in Figure 4.1. It is not unusual to use combinations and variations of these basic types in modern antenna design, with a primary goal of minimizing loss and (spurious) sidelobes in the beam pattern [Sko08, ch.6.3].

We will not describe all of the reflector types here, as it would be redundant with respect to the objective of this thesis. Since the EISCAT UHF is equipped with a Cassegrain antenna (Figure 4.1(f)), we will limit our discussion to concern this type, although much of the following may apply to reflector antennas in general.

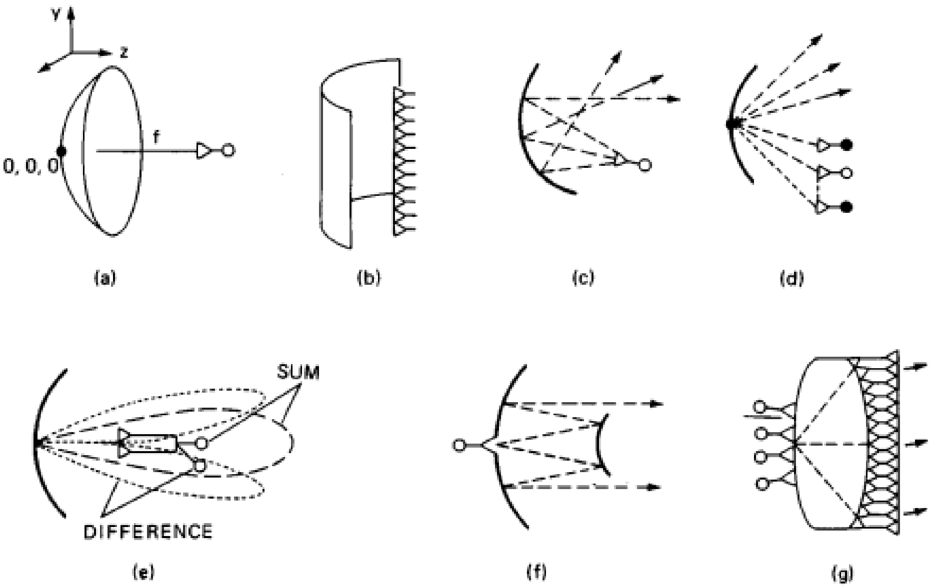

Figure 4.1: Basic types of reflector antennas. (a) Paraboloid. (b) Parabolic cylinder. (c) Shaped. (d) Stacked beam. (e) Monopulse. (f) Cassegrain. (g) Lens. Figure and explanation are captured from [Sko08].

4.3.4 EISCAT UHF Tromsø

Like most other reflector antennas, the EISCAT UHF is equipped with an antenna that is steerable in two directions; within the local horizontal plane – represented by a azimuth angle α; and in the local vertical plane – with the elevation angle ϕ representing the degree of elevation. These planes are perpendicular to one another [Kli10].

In other words, the azimuth angle indicates in which cardinal direction the antenna is pointing, with respect to north. For instance, an azimuth of 0° means that the antenna is pointing directly northward, while an azimuth angle of 90° implies that the antenna is pointed directly eastwards – which is the case for the four experiments that are presented in this thesis. The elevation angle, on the other hand, is the angle from the local horizontal plane (spanning from the antenna), to the pointing direction of the antenna. An elevation of 0° means the antenna is pointing towards the local horizon, while an elevation of 90° implies a pointing towards the local zenith. In the experiments that will be presented later on, an elevation angle of 75° has been used.

In order to provide a more intuitive description to the concept of azimuth and elevation, we draw an analogy to the human head. Suppose you are standing straight with your feet pointing directly towards north, and with your sight fixed, i.e. not moving your eyes. Then, the amount you rotate your head towards your right will decide the azimuth angle. Similarly, the degree you tilt your head backwards from its resting position will determine the elevation angle. A head rotation of 90° to the right [5], along with a backwards tilt of 75°, would have allowed you to copy the antenna pointing direction used in the four beam park experiments. Figure 4.2 shows EISCAT UHF with this pointing direction.

Figure 4.2: The EISCAT UHF radar at experiment day – 12/04/2021. In the image the radar is set to the appropriate pointing direction.

4.3.5 More on EISCAT

The specifications for the EISCAT UHF radar are listed in Table 4.2.

Located at Ramfjordmoen (69°35′N, 19°14′E), just outside the city of Tromsø, Norway – the EISCAT UHF is a HPLA-radar operated by the EISCAT Scientific Association. Along with a VHF-radar at the same location, UHF receivers located at Kiruna, Sweden (67°52′N, 20°26′E) and Sodankylä, Finland (67°22′N,

---

[5] Your chin should align with your right shoulder. Unfortunately though, the human anatomy prevents this from being possible for an average person.

26°38′E), and two UHF radars located outside of Longyearbyen, Svalbard (78°09′N, 16°01′E), the EISCAT facilities have for some time been the most advanced network of incoherent scatter radars in the world. In particular, they have been providing valuable data for decades in the field of ionospheric research. Until recently the Tromsø UHF site, along with remote receivers at Kiruna and Sodankylä, operated at the same frequency of 931 MHz[6] – thus forming a tristatic radar system. However, in recent time, the Kiruna and Sodankylä-sites were converted to 224 MHz-frequency, to support operations in the VHF-band [EIS10, EIS18].

Table 4.2: Specifics for EISCAT UHF Tromsø. Values are adapted from [EIS18, Wan05].

Geographic coordinates	69°35′N, 19°14′E
Altitude (m)	86
Frequency (MHz)	929
Maximum bandwidth (MHz)	8
Transmitter	2 Klystrons
Channels	6
Peak Power (MW)	2.0
Average power (MW)	0.25
Pulse duration (ms)	0.001–2.0
Phase coding	Binary
Minimum interpulse period (ms)	1.0
System Temperature (K)	90–100
– Antenna specifications –	
Geometry	Steerable parabolic dish
Feed system	Cassegrain
Main reflector diameter (m)	32.0
Subreflector diameter (m)	4.58
On-axis Gain (dBi)	48.1
Polarization	Circular

The EISCAT Association goes an exciting time ahead, as they seek to extend their radar park with the upcoming launch of EISCAT 3D – currently under construction. Once it gets set into operation it will be the most comprehensive of the EISCAT systems, and will make use of phased array antennas for transmission and reception. In a two-stage plan, the radar will initially consist of a transmit and receive site located in Skibotn, Norway, and two receive sites located at Karesuvanto, Finland and Bergfors, Sweden, respectively. While the next stage involves two additional receiver sites at Jokkmokk, Sweden, and Andøya, Norway. As with the other EISCAT facilities, the main scientific pur-

---

[6] The frequency of 931 MHz were used until a couple of years ago. This was later changed, and the EISCAT UHF Tromsø is now operating at a frequency of 929 MHz.

pose of EISCAT 3D will not be space debris research, but atmospheric studies – regardless, it was shown in [VMK+17] how this radar also can be used for space debris measurements. The same thing goes for EISCAT UHF, as was first shown by Markkanen et. al. in 2002 [MLHV02].

4.4 The Radar Equation

One of the most fundamental equations when it comes to radar applications is the radar equation. Though it has been presented in several forms in radar literature, we are not going to discuss all of them here, but focus on what applies to detection of a point target, which is what a space object can be regarded as. The following form of the equation is adapted from [Sko08, ch. 1.2], and much of the content of this section is inspired by this book. We will only consider the monostatic case here – meaning that the same radar site is transmitting and receiving the signal, but the formulas can easily be adapted to fit other cases with some slight adjustments.

The signal power that a radar receives, P_r, can be expressed as

$$P_r = \frac{P_t G}{4\pi R^2} \times \frac{\sigma}{4\pi R^2} \times A_e. \tag{4.2}$$

The product on the right hand side is here written as three terms, so as to reflect the three-step propagation process, which can interpreted as the following.

First, a radar antenna of gain G transmits a signal of power P_t, which propagates outwards uniformly in all directions[7] along a distance R (called range). I.e. the power of the signal decreases at a rate proportional to R^{-2}. At an range R, the signal interacts with a target of a radar cross-section (RCS), σ, which scatters some portion of the signal back to the radar system, covering the same distance R. Thus, the product of the first two terms describe the power density of the signal that gets returned to the radar system after completing the two-way travel. This signal is referred to as *the radar echo*. Lastly, a portion of this radar echo gets collected with the radar antenna – determined by its effective aperture area A_e – which in turn directs the signal back to the radar receiver, and reception is made [Sko08].

Since the same antenna is both transmitting and receiving the signal in a monostatic case, we can rewrite A_e in terms of the antenna gain G, and the

---

[7] Here the ideal case of an isotropic radiator is assumed. One should note that this is at best an approximation to real-life applications, since an isotropic radiator only exists in theory.

transmission wavelength λ, by making use of the following relation,

$$A_e = \frac{G\lambda^2}{4\pi}. \tag{4.3}$$

It is often preferred to make use of this, as the wavelength (or frequency) of transmission is an important property that is associated with a particular radar facility, and is therefore common knowledge to have before conducting measurements. In many cases, the same goes for the gain G as well. However, this is a more variable quantity as it depends on the surrounding conditions and structure of the antenna, making it necessary to take routine measurements of this from time to time, in order to possess accurate knowledge about the antenna gain prior to experiments. It is worth mentioning here that the G entering Equation (4.2) and **??**, represents the peak (or on-axis) gain. This is the gain related to the on-axis position of the antenna beam. It is basically a measure of how much signal power residing along the on-axis position of the beam. However, upon transmission, the signal power is not all contained in the beam's on-axis, but will rather distribute itself in a pattern, known as the *antenna beam pattern*.

Returning to the radar equation, we can gather the terms, and use Eq. 4.3 to rewrite Eq. 4.2, yielding the following expression

$$P_r = \frac{P_t G^2 \sigma \lambda^2}{(4\pi)^3 R^4}. \tag{4.4}$$

One can also make some additional adjustments to Eq. 4.4, in order to give a better approximation to real life applications. Essentially, the current form of the equation describes a target-detection occurring at the on-axis position of the beam, i.e. in the beam maxima. Moreover, Eq. 4.4 assumes the signal is traveling in free space, as no propagation effects – that can alter the signal strength – are taken into account. A way to address these issues, is by adding a propagation factor F into the numerator of the equation, which take atmospheric propagation effects, such as absorption, refraction, etc., into consideration, as well as the possibility of measuring a target away from the maximum of the beam. The radar equation will then be

$$P_r = \frac{P_t G^2 \sigma \lambda^2 F^4}{(4\pi)^3 R^4}, \tag{4.5}$$

where the propagation factor F is raised to the fourth power, so as to account for the atmospheric effects that are encountered by the signal both on its propagation from the radar to the target, and on its reversed path. Though Eq. 4.5 might serve as a better approximation for real-life applications, we will stick with Eq. 4.4 as our primary notation for the radar equation, in the remainder of this thesis. In doing this we will assume that the gain G is dependent on θ – the angle between the direction of observation and the optical axis of the beam – and hence we preserve the possibility that detection can occur in a greater portion of the antenna beam other than just in the on-axis beam (i.e. where $\theta = 0$). As stated in Section 4.1, atmospheric attenuation is minimized for radiation inside the radio window of the EM-spectrum, which is why we will neglect these effects altogether, by setting the propagation factor $F = 1$ [Sko08].

Due note that this is only an approximation. In reality the signals will experience propagation effects. Particularly the ionospheric plasma can alter the properties of the signal. This is however not something we will discuss, which is why we simplify things by neglecting it.

4.4.1 Signal-to-Noise Ratio

When performing radar measurements we will always need to deal with the presence of noise. It can appear as background radiation arising from external sources that enter the radar receiver along with the echo returning from a target. An active way of limiting this external noise, is to place the radar systems at a rather remote location, and by choosing a rather "unique" transmission frequency which does not interact with the frequency used by other services, such as cellphones. Internal or thermal noise, on the other hand, is not possible to effectively eliminate actively. This type of noise arise as a result of currents being generated by random thermal fluctuations, taking place between atoms and electrons in the electrical circuits of the radar system. Every resistor in the circuit will then be responsible for generating an electrical power $k_B T$, where k_B is the Boltzmann constant, and T is the resistor temperature. It is inconvenient to treat these noise sources individually, as the noise can be summed together when several independent sources are included in a system. This makes the collective noise power dependent on the system noise temperature T_s [K]. Moreover, noise power is additive across different frequency ranges, which means that the collective noise power P_n that enters the measurements, can be expressed

$$P_n = k_B T_s B, \tag{4.6}$$

where k_B is the Boltzmann constant (1.38×10^{-23} W s K^{-1}), and B denotes the effective noise bandwidth in hertz. It needs to be pointed out that noise is a complex quantity with highly irregular and unpredictable waveforms, as opposed to the well-behaved transmitted signal, which makes it difficult to infer its true value. Thus, the equality sign in Eq. 4.6 should be treated with caution, as it is merely an estimate of the noise power [Sko08, ST11].

Since the noise mixes with the radar echo upon reception, it is basically impossible to distinguish between the two quantities. The signal power entering the radar receiver is therefore a combination of the radar echo and the noise. This highlights the importance of a quantity known as the signal-to-noise ratio (SNR), yielding the mathematical notation; S/N. One can think of it as the ratio between the (desired) power of the signal, and the undesired noise power. Expressed mathematically, we have

$$\left(\frac{S}{N}\right) = \frac{P_r}{P_n}, \tag{4.7}$$

where P_r is the power at the receiver input, and P_n is the noise power at the receiver. Inserting Eq. 4.4, and Eq. 4.6 into Eq. 4.7, we obtain the following expression for the SNR:

$$\left(\frac{S}{N}\right) = \frac{P_t G^2 \sigma \lambda^2}{(4\pi)^3 R^4 k_B T_s B}. \tag{4.8}$$

If a threshold, $(S/N)_{min}$, is determined, one may solve this equation for R, and use it to estimate the maximum range, R_{max}, the radar can detect an object with a certain RCS, σ. Given that all other quantities in Eq. 4.8 are known. This is not going to be outlined here, but the approach is covered in [Sko08].

4.4.2 Detection threshold

For the sake of reliable results it is important to decide upon an appropriate threshold, so as to distinguish between measurements caused by target echos, and noise coming from other sources, i.e. what is a target observation, and what is not. This way, if the received signal power exceeds the threshold – the measurement is recorded and saved as an object detection. But if the echo is too weak, it gets discarded.

It is paramount that this threshold is set to an appropriate value. A too high threshold will result in an underestimation of detections, while a too low threshold will make the radar oversensitive to radiation from other sources. The former results in a sparse, or insufficient, recorded data set. While the latter prompts invalid results corrupted with false detections. Therefore, a compromise between the two extremes is desirable.[8] For most of the space debris experiments conducted with EISCAT UHF, a minimum SNR of 25 has been used as a detectability measure. The value has been chosen empirically, and is based on past test campaigns. Usually, it is preferred to represent the SNR on the more descriptive decibel (dB) scale, in which case the threshold corresponds to $10\log_{10}(25) \approx 14$ dB [Sko08, MLHV02].

---

[8] I.e. the threshold need to keep the rate of false detections adequately low, while maintaining a decent probability for observing the targets of interest, when they propagate through the radar beam.

4.4.3 Energy-to-noise ratio

The content of this section is solely based on the work by J. Markkanen et. al [MLHV02]. Instead of using the directly measurable SNR as a detectability measure, one can use the energy-to-noise ratio (ENR) as a measure to quantify detection probability. Assuming unit noise bandwidth, one can define this as

$$\mathrm{ENR} = \frac{E_s}{k_B T_s}, \tag{4.9}$$

where E_s is the *average* signal energy. With the use of a coherent integrator – i.e. integrating the signal over several pulses – it will have a peak output that is proportional to this signal energy. Then, if the signal is sampled correctly, the sampling interval τ will be the reciprocal of the receiver bandwidth B. The signal energy E_r will then be the product of the received power P_r and the sampling interval. However, when the computation is performed over several samples N, the ENR and SNR yield the following relation:

$$\mathrm{ENR} = \frac{N P_s \tau}{k_B T_s} = \frac{N P_s}{k_B T_s B} = N \cdot \mathrm{SNR}, \tag{4.10}$$

with P_s being the average signal power received. Thus, by extending the integration time, one can amplify the SNR – which is an essential benefit with coherent integration. In turn this prompts for a significant improvement in both the detection sensitivity, and in the parameter estimation accuracy [MLHV02].

4.4.4 Relation between radar cross-section and size

One can see from the radar equation, Eq. 4.4, that the scattered echo power is highly influenced by the value of the RCS, σ, of a target. The nature of this quantity is not only complex, but also dynamic. As it depends on the target's shape, size, and orientation, as well as the electrical conductivity of the material it is made of. In addition to this, the wavelength of the radiation it interacts with, plays an important role [Kli10, MLHV02].

However, since a debris particle is something generated in orbit, the knowledge about its physical characteristics is usually limited. Therefore, it is necessary to make assumptions about the shape and material properties of space objects, such that decent estimates of the RCS can be obtained. A common approach, as outlined in [MLHV02, p.17], is to assume that all space debris objects are perfectly conducting spheres. Invoked in this single statement are assumptions about its material properties, its shape, as well as the implicit assumption about the non-varying orientation of the object, since a sphere is perfectly symmetric. This way, one can obtain a relation of the RCS that depends on the size of the object, and the transmission wavelength, λ. Because the shape is regarded as spherical, we can recognize the size of the object by its diameter d.

When the object diameter is small compared to the wavelength, the target scattering can be described by the Rayleigh approximation, and the RCS, σ, becomes proportional to d^6. For targets with diameter larger than the wavelength, the optical approximation applies. Then the RCS is considered equal to the geometrical cross section of the particle. For a sphere this is the same as the surface area of a circle, i.e. $\pi r^2 = (\pi d^2)/4$.

When the target diameter is similar to the radiation wavelength, it occurs some sort of resonance which cause the RCS to display an oscillatory behaviour. This is called *Mie scattering*. However, since the calculation is already simplified through the assumption of spherical debris, it is rational to neglect the effect of Mie scattering, for the purpose of not over-complicating things. In doing so, the radar cross section can be estimated by

$$\sigma \approx \begin{cases} \dfrac{9\pi^5}{4\lambda^4} d^6, & \text{when } d < \dfrac{\lambda}{\pi\sqrt{3}} \\ \dfrac{1}{4}\pi d^2, & \text{when } d > \dfrac{\lambda}{\pi\sqrt{3}}. \end{cases} \tag{4.11}$$

The top term represents the Rayleigh approximation, while the lower term is the optical approximation. This equation, and the reasoning behind it, are found on [MLHV02, p.17].

EISCAT UHF is operating with a transmission wavelength of 0.322 m, and is thus the value used in the four experiments. Inserting this into Eq. 4.11, the cross-over point between the Rayleigh and optical region occurs at a diameter of ≈ 5.9 cm. With this in mind, we estimate the radar-cross section for a selection of object diameters below, with the complete curve given in Figure 4.3.

$$\begin{aligned} d = 1 \text{ cm} &\Rightarrow \sigma \approx 6.4 \times 10^{-8}, \\ d = 5 \text{ cm} &\Rightarrow \sigma \approx 1.0 \times 10^{-3}, \\ d = 10 \text{ cm} &\Rightarrow \sigma \approx 2.5 \times 10^{-3}, \\ d = 20 \text{ cm} &\Rightarrow \sigma \approx 1.0 \times 10^{-2}. \end{aligned}$$

One can see that an increasing diameter leads to a notable rise in the RCS. Thus, it is evident that the RCS are safe to regard as a quantity specifying the detection probability of a target. This makes EISCAT UHF more sensitive to large sized targets, which are often the case for cataloged objects. Many of them can be detected far into the sidelobes of the antenna beam. On the other hand, the uncataloged portion of the population mainly consist of small sized debris particles. Consequently, the radar is less sensitive to these objects, as they need to enter close to the on-axis beam position, in order to be observed. For the smallest debris the RCS are simply too small to get detected. Based on this we expect the majority of the beam park observations to come from objects found in the catalog [VKM+19].

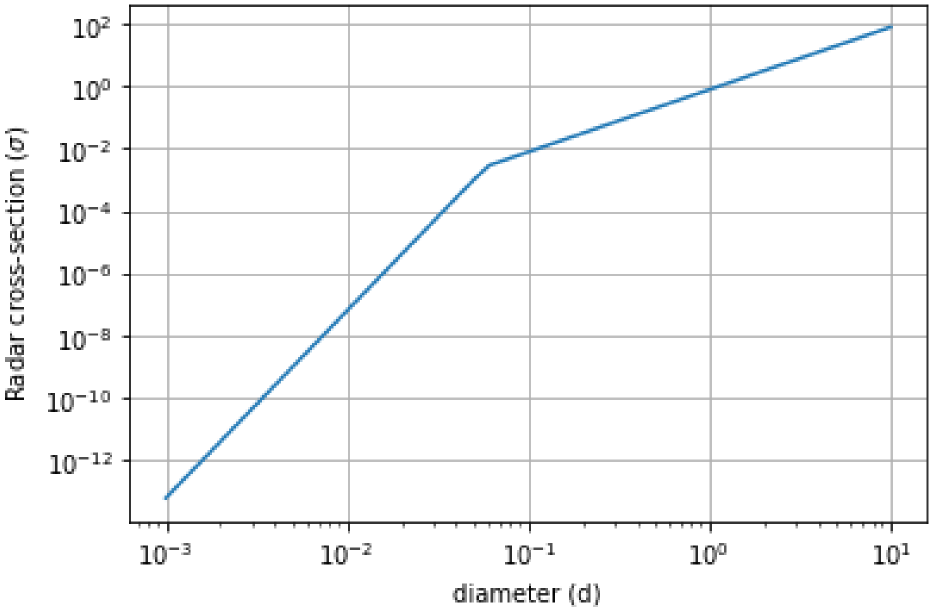

Figure 4.3: Logarithmic plot showing the radar cross section as a function of diameter when using the approximation in Eq. 4.11. The graph is applied for the wavelength used by EISCAT UHF. The diameter is given in meters. Mie scattering is ignored, thus the optical region begins where the Rayleigh region ends. This intersection takes place where the slope of the curve changes.

4.5 Observable parameters

The simple fact that all electromagnetic radiation travels at an enormous pace (i.e. the speed of light), is what make radars – along with other remote sensing devices – so desirable to use. It enables substantial amount of data collection within a short time frame. Speaking of time – most radars are able to measure the round-trip time of a signal, Δt. This is the time that elapses from the signal is transmitted, until it gets received. Thus, the round-trip time is nothing less than

$$\Delta t = t_r - t_t,$$

where t_t is the time of transmission, and t_r is the time of reception. If only one sensor system is performing both the transmission and reception, it is known as a mono-static radar. This is often sufficient in the context of basic debris studies.

Range

Once the round-trip time, Δt, of a measurement is captured, one can derive the range to the target, R, by

$$R = \frac{c\Delta t}{2}, \tag{4.12}$$

with c being the speed of light. We divide by two in order to account for the two-way propagation of the signal. E.g. if the round-trip time of a signal is 6.67 ms, the range to the target is about 1000 km, according to Eq. 4.12.

Though it may be tempting to use altitude in place of range, it is important to distinguish between the two, as they are not the same. The range, sometimes referred to as the slant range, is simply the distance between the target and the radar system, measured along the radar's line-of-sight (LOS). Whilst the altitude is merely the object's height above ground. However, the range serves as an indication of the altitude, and it is possible to estimate the altitude when knowing the range and pointing direction of the antenna.

4.5.1 Doppler shift and Doppler velocity

One of the most fundamental properties in signal theory is the Doppler shift. With high accuracy, the Doppler shift can be used to determine the relative velocity between a target and a receiver. Speed limit enforcement is an example of where the Doppler shift is used in practice.[9] Although the sensors are less advanced than those used at EISCAT, the physical concept is similar for both detection devices.

Consider a transmitted signal characterized with a frequency f_t. When the signal interacts with a conducting target, the target reflects a signal back to the receiver which may have a shift in frequency f_d, given that the target has a relative movement to the receiver. That is, the frequency of the received signal is $f' = f_t + f_d$, where the latter term is known as the Doppler shift. Based on

[9] Equipped with a sensor device that can both transmit and receive an EM-signal, the police can determine if a driver is exceeding the speed limit or not, by bouncing a signal off their vehicle. However, since it is only the relative velocity that gets measured, the policeman should ideally be situated in an overhead position relative to the vehicle.

the relative movement of the target, it can either *compress* or *stretch*[10] the original signal. How the signal is affected depends on whether the target moves towards or away from the radar. However, if the target is moving perpendicular to the radar beam, no relative movement is occurring along the measurement axis of the radar, namely the radar's LOS. In that case, the received frequency will be equal to the transmitted frequency, since no Doppler shift is applied to the signal. After an echo has been received at a radar station, the measured Doppler shift is obtained after some simple signal processing operations have been applied. Knowing this, it is straightforward to calculate the so-called Doppler velocity of the target, which is given by

$$v_d = -c\frac{f_d}{2f_t}, \tag{4.13}$$

where v_d denotes the Doppler velocity, and c is the speed of light. It is important to note that the EISCAT UHF is only capable to measure the velocity component in radial direction, meaning that Eq. 4.13 can only be thought of as a measure of the radial velocity of the detected object, and not its true velocity. To derive this, we would need to know the angle between the object's direction of motion, and the measurement axis. This knowledge is not possible to infer with the current standards of EISCAT UHF [MLHV02, EvZ06].

Another thing which is important to address at this point, is the sign convention of the Doppler velocity. This is because it is ambiguously defined in the literature. The definition we will stick to, which is used in all of our beam-park experiments, is that a **positive** Doppler velocity describes an object moving **away** from the radar – i.e. the range increases. Consequently, when an object moves **towards** the radar, it will have a **negative** Doppler velocity – describing a decrease in range. This is in agreement with the convention used by [MLHV02].

However, to stick with the intuitive interpretation of an away-moving object causing a negative Doppler shift f_d, but a positive velocity v_d (and vice versa) – a minus sign have been inserted in front of the right-hand side of Eq. 4.13. This means that a decrease in frequency of 6.2 kHz ($f_d = -6.2$ kHz), gives a positive Doppler velocity of +1.0 km/s, when a transmit frequency $f_t = 929.3$ MHz is used. Likewise, a Doppler velocity of -1.0 km/s occurs when the initial signal frequency increases with 6.2 kHz.

In addition to being valuable in itself, the Doppler velocity of a target can be used to derive information about its orbital inclination. If the antenna pointing

---

[10] Although not directly transmutable, the Doppler effect can be compared to that of pushing, or pulling a spring out of its rest position. This results in compressing, or stretching the coils of the respect to one another. If the spring represent the signal, the first effect would result in an increase in frequency, while the second would decrease it. Keep in mind that a spring has mass, and radiation does not.

direction is known, this can be estimated numerically. The inclination estimates for the conducted measurements will appear in Section 5.2.

4.6 The meaning of a beam-park experiment

By now, the reader may be acquainted with the term *beam-park experiment* as it has been mentioned several times prior to this section. Therefore, it is about time that we provide some further explanation on this topic. A beam-park experiment, abbreviated BPE, is a way of conducting radar measurements where the pointing direction of the radar beam is set in *parking-mode* during the experiment. I.e. the azimuth and elevation angle of the radar antenna are kept fixed throughout the campaign duration, which for all four BPEs presented in this thesis, were set to 24 hours. The pointing direction appears fixed for a local observer, but the relative pointing direction will vary with the rotation of the Earth.[11] This way the beam position is continuously changing with respect to the space population we are trying to observe.

An experiment time of 24 hours – matching the rotational period of the Earth around its own axis – lets the radar perform one complete "sweep" in the local celestial plane. Although it is difficult to describe this accurately with words, here is an attempt to provide an intuitive visualization: imagine the beam to leave a trace of "paint" in every portion of the sky that it illuminates. Then, after the Earth has completed one revolution, the radar beam would have "painted" something that resembles a ring-like structure above the Earth – when viewing it from the side.[12] The width of the edges of this ring would then be determined by the radar antenna's field-of-view (FOV) (the total collecting area of the antenna beam pattern), and its height will be determined by the range interval where detections can occur. A last note on this analogy is that the ring will be tilted, because of the axial tilt of the Earth.

A key advantage of the EISCAT UHF in terms of space object studies, is its location at a polar latitude. This is great for detecting objects in high-inclined orbits, as objects in these orbits pass over polar latitudes far more often (at near every pass) than at lower latitudes. Furthermore, high-inclined orbits are among the most popular choices for satellite operators, and are consequently

---

[11] The situation is comparable with the diurnal motion of the Sun. Our perception of the Sun moving during the day, is in reality only caused by the diurnal rotation of the Earth. Although we regard our ground position as fixed, it is continuously moving compared to the spatial surroundings.

[12] Sticking a toothpick near the top of an orange, and then rotate the orange through one revolution, resembles the same effect. With the orange being the Earth, and the toothpick representing the radar beam in this analogy.

the most occupied orbits found in LEO, which we saw in Figure 3.5. If the pointing direction of the EISCAT UHF is chosen appropriately, it should be able to detect two passes for most high-inclined objects during the same 24h BPE. These two passes will in case be at different points along the orbit of the object – traversing through the radar beam on its ascending and descending[13] transits [VKM+19].

---

[13] An ascending transit occur when the object is heading towards the apex of the orbit. Likewise a descending transit is detected at a point where the object is traveling away from the apex. With reference to the Earth, these terms may be translated to going northwards, and southwards, respectively.

5

Beam Park Observations

The conventional remote detection devices – such as the radars operated by the SSN – that are used to monitor and track the space infrastructure on a daily basis, are only able to detect objects larger than 10 cm in size. These objects are stored in a catalog[1] in the form of a snapshot for any given day, usually in the Two-Line Element (TLE)-format [Uni21]. But, as previously mentioned in this thesis, the bulk portion of the space debris environment consists of objects that are smaller than 10 cm in size. Since these objects are regarded as "untrackable" with conventional radars, the predictions and monitoring of the orbits of these objects are achieved using statistical models. However, HPLA-radar measurements are used to assist these models, as these radars are capable of detecting objects smaller than 10 cm in diameter – possibly all the way down to 1 cm at the lowest altitudes in LEO. The EISCAT UHF is such a radar. In this and the subsequent chapters, observations captured with this radar will be presented.

5.1 Measurement data

Detailed data from all of the beam-park experiments are listed in Table 5.1. The start- and end times in the table, are the points in time when the first and last detection were made, with the date expressed in day/month-format, and

---

[1] The Spacetrack-catalog (previously called the NORAD-catalog).

the time of day (hour:min:sec) represented in UTC-time. Consequently, the duration of each experiment is here calculated as the time that elapsed between the first and last detection, though the true duration of each experiment might have been slightly longer than this. However, since no further detections were made during this time span, we can safely ignore it. We mention this now, so as to explain why there is a minor difference in the time range of the plots between the different BPEs. Moving ahead the duration of each BPE is regarded to be 24 hours, rounded to the closest hour.

The remaining entries in Table 5.1, in agreement with that stated in [MLHV02], can be explained:

- Name – the designated name that is used for the respective BPE in this thesis.

- P_t – The peak transmission power given in megawatts.

- T_s – The recorded system temperatures in Kelvin.

- N_{det} – the total number of detected objects during the respective BPE.

- Range – the range given in km.

- Alt. – the estimated altitude of the object, calculated from the range, and the pointing direction of the antenna (azimuth and elevation angle).

- v_{dop} – the Doppler velocity of the object relative to the radar given in km/s. This can be found through inspection of the echo's Doppler shift. A positive value means that the object is moving away from the radar.

- a_{dop} – the radial acceleration [km/s^2] of the target, estimated as v_{dop}/dt. This is not available for every detection, as it requires time separated data points to be calculated. This means that the target must be located inside the radar beam for a decent amount of time, such that several echos associated with the same object are received by the radar which exceeds the detection threshold. With several data points at hand, an estimate of a_{dop} can be achieved through a best line fit (or a best parabola fit in this case) to the data points for v_{dop}.

- $\sqrt{SNR}$ – an estimate of the coherent integration. The values stored for each detection are the maximum ratio obtained for the respective object. Table values for these entries are given in an ordinarily linear scale.

- SNR – by squaring the max ratio (previous entry) we obtain estimates for the signal-to-noise ratio recorded for each detection. The table values are given in decibels (dB).

- Event dur. – short for event duration. This is the estimated time that a particular object traverses through the *detectable region* of the radar beam. The detectable region is the portion of the radar beam pattern in which the object is able to scatter an echo of sufficient power to yield a detection. This is highly dependent on the radar cross section of the object, σ, which in turn is a function of its size d, as described in Section 4.4. Therefore, a long event duration are thought to be caused by relatively large space objects, as these can yield detections far into the sidelobes of the beam. This increases the probability of obtaining multiple detections for the same object, as it can get detected at several instances of the beam pattern than a smaller object. The trajectory of the object also needs to enter the radar antenna's FOV.

- $d_{\text{eff,min}}$ – the minimum effective diameter of the object given in cm. Assuming the target is a conducting sphere, its diameter gets approximated by Eq. 4.11. Inserting this into the radar equation, the minimum effective diameter can be estimated when knowing the transmission wavelength and power, on-axis gain, system temperature, and the range to the target. The effective diameter gets estimated as if the object got detected at the on-axis beam position. This typically means that the effective diameter is an underestimation of the true size of the object, since it is more likely that the detection occurred at an off-axis position of the beam than on-axis, as this portion has a far larger collective area. Thus, we give the effective diameter the additional "minimum"-term in front, as to highlight that the object probably was larger than this diameter estimate.

- The last entries of Table 5.1 are those values that remained unchanged for all the four beam-park experiments. These are the wavelength of transmission λ, on-axis gain G, and the antenna pointing direction – determined by the azimuth and elevation angles. Although these angles can slightly vary during the experiment, the maximum recorded change was found to be at an increment angle $\approx 0.1°$ at its highest. This do not pose any significant influence on the results analysis, and we will therefore ignore it.

The data in Table 5.1 are initially presented with the minimum and maximum values of the estimates. While this gives an idea of the detection limits of the EISCAT UHF, it is not necessarily a very descriptive representation of the population. Therefore, the table also includes the median values (marked with red) of the total datasets, since this gives a measure on the properties relating to the bulk of the detections. Why we have chosen to use the median value instead of the mean value for instance, is because the mean value is much more affected by outliers than the median, which would give an inaccurate image of the true nature of the population, as the large targets gets overemphasized by the mean compared to smaller targets.

Table 5.1: Detailed data from respective BPEs. The parameter intervals are listed by their minimum and maximum recorded, or estimated, values. While red color indicate the median values.

Beam-park experiments conducted with EISCAT UHF

Name	BPE: 0118	BPE: 0419	BPE: 0619	BPE: 0421
Year	2018	2019	2019	2021
Start time	04/01 12:01:33	02/04 11:38:04	06/06 12:20:22	12/04 12:01:33
End time	05/01 11:58:52	03/04 11:59:35	07/06 12:29:00	13/04 11:59:15
Dur. [s]	86 241	87 689	86 918	86 264
P_t [MW]	1.53 – 1.72 (1.63)	1.56 – 1.77 (1.73)	1.74 – 1.92 (1.82)	1.61 – 1.78 (1.71)
T_s [K]	86.2 – 9371 (89.8)	88.7 – 102 (92.3)	75.7 – 101 (93.1)	83.3 – 105 (92.1)
N_{det}	1744	1779	1653	1657
Range [km]	177 – 2572 (879)	192 – 2616 (873)	244 – 2595 (885)	332 – 2619 (892)
Alt. [km]	171 – 2510 (853)	186 – 2552 (847)	236 – 2532 (858)	321 – 2555 (865)
$\mathrm{v}_{\mathrm{dop}}$ [km/s]	−9.1 – 9.4 (0.15)	−9.6 – 10 (−0.26)	−8.9 – 9.9 (−0.51)	−9.9 – 9.7 (−0.18)
$\mathrm{a}_{\mathrm{dop}}$ [km/s^2]	0.00 – 0.34 (0.05)	0.00 – 0.70 (0.05)	0.00 – 0.14 (0.05)	0.00 – 0.12 (0.05)
$\sqrt{\mathrm{SNR}}$ [linear]	5.0 – 10090 (15.6)	5.0 – 15060 (18.9)	5.0 – 11760 (17.2)	5.0 – 14370 (16.7)
SNR [dB]	14.0 – 80.1 (23.9)	14.0 – 83.6 (25.5)	14.0 – 81.4 (24.7)	14.0 – 83.1 (24.5)
Event dur. [s]	0.0 – 25.2 (2.2)	0.0 – 18.6 (1.6)	0.0 – 17.6 (1.6)	0.0 – 20.2 (1.8)
$d_{\mathrm{eff,min}}$ [cm]	1.32 – 380 (3.29)	1.43 – 435 (3.09)	1.39 – 439 (3.09)	1.41 – 349 (3.14)

Parameters shared by each BPE:

λ: 32.26 cm On-axis gain: 48.1 dB Azimuth: 90° Elevation: 75°

5.2 Object distribution by R, v, and i.

We have estimated the inclination numerically as a function of Doppler velocity and range. This has been done for a selection of values, and the results are shown in Figures 5.1 and 5.2. The top panels of the figures display the observed distribution for the measurements conducted in January 2018, and June 2019, respectively. Likewise, the bottom panels shows the same results for the BPEs performed in April 2019, and April 2021. Hence, the plots are presented in chronological order. For simplicity, we have in the computation assumed the objects to be in unperturbed, circular orbits. The influence of perturbations can be regarded as negligible over a time span of one day, which is the approximate duration of each BPE. More importantly, the estimates have been calculated with respect to the antenna pointing direction used in the experiments.

Since we in each campaign can observe the same object twice – both on its ascending and descending transit – each inclination serves two possible solutions. This is indicated by the colored curves appearing in Figures 5.1 and 5.2. The panels on the left side in the figures, shows the range and Doppler velocity for each detected object of the respective BPE. The detections are illustrated with black markers, and their placement with respect to the drawn curves, serves as an indication of their orbital inclination. The right panels display the related histograms in a pseudo color format – where the colorbar gives the number of targets observed in the particular bins.

For all of the campaigns, the most distinctive cluster of observations is made at a range, $R = 800 \pm 150$ km, and Doppler velocity $v_d = -0.85 \pm 0.15$ km/s – i.e. these objects appear to move towards the radar. This translates to an inclination between 95° and 102°, centered towards $i \approx 98 - 99°$. These trajectories are cases of Sun-synchronous orbit (SSO), which we covered in Section 3.6. Based on the beam-park measurements it is clear that these orbits are among the most populated regions in LEO. Thus, the results correlate well with the distribution presented in Figure 3.5.

The observations reveal numerous objects detected at respective inclinations of $i \approx 70°$, $i \approx 74°$, and, to some extent, at $i \approx 82°$. In terms of numbers, the latter exhibit the bleakest clustering of the three. Nevertheless, a significant portion is observed here in the 2018 campaign, at a range of about 1000 km, but the amount of objects within this region appears to have declined in the three following experiments. On the other hand, the relative portion of detections made at 70°, and 74°, are similar in all four BPEs. For the first case the targets are mostly detected at a range of about 900 km, translating to a Doppler velocity of $v_d \approx 1.6 \pm 0.1$ km/s. Whilst for the second case (orange line in plots) we got two instances of pronounced clustering; the first at about 800 km range, and the other occurring at ranges of ≈ 1550 km, which translates to

Doppler velocities somewhere within the 1.3–1.0 km/s interval. Indeed, this distributional behaviour of the observations, matches with that appearing in Figure 3.5, with the peaks found in the same regions.

Furthermore, we recall from Section 3.4 that the spacecrafts involved in the two most severe breakup events on record, were all located in polar orbits. Fengyun-1C had an inclination, i, of 98.6°. Likewise, $i \approx 86.4°$ for Iridium-33, while for Cosmos-2251, $i \approx 74.0°$, was the orbit inclination. The debris created in these events have diffused across the orbital environment, and are now in trajectories encircling the globe. However, if we only regard the inclination of the parent bodies for now. It becomes tangible that these debris clouds contribute to several of the "observation cluster" appearing in the plots. Especially the Fengyun and Cosmos fragments. At their associated inclinations, the pronounce population occur at ranges 700 – 900 km. This is in good agreement with the altitudes these disintegrated at, in 2007 and 2009, respectively.

Though Figures 5.1 and 5.2 exhibit the same general pattern, there is a unique signature occurring in the April measurements from 2019. It can be distinguished as the points arising below 500 km range, at a Doppler velocity of ≈ -0.6 km/s. Further, these make up the starting portion of a diagonal structure that distributes itself in the way that growing range also increase the Doppler velocity. This diagonal pattern seems to extend all from −0.6 km/s to about 0.5 km/s along the y-axis, and from 200 to around 900 km along the x-axis. Presumably, these objects are debris from the Indian ASAT-mission.

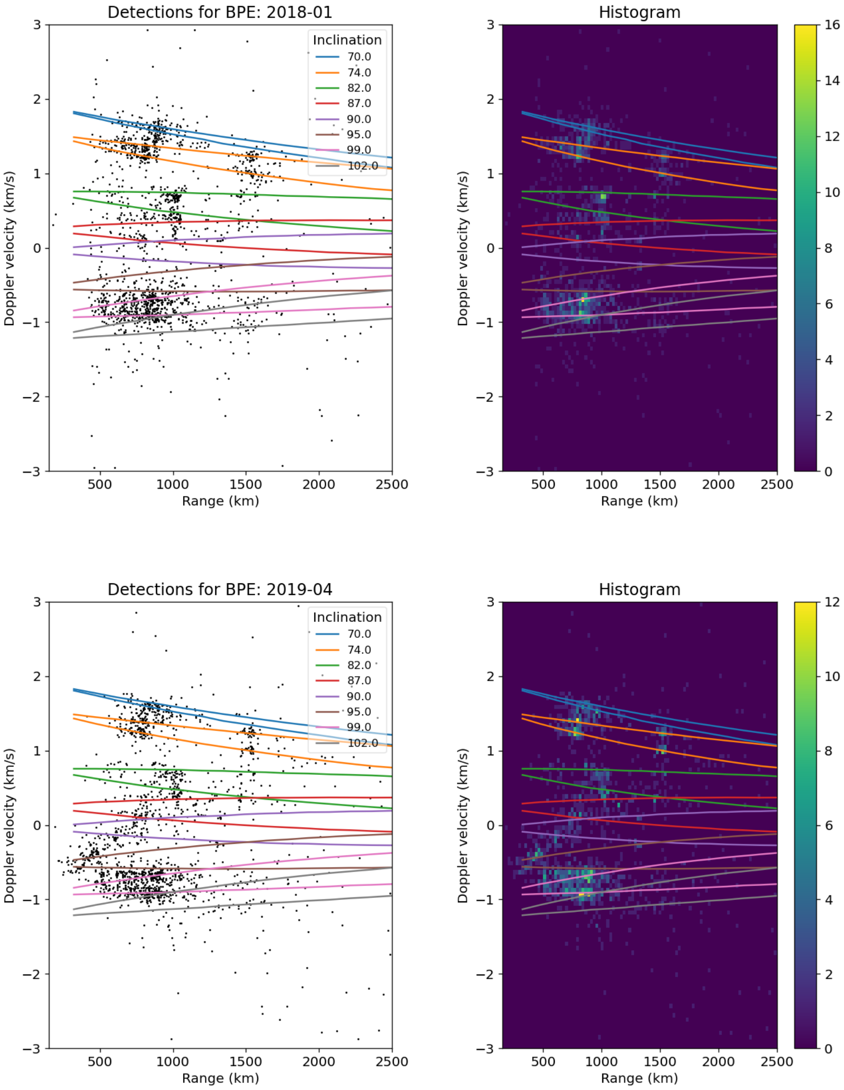

Figure 5.1: Distribution of beam park observations as a function of range, Doppler velocity, and inclination. The range and velocity are measured quantities, while the inclinations are estimated numerically. The top, and lower panels show object observations made in January 2018, and April 2019, respectively.

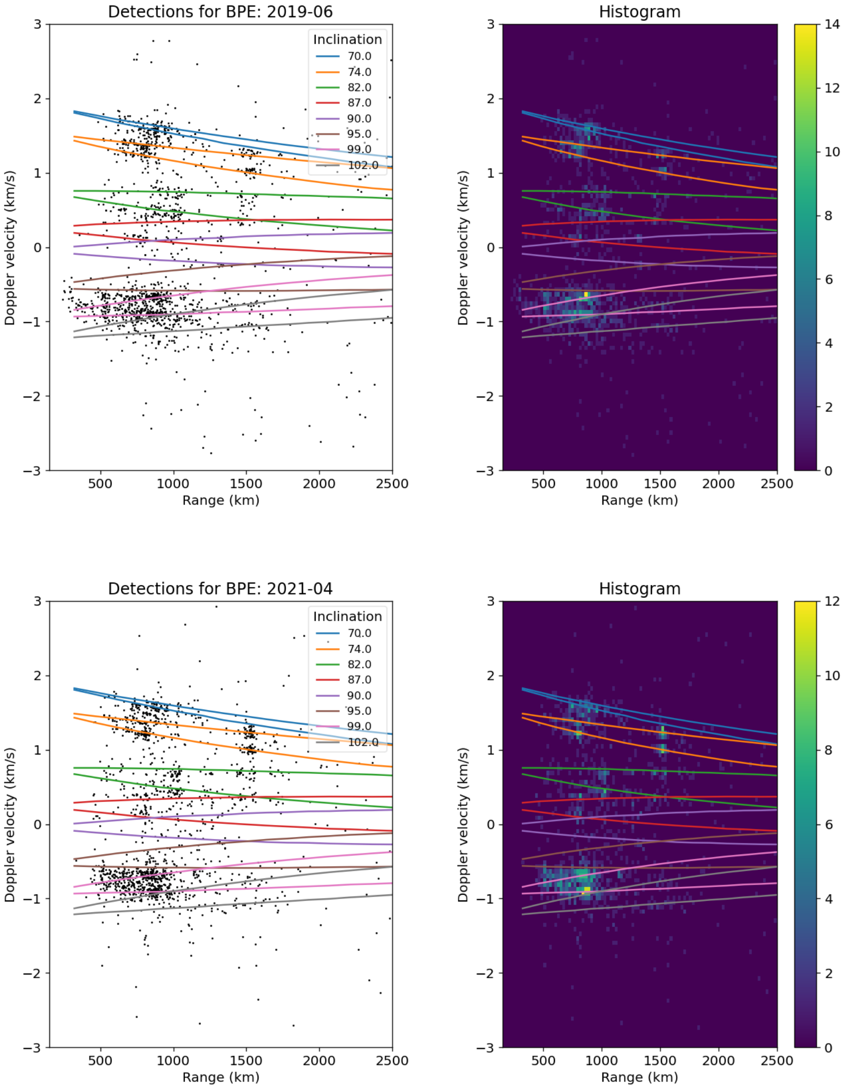

Figure 5.2: Distribution of beam park observations as a function of range, Doppler velocity, and inclination. The range and velocity are measured quantities, while the inclinations are estimated numerically. The top, and lower panels show target detections captured in June 2019, and April 2021, respectively.

6

Catalog correlation

In the figures presented later, the objects have been divided into two categories, designated as *catalog matches*, and *uncorrelated detections* – marked in red and black color, respectively. The catalog matches are named such since the observed object can be related to an item contained in the SpaceTrack-catalog [Uni21]. In which case, the positional properties of the detected target, and the object found in the catalog, resemble one another in such a manner that they are determined to be the same object. These belong to the 'familiar' part of the space population, and are routinely tracked by the SSN. Consequently, the orbits and origin of these are known. Whilst the second category governs the detected targets of which we have not managed to associate with any of the entries in the catalog, thus, their nature and origin remain more or less unknown.

6.1 Method

In order to arrive at the distinction, we have used the correlator included in the magnificent SORTS program [1] – which is described in [KVK+19]. It should therefore be acknowledged that much of the contents of this chapter are based on some of the features this program offers.

[1] Location of SORTS-repository: `https://github.com/danielk333/SORTS`

Before moving on to the detailed step-wise description, it might be pertinent to take a look at Figure 6.1, which provides an overview of the correlation process.

The correlator takes in the detections from the respective BPE, along with a snapshot of the Spacetrack-catalog captured in the same time span (as the BPE) and given in the TLE-format.[2] Since the catalog data are provided as snapshots (i.e. the situation at a particular instant of time), SORTS has implemented a SGP4-propagator[3] which propagates the catalog objects for a time extent matching that of the BPE. In addition to this, we specify what radar facility that has been used to make the detections, with the appropriate pointing direction defined. This then tells the correlator what spatial regions it should search for matches in. Once this has been specified, and ensuring we are computing in a ECEF[4] reference frame, the correlator searches through every item in the catalog for a particular detection, and then returns the n closest matches it found in the catalog, for the object that was detected at a time t. So it does for every object detected in the respective beam-park experiment.

---

[2] The reason it is called "two-line element" is because the information about each object in the catalog is organized across two lines. The contents of the first line include, among else, entry catalog number, international designator, element set epoch, drag term, etc. At the second line the mean, doubly averaged Kepler states are provided, in addition to other info [Uni21, Kli10].

[3] The Simplified General Perturbations (SGP-4) theory performs a propagation with doubly averaged Kepler elements with respect to secular variations in the zonal harmonics in the Earth potential, as well as perturbations from drag [Kli10, p.216].

[4] *Earth-centered Earth-Fixed*. The conversion of the catalog population is important, as tle data are captured in a *True Earth, Mean Equinox* frame.

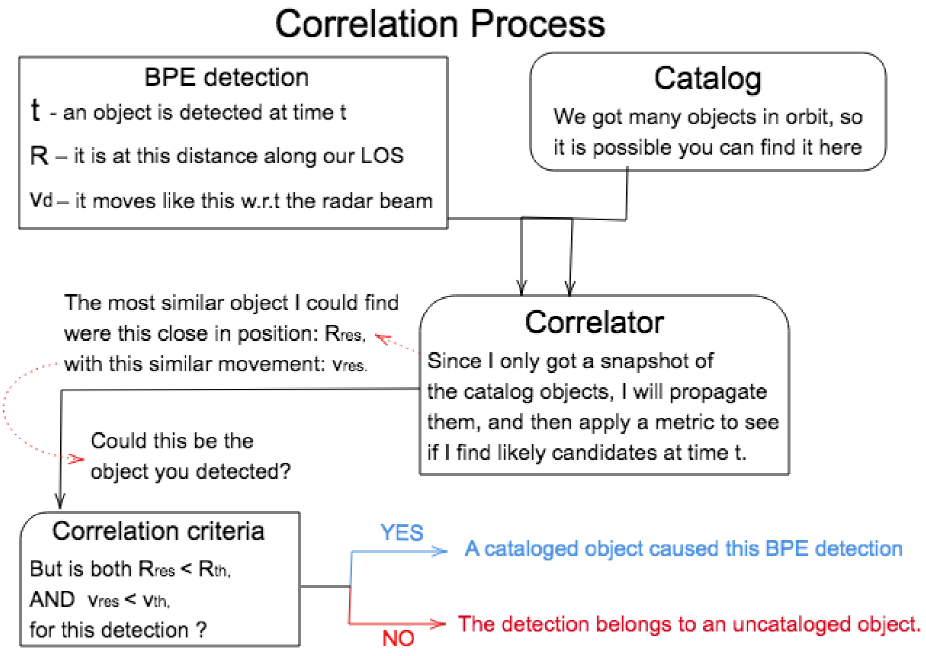

Figure 6.1: A simplified schematic on how to identify catalog objects from measurements.

In the computations, we have set $n = 1$, which means that the correlator only returns the closest match for each detection. The closest catalog match is found using a specified distance measure (metric), D_m, arranged such that lower returned values indicate "better" matches, i.e. Closest Match = $\min\{D_m\}$. The distance measure used in the computations, can be expressed as

$$D_m = \sqrt{\left(R_{cat} - R_{bpe}\right)^2 + w^2\left(V_{cat} - V_{bpe}\right)^2}, \qquad (6.1)$$

where R_{bpe}, and V_{bpe}, indicate the measured range and Doppler velocity of the detected object, while R_{cat}, and V_{cat}, denote the range and Doppler velocity of the cataloged objects entering the simulation. It might be more intuitive to think about the Doppler velocities as radial velocities here, but we will stick with the first term for consistency. The last term that appears in Eq. 6.1, is a weighting factor, w. It is of significant importance, as it ensures that the Doppler velocity residuals, $\Delta V = V_{cat} - V_{bpe}$, contribute equally to the distance measure (and ultimately to the correlation) as the difference in range, ΔR. The weight needs to be included since the difference in range is typically several orders of magnitude larger than the difference in Doppler velocity. For instance, a range residual of 1 km is, unweighted, playing a larger contribution than a Doppler velocity difference of e.g. 0.5 km/s. Still, a range difference of 1 km is relatively small when we are talking about objects distanced over 500 km away. However, a relative difference of 0.5 km/s, i.e. 1800 km/h, is a massive difference when we are considering velocities. Therefore, to account for this effect, we have used a weight, $w = 10$, in the calculations. This way, a velocity residual of 0.1 km/s accounts for an equal contribution to the distance measure as a range residual of 1 km (since the terms are squared in Eq. 6.1).

After we have successfully found the closest match for each detection, we need to determine if this match indeed translates to a correlation with the catalog or not. For this, we need to apply a correlation criteria, which says that the range residual ΔR needs to be within a threshold value R_{th}. However, also an uncatalogued object might coincidentally find itself close to the position of a detection – simultaneously as an object found in the catalog for instance. Less likely is it though, that it does this in addition to move in a similar manner/direction as a catalogued object. Therefore, as a means to correlate the correct objects, we put a constraint on the movement of the object as well, saying that the Doppler velocity residual ΔV needs to be within a threshold value v_{th}. Then, if every criteria is satisfied, we classify the respective detection as a catalog object. However, if at least one criterion is left unsatisfied, we categorize it as an uncorrelated object, as pointed out in the beginning of this chapter.

If our correlator has done a decent job, a significant fraction of the population should have residual values which are centered around zero. Since, when both residuals, ΔR and ΔV, are equal to zero, it simply means that the correlator found an object in the catalog that was at the exact same range distance, having identical radial velocity (relative to EISCAT UHF), at the same time as the detection was captured. However, one should expect some uncertainty occurring in both the measurements and the simulations, which is something we need to account for when choosing the correlation criteria.

6.2 Choice of correlation criteria

The question then remains, what is a suitable correlation criterion? To determine the threshold values we have done a graphical inspection. That is, we have evaluated the residual histograms for both range and Doppler velocity, in order to identify where the bulk of the population resides. This method is inspired by the similar approach used in [VKM⁺19]. The histograms give us an idea of what threshold values, R_{th} and v_{th}, are reasonable for us to ensure a good degree of correct correlation with the catalog. Ultimately we have deemed the detected object to be a match with the catalog if

$$|\Delta R| < 2.0 \text{ km} \quad \text{AND} \quad |\Delta V| < 0.2 \text{ km/s}. \tag{6.2}$$

The residual histograms within this *correlation interval* are included in the top panels of Figures 6.2 to 6.5, with each figure representing the situation for a particular BPE. Blue colored bins illustrate the range residuals, while the Doppler velocity residuals are displayed with red bins. The binwidths are set to 50 m, and 5 m/s, respectively. Indeed, the histograms are all centered close to zero (with a slight negative shift), with something that resembles a normal distribution. The histograms suggest that we could easily have chosen thresholds having half the value of the ones determined in Eq. 6.2, without 'loosing' too many matches. However, with respect to our objective, we proclaim it more beneficial to correlate 'too many' objects with the catalog, rather than wrongly classifying actual cataloged objects as *uncorrelated detections*. In any case, it is reasonable to assume that the majority of the unknown objects would have (at least) one residual value greatly exceeding our chosen thresholds, and therefore enter the category they truly belong in, regardless of the choice of threshold (given that it is reasonably low).

To support our choice of threshold, we have plotted the detections (as points) in residual space, with ΔR along the x-axis, and ΔV along the y-axis. The respective figures are shown in the bottom panels of Figures 6.2 to 6.5. To give the best representation, we have used logarithmic scale for both axes in the figures. Moreover, to prevent elongated plots, and to highlight that both (range and velocity) residuals yield an equal contribution to the correlation, we have multiplied the y-axis values (ΔV) with a factor of w. This weighting factor is the same as mentioned before, which, analytically, can be found from

$$\begin{aligned} w &= \frac{R_{th}}{v_{th}} \\ \Rightarrow w &= 10, \end{aligned}$$

which is calculated by inserting the threshold values from Eq. 6.2.

When investigating the scatter plots of Figures 6.2 to 6.5, the presence of two distinct clusters emerges. The first cluster, indicated by red dots, has an overall population which is situated at pretty low residual values – close to zero on both axes. The other cluster, represented by black dots, is situated at comparatively high values – mainly between 10 and 100. Remember that each of the points represents the difference between a detected object and its closest (simulated) catalog companion. Thus, we can proceed to say that the first cluster must represent detections of cataloged objects, since the detected and simulated characteristics of the objects are so similar that they need to be the same object. Whilst for the inhabitants of the other cluster, the following logic applies: The closest catalog match, and the detected object, have too dissimilar properties in order for them to represent the same object – and therefore these detections have to be caused by an object found outside the spacetrack-catalog.

The border separating the two classes, given by our correlation threshold, is represented by a blue line in the plots. Some detections are, however, located at border-line residual values. This is particularly visible in Figure 6.4. These detections may belong to either category, so we might have some degree of false classification in this region, as compared to the true nature of the object. On the other hand, the objects enclosed by the purple boundary – called "optional threshold" – are, with a greater degree of certainty, associated with cataloged objects. Thus, if the main objective was to ensure highest ratio of 'correctness' for true catalog matches, the optional threshold might be a more desirable choice. However, as this only governs a minor fraction of the total population anyway – which can be seen by the relatively low population of points residing between the blue and purple lines in the bottom panels – either choice of threshold would render most of the data correctly classified. It is therefore not of significant importance if we happen to get some misclassifications. To summarize, we claim it more probable that the points enclosed by the blue boundary are related to detections of catalog objects, rather than to detections of unknown objects, and vice versa.

As a final remark on the choice of threshold we mention that we easily could have picked a lower threshold with respect to some of the campaigns, and thereby obtained more *confident* correlations. However, as a matter of consistency, use the same criteria for every experiment.

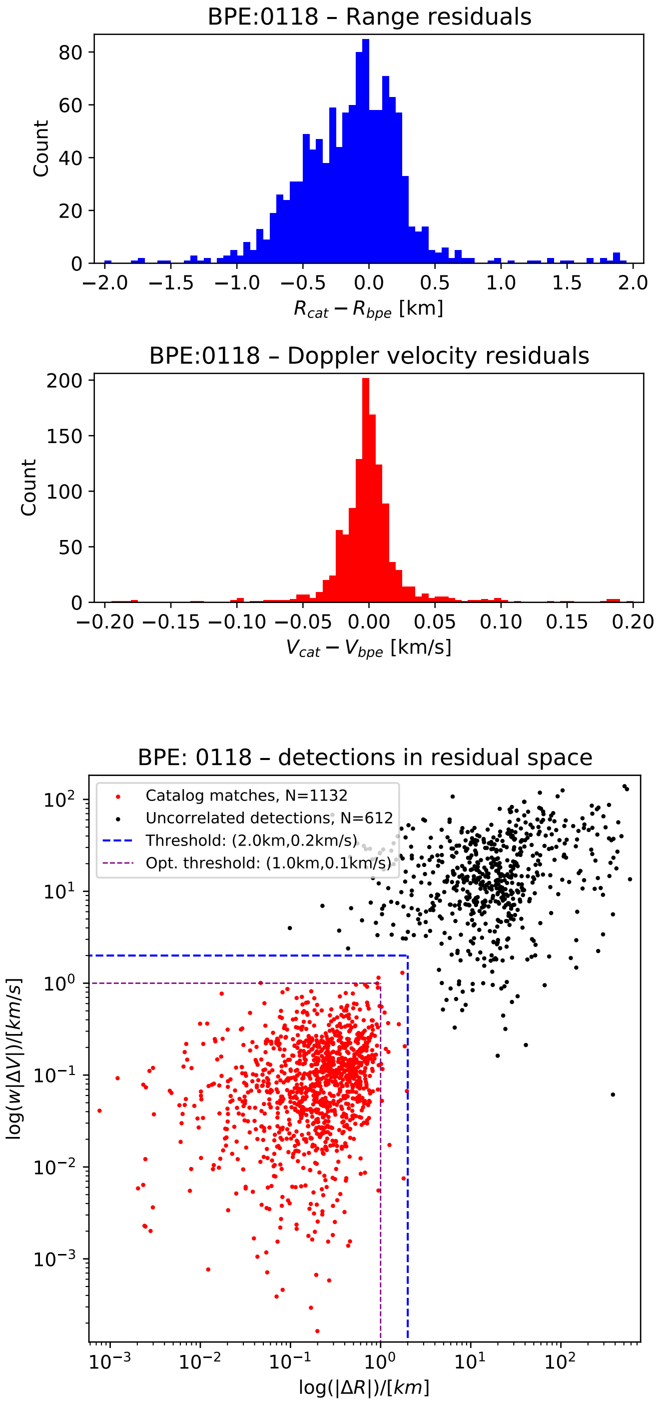

Figure 6.2: Correlation figure for BPE: 0118. The top panels show the residual histograms for the cataloged objects. The histograms can then be related to the red points of the bottom panel, which displays the appearance of every detection in residual space. The points contained by the blue correlation boundary represent detections associated with cataloged objects in orbit. This category, named *catalog matches*, has the highest occurrence in this particular campaign, compared to the three other experiments. The remaining points are categorized as *uncorrelated detections*, since their residuals exceed the correlation threshold(s).

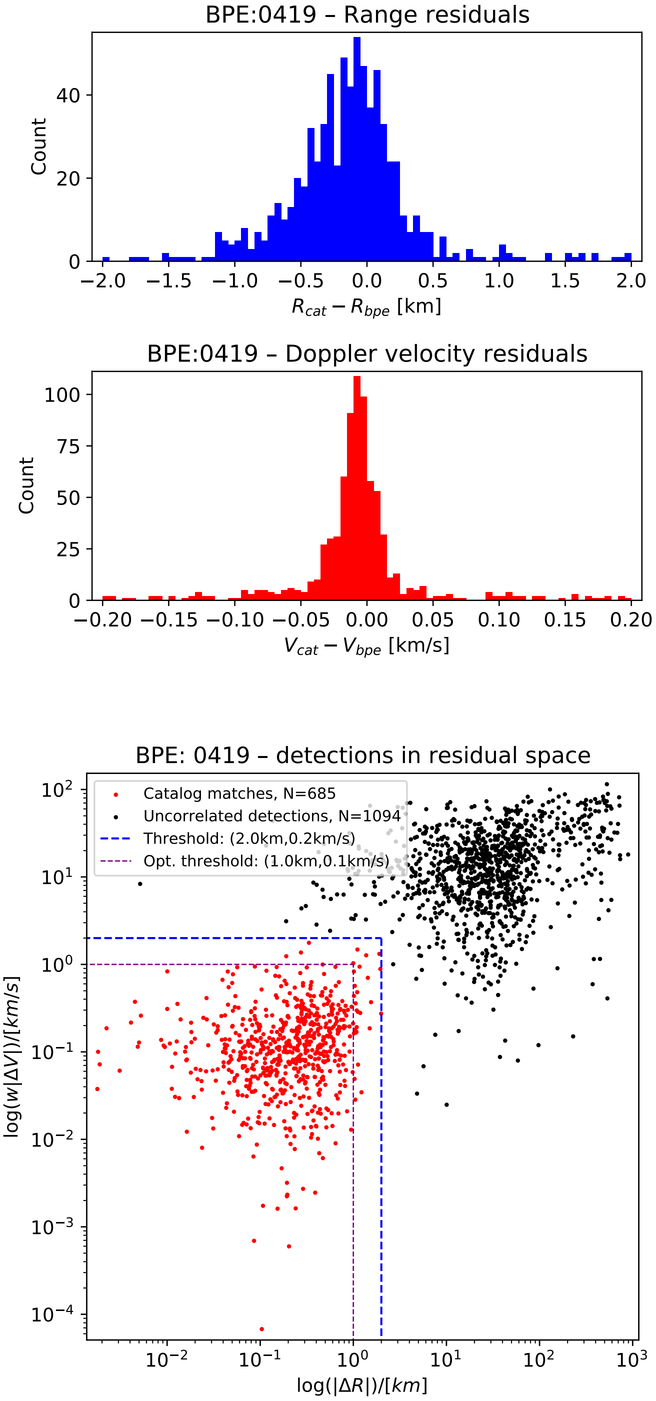

Figure 6.3: Correlation figure for BPE: 0419. The top panels show the residual histograms for the objects correlated with the catalog. The bottom panel displays all of the detections in residual space. Out of the four conducted experiments, the presence of uncorrelated detections is maximized in this one.

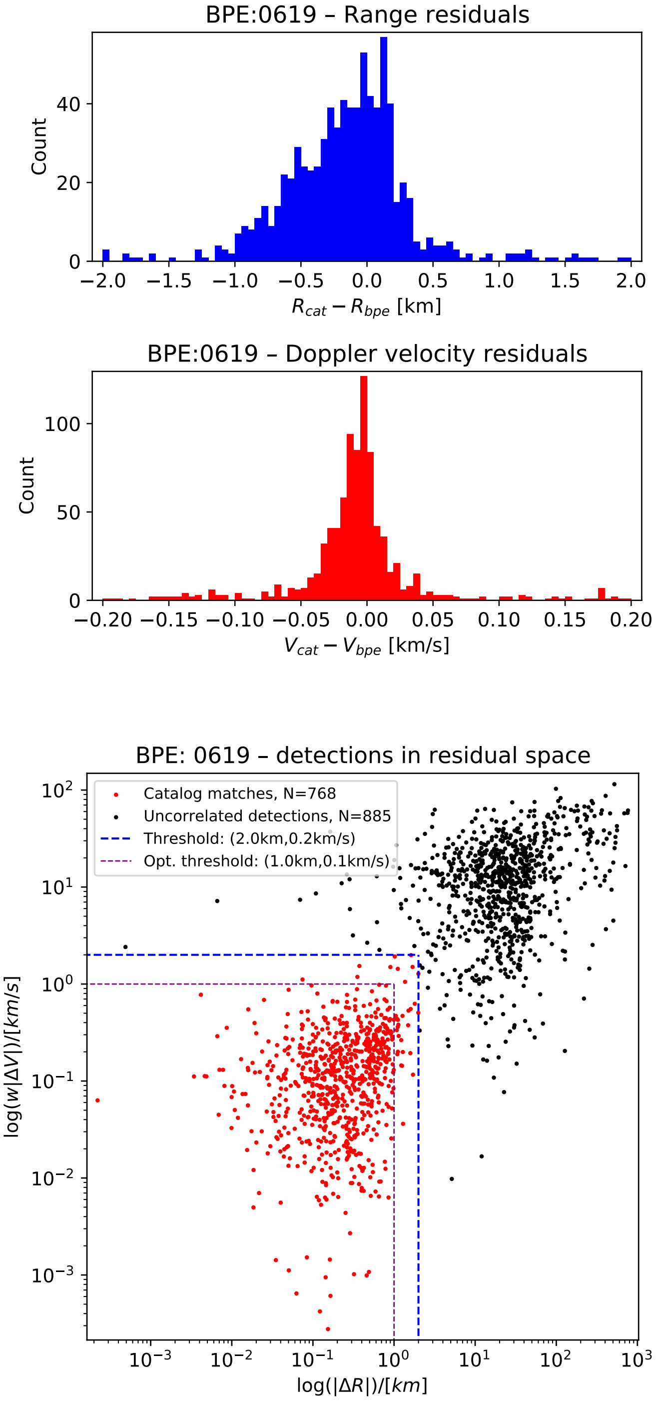

Figure 6.4: Correlation figure for BPE: 0619. The top panels show the residual histograms for the objects correlated with the catalog. The bottom panel displays all of the detections in residual space. The occurrence of points near/on the correlation boundary is perhaps most prominent for this experiment, which may open up for some misclassifications. However, this issue might apply to some 10–15 objects, which still constitutes less than 1% of the overall population. Hence, it is evident that most detections would be classified correctly, as long as the criteria are chosen within some appropriate selection interval.

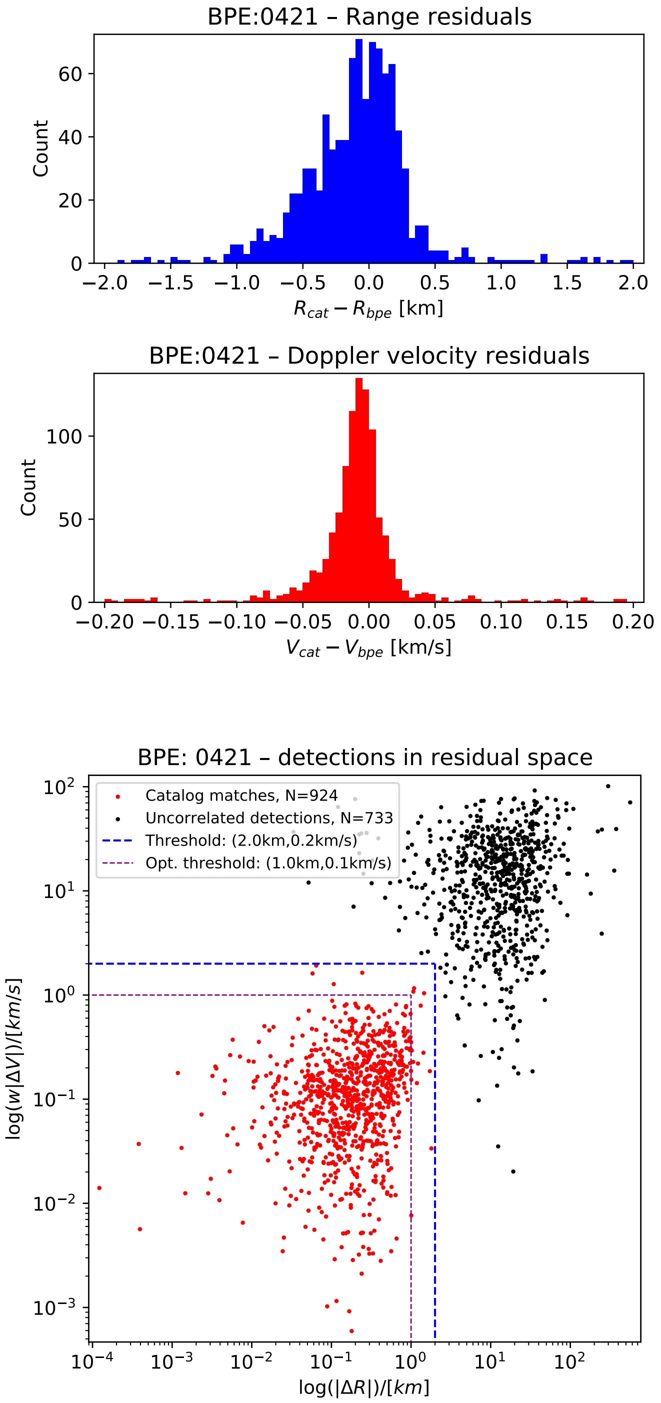

Figure 6.5: Correlation figure for BPE: 0421. The top panels shows the residual histograms for the objects correlated with the catalog. The bottom panel displays all of the detections in residual space. Comparing this to the three previous experiments, it seems that the situation are slowly changing towards how it looked like in 2018, in the sense that *catalog matches* are once again the most numerous of the two categories.

Results of correlation

The outcome of the correlation is summarized in Table 6.1. It is a considerable variation in the fraction of cataloged and uncorrelated objects between the different campaigns. In particular from the observations made in 2018, to those conducted in 2019. Evidently, this is a quite surprising result, as we do not expect that the population of cataloged objects had decreased this drastically. For instance, it is not likely that ≈ 450 objects all of a sudden changed *category* going from January 2018 to April 2019. Therefore, there needs to be another explanation. Exactly what the cause is, is not easy to say for sure.

However, one guess is that the occurrence of reasonably sized objects at lower ranges was higher in 2019, than in the 2018-measurements. Since the signal power reduces proportional to R^{-4}, as seen in Eq. 4.4, smaller objects at lower ranges may still yield a higher SNR than larger (cataloged) objects at higher ranges. In turn, the lower located object may get favored in the measurement analysis compared to the cataloged object situated at higher altitudes – given that the two objects pass through the radar beam at similar times. As a consequence, the measurement of the cataloged object might get 'accidentally' discarded during the analysis. Note that this is only one interpretation, and its validity needs to be addressed before making any conclusion. In any case, further investigation would need to be performed in order to verify the reason for the correlation deviations between the different experiments.

Table 6.1: Numbers of cataloged and uncorrelated objects from four beam-park experiments, including approximate percentage of the overall detected population.

BPE	01/18	04/19	06/19	04/21
Cataloged	1132 (65%)	685 (39%)	768 (46%)	924 (56%)
Uncorrelated	612 (35%)	1094 (61%)	885 (54%)	733 (44%)

7

Inspection of Microsat-R fragments

It is time to proceed with our initial quest of investigating the space debris generated in the Indian ASAT-test (described in Subsection 3.4.3). This is done by evaluating the results from the four BPEs. The mentioned debris cloud will from henceforth be referred to as the *Microsat (or MSAT) fragments*, named such because the victim of the collision was the Microsat-R satellite.

The satellite destruction occurred on 27/03/2019 – meaning that three of the BPEs have been conducted in the aftermath of this event. The measurements are captured with distinct differences in time, and one can therefore assume that the footprints of the MSAT fragments will have a remarkable variation in its appearance – caused by the dynamic orbits of the debris. Specifically, the elapsed time for when the experiments were conducted – with respect to the ASAT-event – yield; 1 week (6–7 days) for *BPE 0419*; 71 days (2.3 months) for *BPE 0619*; and 747 days ($\sim$ 2 years and 2 weeks) for *BPE 0421*. This gives us a fairly good representation of the short-term and long-term evolution of the mentioned debris cloud, with the last providing us with information of the current situation – and possibly new information on more recent fragmentation events.

In addition to the three mentioned BPEs, we also got results from a BPE conducted in January 2018 (which we call *BPE 0118*). This lets us compare our results with how the situation appeared at a time prior to the event (i.e. $\sim$ 1.25 years prior). For this particular BPE it was, in addition to EISCAT UHF Tromsø, conducted similar measurements with one of the UHF radars located in Svalbard. However, since the other three BPEs only used the Tromsø site, we will not include the Svalbard results in our analysis.

Notes about results: As may be apparent from Table 5.1, we got access to a vast amount of data. Unfortunately, not all will be presented, since it would simply be an overload of information that might overshadow the pursuit of our objective. Thus, the results that will be presented are those considered to be of greatest relevance. The results, portrayed in different formats, are presented in chronological order, as this opens up for the best level of comparison. Since we are treating four experiments in parallel it is easy to mix things up. Thus, to clearly state which measurements we are referring to, the sub-chapters are headlined with the date of the experiment – expressed in a month/year-format.

Note that the figures appearing first are structured in another way than the next formats. These are maximized in order to give a clear visualization of the distinct differences in the distribution. When this is readily invoked, we present the other figures in a more compact way, which suits a better solution when comparing the data, since it is more convenient to view them on the same page.

As we thoroughly outlined in Chapter 6, we have divided objects into two categories. This distinction is maintained in most of the results that are presented in the following. With that said, our main focus will be on the *uncorrelated detections*, since we can expect that the Microsat fragments would have taken some time to enter the Spacetrack-catalog. Moreover, many of these fragments would not have entered the catalog at all, since they are too small in size, i.e. below 10 cm, to be monitored by the SSN-facilities. However, since EISCAT UHF has the ability to detect targets of this size regime,[1] we should expect some of these to enter the measurements – in which case they will make their presence as members of the category called *uncorrelated detections*.

In the following, the terms *red points*, and *black points*, will be introduced. The distinction can be traced back to the two colors used to separate the categories appearing in the figures. Using these terms do not only make room for smoother textual flow – it also helps the reader to separate the categories.

---

[1] As listed in Table 5.1, it is possible for the radar to detect targets as small as ≈ 1.3 cm – if it traverses the main lobe. However, most objects get detected in the side lobes of the radar beam, due to the larger collection area. Therefore, the true size of the smallest observed object is probably larger than 1.3 cm. Nevertheless, it is sensible that the lower bound still is well below 10 cm.

Thus, whenever you encounter the word "red", we are talking about detected objects which we have successfully identified from the catalog. Likewise, whenever the word "black" appear, we are discussing detected objects that cannot be found in the catalog – hence the unknown/uncorrelated objects.

7.1 Range vs Time

Figures 7.1 and 7.2 describe where, and when, every detection is made, for each of the four measurement campaigns. In other words, the plots show at what distance from the radar – i.e. range – a detection made at a particular time, was located. The range, in km, is displayed along the y-axes of the figures, while the x-axes show the time of detection, given as the amount of hours since the epoch of the respective campaign.

01/18

For BPE:0118 we got a "healthy" mixture of cataloged and uncorrelated objects, in the sense that there are few black clusters in the plot. Some are still visible though, among those we can mention a successive 'train' of objects appearing at around 480 km and 1300 km range, at about 22–23 hours after epoch. With further investigation of these clusters, obtaining relations to distinct breakup events should be feasible.

04/19

We have a notable scene change in April 2019. Overall, the appearance of black objects are far more abundant than before, indicating that a lot of space debris has accumulated by this stage. It goes without saying, that certain observation periods in the panels of Figure 7.1 show a remarkable discrepancy compared to the other. A distinct distribution signature occurs at two occasions in the April 2019 measurements, when the object density suddenly increases.

The first of these clusters are seen to be most pronounced between 11 and 12 hours after epoch. This cluster is seen extending all the way from $\approx$ 250 km up to $\approx$ 1500 km in range, with the greatest fraction of the cluster appearing at the lower portion, i.e. below 600 km. However, the significance of black points appearing adjacent to the densest group – especially at ranges of 700–900 km – suggests that many of the uncorrelated detections within the time window of 9–14 hours after epoch, also can be linked to the same cluster. In terms of time of day, this translates to 20:30 UTC (02/04) to 01:30 UTC (03/04), with the main group passing the beam at 22:30–23:30 UTC (02/04).

A similar cluster appears at 21–22 hours after epoch, i.e at 09:30–10:30 UTC (03/04). Although the presence of this cluster is not equally significant as the former at the highest ranges (from 1000 to 1500 km), a comparatively larger amount of black objects at the intermediate ranges from around 700 to 900 km is found within the main group. The population is still substantial below 500 km in range, extending all the way down to about 200 km. Since we got a lot of uncorrelated detections neighbouring the cluster, mainly at ranges of 700 – 1000 km, it is probable that associated fragments are found passing the beam between 07:30 and 10:30 UTC on thethird of April. Namely, from 19 to 23 hours after measurement epoch.

The clusters are representing two beam passing events – the ascending and descending transit – of the same debris cloud.[2] Specifically, the debris cloud are believed to be the Microsat fragments. Although it is difficult to know this for certain, there are several evidence which points towards this being the case.

First of all, the destruction of Microsat-R occurred merely one week prior to the date of the respective observations. No other breakup have been reported taking place in LEO in the meantime. Apart from the ASAT-test, the other closest fragmentation event, with respect to date, occurred on 6 February 2019 as found in [Nat19b]. The particular event was the fragmentation of a Japanese rocket body, *H-2A* second stage, located in a orbit with height 590 × 493 km and inclination of 98.8° at the time. Indeed, these characteristics suggest that this event may have entered the EISCAT-observations. However, it is not likely that the fragments of a rocket body breakup distribute itself in the fashion of our clustered data.

Second of all, the main groups of objects still have a compact distribution – shaped somewhat like a cylinder in Figure 7.1(bottom panel). This tells us that the particular debris have not diffused for a particularly long time, as the bulk of the population passes the radar beam during 0.5 – 1 hour. Longer exposure to perturbations should slowly separate this compact cluster apart.

Perhaps the most solid argument for this being the Microsat fragments is given by the low ranges at which the clusters are detected. In Subsection 3.4.3 we said that the altitude of the parent object was (294×265) km. It is not common that spacecrafts are located at such low altitudes,[3] since the dense atmosphere

---

[2] How the ascending and descending pass relate to the distinct cluster observations, is something we need to revisit later.

[3] As can be confirmed by Figure 3.5.

reduces the mission lifetime. Hence, we are left with a very limited selection of candidates which fits our case. This brings us to the conclusion that the observed clusters – appearing in bottom panel of Figure 7.1 – are caused by the Microsat fragments.

The large range extent in the results indicates that a lot of the debris took on more eccentric orbits after the collision. Moreover, there is a distinct internal range difference between the first and second pass of the debris cloud, most visible at the highest ranges. This means that the LOS distance between the radar and some of the objects, depends on where along its orbit the target is located. This is an additional argument telling us that several of the orbits are eccentric. Most of these trajectories may govern the fragments of the missile weapon, but this is hard to determine without accurate modelling of the explosion. Knowledge about the missile trajectory would prove an advantage, if not a necessity, for the implementation of this model. Unfortunately, such information is rarely released to the public.

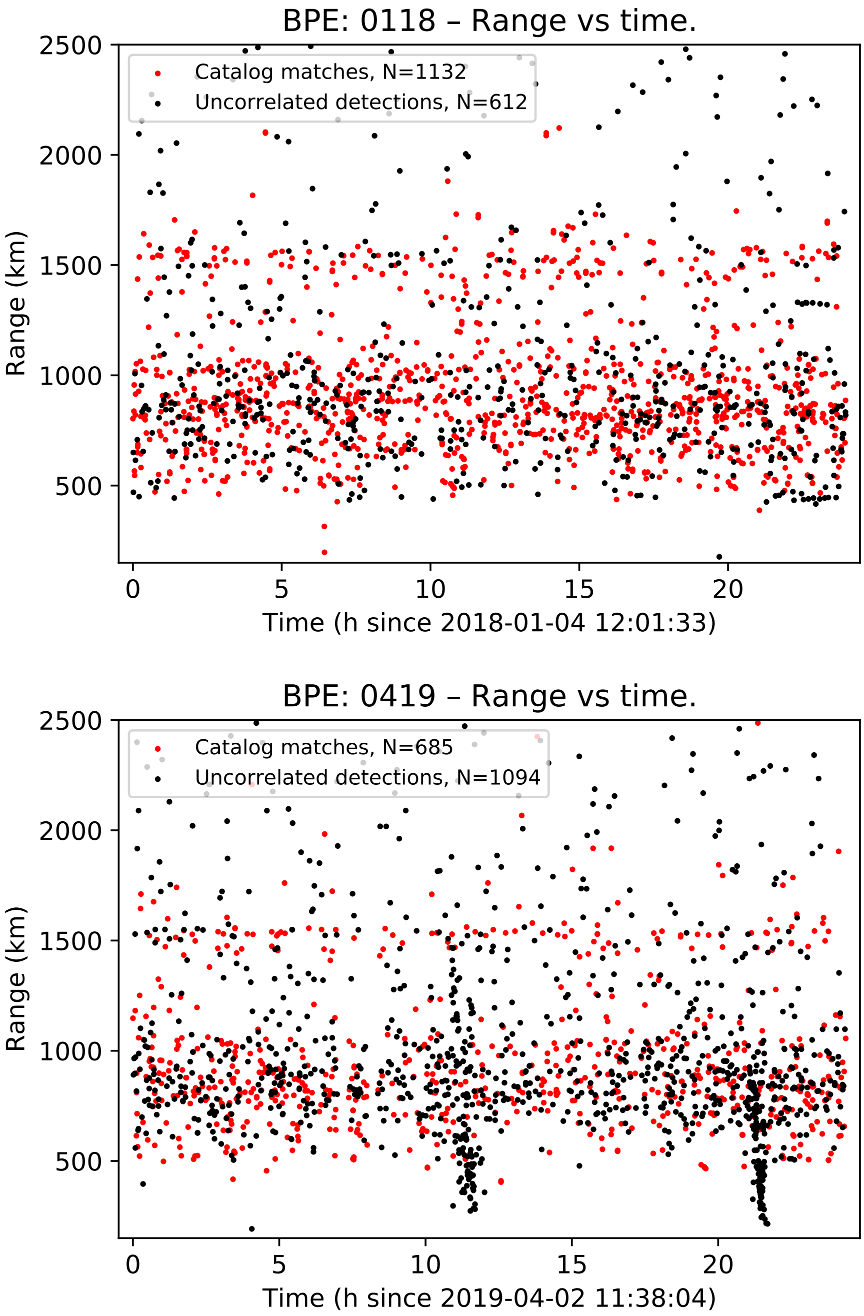

Figure 7.1: Range as a function of time. The top panel is associated with the BPE conducted in January 2018, while the bottom belong to that conducted in April 2019. In the latter, two remarkable events stand out from the rest. These can be recognized by the pronounce clustering of uncorrelated detections centered at ≈ 11.5, and ≈ 21.5 hours after epoch.

06/19

How the observations are distributed in June 2019, can be seen in the top panel of Figure 7.2. The Microsat fragments are still clearly visible. Two distinct groups of uncataloged objects can be recognized centered at ≈ 9.5, and ≈ 19.5 hours after epoch. Thus, the period between these passes get detected, adds up to 10 hours – the same as two months prior. However, the pronounced clusters that appeared within the April measurements are not equally compact in June.

The change is perhaps most visible at ranges below 500 km. At these heights, the time variation for when the fragments were observed, were less than an hour in April, i.e. the time that elapsed from when the first object in the compact cluster was detected, to the final. In June, this time interval seems to have extended to 3–4 hours. This implies that the debris had diffused along its orbit during the two month time span due to perturbations.

In addition, the range extent is not as pronounced as before. This is evident from the bleaker distribution of black objects detected between 1000 and 1500 km range, at the particular times of interest. The reason is that the elliptic orbits gets circularized with time, as a means of decreasing eccentricity. This is a consequence of the considerable drag an object encounters at the low residing perigee position – where the density of the atmosphere is at its greatest in its trajectory. The high *perigee drag* acts like an impulsive braking maneuver on the fragment – lowering its apogee for every transit, until its orbit is near-circular. Only when the desired shape is obtained, may the perturbations force the object to de-orbit [Kli10, p.75]. The fragments that avoid this process – because they are located in near-circular orbits subsequent to the collision – are those first removed from orbit, given that their initial altitude is sufficiently low.

It is evident that many Microsat fragments have been removed from orbit during the two months. Since the cluster populations are less numerous in the June plot than they were in April. By using the recorded decay data of the Spacetrack-catalog [Uni21], we find that 53 objects[4] of this debris cloud are reported to have de-orbited in the period between the two 2019 campaigns. Although cataloging was particular difficult for this event, due to the challenges mentioned in Subsection 3.4.3, it supports the development observed in the BPEs.

---

[4] 26 in April, 26 in May, and 1 during the first week of June.

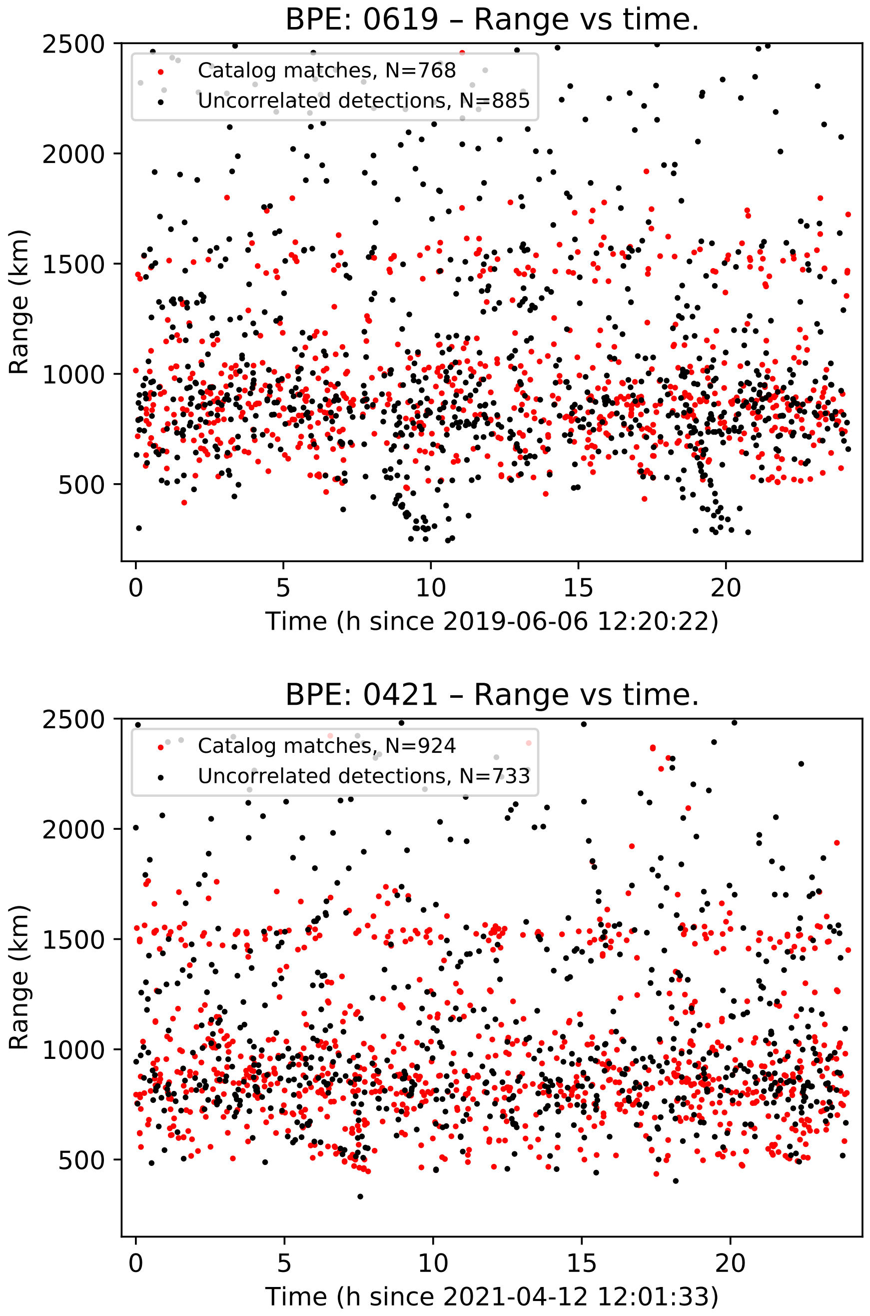

Figure 7.2: Range as a function of time. The top panel relates to the BPE conducted in June 2019, while the lower panel displays the similar format for the BPE conducted in April 2021. For the former, two distinct clusters are discovered centered at ≈ 10, and ≈ 20 hours following the epoch. In particular, the two clusters dominate the presence of objects found below 500 km range. Only a few observations are captured at these ranges in the 2021 campaign.

04/21

The range vs time diagram for the measurements conducted in mid-April this year (2021), are shown in the bottom panel of Figure 7.2. The distinct features of the clusters appearing in the 2019 results, are not discovered in 2021. This suggests that most of the Microsat fragments have decayed by now. Indeed, this result serves in agreement with the relatively low altitude where the Indian ASAT test took place. The atmosphere is simply too dense at these heights to allow an orbital lifetime exceeding two years. Unless an object get external contributions of energy, such as thrust, it de-orbits in a rather short time. It goes without saying that space debris does not obtain thrust, hence will they dissolve quite quickly.

Some Microsat fragments may still be present at higher altitudes. Out of the debris that were cataloged [Uni21], it is still one Microsat-R fragment left in orbit at the time being – with apogee of 1228 km, and perigee of 275 km. Potentially, several fragments accompanies it, although their characteristics have prevented them from being officially associated with the event. A peculiar alignment of uncorrelated detections take place at $\approx$ 7.5 h after epoch, extending from $\approx$ 1000 km range for the highest object all the way down to $\approx$ 250 km for a lowest "lonely" target, with visible range gaps occurring in the particular distribution. A similar "line of detections" is made around 17.5 hours after epoch, with a lower object at $R \approx 400$ km trailing them by half an hour. All of these objects may be totally independent of one another, and we do not have any basis for suggesting these to be the Microsat fragments at the moment. We would need more evidence to justify such before making any conclusion. LEO is indeed the home of countless other objects, thus the probability of these "coincidentally" being the Microsat fragments is tiny. Nevertheless, we regard it as an area of interest for the moment.

Without limiting our focus to this event alone, this year's observations show some distinct clusters of uncorrelated objects, that may be related to more recent breakup events. Some of the most pronounced include those found at 3.5, 9, 14, 16, and at 21–22.5 hours after epoch. All of these should be regarded as approximate numbers. All of these clusters have been observed at ranges of 800 ± 50 km.

According to [Nat21], the two first breakup events of 2021 occurred on 10 March, and 18 March, respectively. The first fragmentation was associated with the U.S meteorological satellite NOAA 17, which resided in an orbit of 817 × 800 km altitude, at an inclination of 98.62°, when the event occurred. Eight days later YunHai 1-02 – a Chinese meteorological satellite – fragmented while occupying an orbit of 785 × 780 km altitude, and 98.54° inclination. The heights and inclinations of these fragmentations, not to mention their recent occurrence with respect to the conducted BPE, are aspects suggesting that some of the mentioned clusters represent the debris stemming from these events.

7.2 Doppler velocity vs Time

How the observations are arranged with respect to Doppler velocity and time, are shown in Figure 7.3. Each of Figures 7.3a to 7.3d corresponds to a particular BPE. Although some observations are made outside the portrayed Doppler velocity interval, which extends from -2.5 to 2.5 km/s, their contribution is sparse to the overall population. The majority of the observations have velocities of $v_d \in [-1.5, 2.0]$ km/s, which we know from Figures 5.1 to 5.2, translates to inclinations approximately between 102° and 70° for circular orbits – expressed such that the lowest inclination matches the highest Doppler velocity.

01/18 – identifying potential SNAPSHOT debris.

In regard to the distribution observed in January 2018, Figure 7.3a, we notice the same distinctive train of *black* objects, as highlighted previously at $22 - 23$ hours after epoch, reappearing at a Doppler velocity of ≈ -0.25 km/s, and the other at $v_d \approx -1.1$ km/s.

Limiting our focus to the first, such low Doppler velocity serves as an indication that these fragments are close to an inclination of 90°. In [VKM+19] it was mentioned that this debris could originate from a further fragmentation of the SNAPSHOT satellite,[5] which was launched by the US military in 1965 carrying a nuclear power source. At several previous occasions, this spacecraft has been reported to shed debris [SS08]. The payload is residing in a near-circular orbit at heights between 1271 and 1318 km, with an inclination of $i = 90.28^\circ$ [Uni21]. Thus, since the measurements share similar characteristics, it is reasonable to believe that the observed debris cloud is connected to additional fragmentation of the SNAPSHOT-satellite.

04/19

As established in the prior, the Microsat fragments entered the observations between 9 and 14 hours after epoch, and made their reappearance 10 hours

---

[5] also called *OPS 4682* or SNAP-10A, international designator: 1965-027A, and NORAD ID: 1314 [Uni21].

later. This is clearly visible in Figure 7.3b. However, it seems appropriate to modify the relevant time intervals to 10–13 and 20–23 hours after epoch, respectively.

The observed Doppler velocities for the first passing of the debris clouds extend from -1.0 to about 0.5 km/s for the densest cluster, with some deviating from the range.

For the second pass, the majority of the observed velocities can be found within the same interval as the prior. However, at positive velocity values, the Microsat fragments are not equally prominent. Instead, the *black* objects exhibit a distribution somewhat similar to "an upside-down T". The *pillar* of this shape has the same velocity extension as in the first passing. While the *floor* of this reverse "T" extends along the x-axis from 20 to 23 hours after epoch, residing at a Doppler velocity of $\approx (-0.75)$ km/s. We cannot guarantee that each of the objects making up the floor of this fictitious "T", are Microsat fragments. But that the majority are related to this group seems probable. We know that the inclination of the parent body was 96.63°. This does not get significantly altered in a collision event, thus will the orbits of the debris have similar inclinations. Comparing this to the inclination lines in Figure 5.1, a Doppler velocity of -0.75 km/s is in good accordance with a circular orbit of 96.63° inclination.

However, this does not explain the significant Doppler velocity variation detected for the Microsat fragments. A reason for why Figure 5.1 does not adapt all that well to the debris cloud, is because the estimated inclinations are based on the assumption that we are dealing with circular orbits. But many of the debris trajectories are elliptic after the collision. A higher eccentricity implies a greater difference from the circular case. In turn these orbits will have a worse correlation with the inclination model.

What we can make of the different Doppler velocity distribution between the two clusters in Figure 7.3b, is that a lot more objects move away from the radar during the first pass compared to the second fly-by, due to the heavier appearance of positive velocity values. It seems evident that the relevant objects are situated in eccentric orbits.

06/19

Earlier we established that a lot of the Microsat fragments had de-orbited by June 2019. There is nothing from the distribution in Figure 7.3c that suggests otherwise. In fact, it is increasingly apparent that the perturbations have taken its toll on the dynamics of the debris cloud. That is, the overall eccentricity of the debris has been reduced. This is evident from the much bleaker presence of uncorrelated objects between Doppler velocities of −0.5 and 0.5 km/s, at the points in time when the Microsat fragments are observed. Many of the objects remaining in orbit seems to have an associated Doppler velocity of ≈ -0.8 km/s, as indicated by the heavy clusters observed at 9, and 19.5 hours after epoch. Thus, they can be interpreted as having near-circular orbits of an inclination equal to their parent body.

A nature which were not observed in April 2019 – which arise in June – is the many objects having Doppler velocity from −1.5 km/s to −1.0 km/s. Some are visible during the first crossings of the debris cloud, but the population within this interval is more abundant in the time frame from 18 to 20 hours after epoch. I.e. at 06:20–08:20 UTC on 7 June. Since these are the Microsat fragments, we should have captured some of them ≈ 10 hours earlier as well. Therefore, we need to investigate if some distinct differences stand out at around 9 hours, that do not reveal themselves by the time of the second pass. And it is. Specifically, the group of black objects with 0.5 ± 0.2 km/s Doppler velocities, and the fine line of uncorrelated detections making up a path "above" it, is a unique feature occurring in the first pass. If these positive velocities at the first observation, can be associated with the relevant negative velocities during the second detection, their respective objects are residing in eccentric orbits. Something that may explain this, is that these objects are, at 9 h, detected in they ascent towards the orbit apogee – observed as they "travel away" relative to the radar. Then, at ≈ 19 hours after epoch, the objects are observed as they head towards the radar – propagating with their course set for perigee.

04/21

The Doppler velocity vs time distribution from this year's campaign appears in Figure 7.3d. Previously we established an "area of interest" at 7.5, and 17.5 hours after epoch, due to the peculiar range arrangement associated with a group of detections. Interestingly, it seems to be some correlation between the inhabitants within these groups. At both instances, we observe distinct object crowds with Doppler velocities of -0.8 ∓ 0.1 km/s. If they represent two different transits of the same fragments, the small variation in radial velocity (≈ 0.1 km/s) imply that they are located in near-circular orbits. This can be confirmed by Figure 7.2(bottom) which indicates a rather small range difference for each individual object in the respective groups. For near-circular orbits the inclination estimates in Figure 5.2(bottom) should be rather accurate. From the associated range and velocity values of the group, we can determine their related orbital inclination – which is between 95° and 99°. Based on this, it is not improbable that these fragments could represent remnants from the Indian ASAT mission. However, it is important not to spiral into a logic of biased[6] research. Which is why we need to discuss what may contradict this theory.

We are at this stage familiar with the concept of diffusion, and that the Microsat-R got destroyed more than two years prior to the latest conducted BPE. Based on this, the coincidence of these fragments passing the radar beam within a period of only 45 minutes seems suspicious. After all they are at different ranges, and therefore have dissimilar orbital periods. Since the orbital periods at the relevant altitudes are in the range of 94–100 minutes, one should expect the objects to pass the beam during such time interval. At the same time, it may be the case that only a fraction of these fragments get detected, since the beam pointing direction is varying with the rotation of Earth. The second fact is that these black objects, occur alongside many red detections. Thus, it is likely that some of these uncorrelated detections are associated with the *clustered* observations of cataloged objects, which in turn may be linked to a more recent breakup event.

---

[6] A case of "we see what we want to see", without respecting the complete picture, is not a very scientific approach. If one give into such temptations, one may end up making invalid conclusions. The well-known conspiracy of people believing the Earth to be flat, is an outstanding example of this. Blinded by their own interpretations, they claim all facts disproving their theory, to be false.

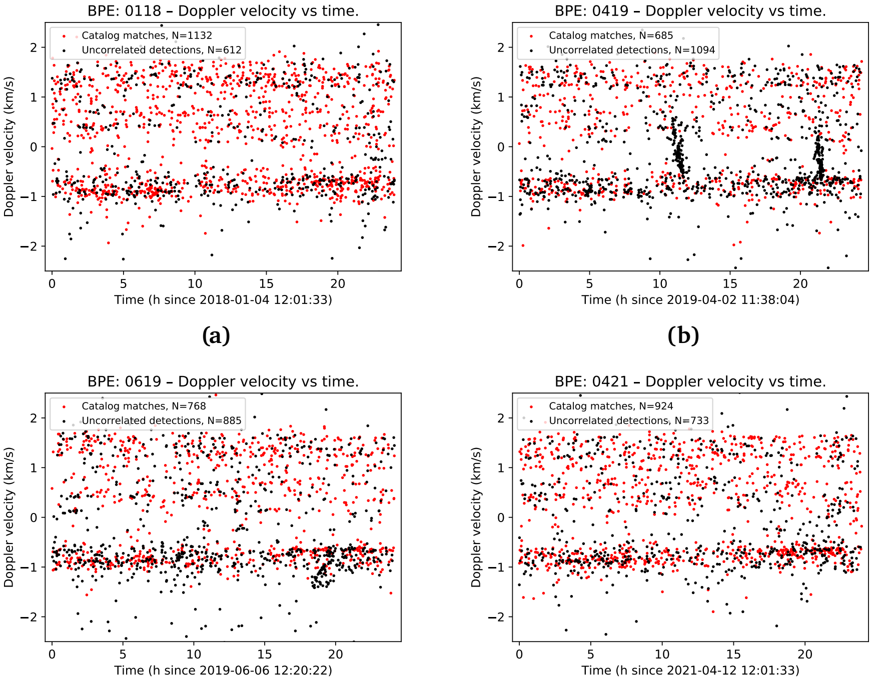

(a) (b)

(c) (d)

Figure 7.3: Distribution of beam-park observations as a function of detection time and Doppler velocity. Displayed in chronological order with respect to experiment date.

7.3 Range vs Doppler velocity

The object distributions are displayed with respect to range and Doppler velocity in Figure 7.4. Since this format is a compromise of the two former, we will limit the discussion for this one.

The overall pattern is the same in the sense that most objects are observed within distinct regions in the plots. Their locations along the figure axes are summarized in Table 7.1. For convenience we will in this section use the designations introduced in this table, and refer to these regions when identifying notable discrepancies.

In the plots representing the 2019 experiments, Figures 7.4b to 7.4c, we have colored potential Microsat fragments with blue color. This identification is based on the distributions encountered in the previous presented formats. Therefore, they should only be regarded as approximate values. This is because the criteria chosen to relate these objects are only based on graphical interpretation, which increases the uncertainty abruptly. Also, the *blue* points should only be regarded as a subcategory to the *uncorrelated detections*, i.e. they only make up a certain portion of the main class.

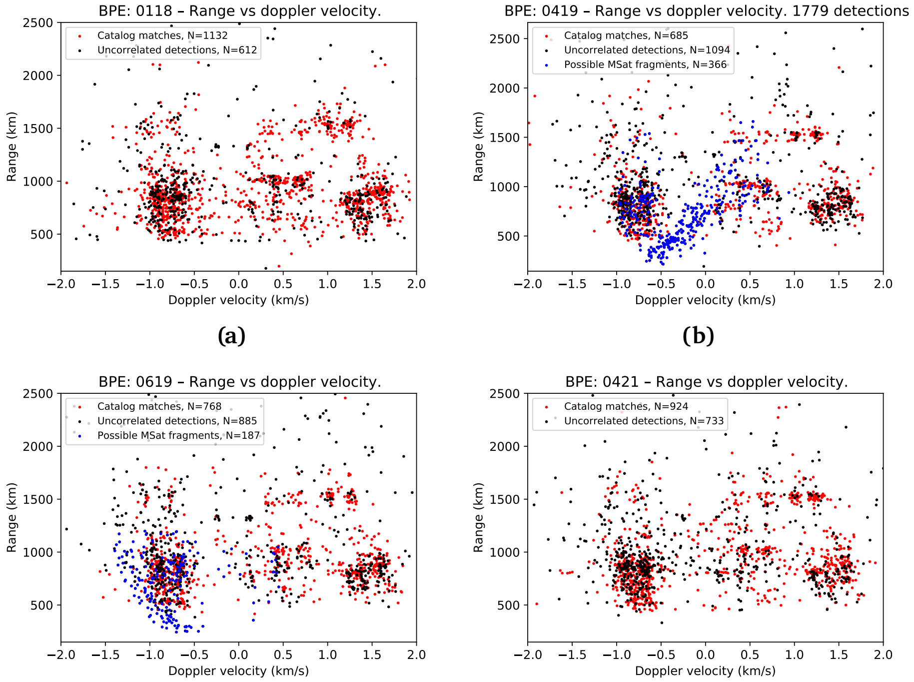

(a) **(b)**

(c) **(d)**

Figure 7.4: Object distribution as a function of observed range, and Doppler velocity. Plots are arranged in chronological order with respect to campaign date. Potential Microsat fragments are colored blue in 2019-plots.

Table 7.1: Most populated *regions* based on the "shared" distribution patterns appearing in Figure 7.4. The regions are sorted in descending order with respect to the amount of observations residing within it. The region designations reflect the location of the cluster, and chosen in the fashion as if the plot was a map; Southwest (SW), southeast (SE), central-east (CE), northeast (NE), and northwest (NW).

Region	Doppler span (km/s)	Range span (km)
SW:	$[-1.0, -0.5]$	$[500, 1000]$
SE:	$[1.2, 1.8]$	$[500, 1000]$
CE:	$[0.2, 0.8]$	$[950, 1050]$
NE:	$[1.0, 1.5]$	$[1450, 1550]$
NW:	$[-1.0, -0.5]$	$[1450, 1550]$

01/18

Figure 7.4a shows the distribution in January 2018. The majority belongs to one of the regions described in Table 7.1. It is not surprising that SW has the most dense distribution, since the observations contained here represent objects in Sun-synchronous orbits. The debris stemming from *Fengyun-1C* can be assumed to bring a solid contribution to this population. The other remarkable increase corresponds to inclinations between 70° and 74°, designated here as the SE-region. This region is among else the home of the *Cosmos-2251* fragments, partly explaining the significant amount of objects detected at these orbits.

In the previous section we argued that one of the clusters found in the observations, were potential debris from the SNAPSHOT satellite. These fragments are also discovered in this plot – likely responsible for the cluster appearing at a range of $\approx$ 1300 km, and a Doppler velocity of ≈ -0.25 km/s. This cluster is actually detected in all four experiments and are each time predominantly colored black. This indicates that many of the fragments in this cluster are smaller than 10 cm, and thus have not entered the catalog.

04/19

A general remark we can make of the distribution in April 2019, displayed in Figure 7.4b, is that the presence of cataloged objects is bleaker in all of the five *main* regions.

The Microsat fragments are potentially accounting for 366 of the detections. The distinctive signature we saw in the two other formats are combined here. This is manifested as a "staircase"-structure extending from $v_d \approx -0.6$ km/s and $R \approx 200$ km, to $v_d \approx 0.5$ km/s and $R \approx 1500$ km. There is also found a notable cluster of these fragments residing in the SW-region.

06/19

The properties of the Microsat fragments seems to have changed drastically during the two months from April to June 2019. Figure 7.4c shows that the Doppler velocity of most of the Microsat fragments have switched towards more negative values, that a lot of the eccentric orbits have begun their *circularization process* in the hands of the perturbations.

We see that 187 potential Microsat fragments remained in orbit by June. This alone implies that 179 of the objects de-orbited during the two months between the measurements, i.e. nearly 50%.

However, the range cutoff for categorizing the Microsat fragments were set to 1200 km in the making of the June plot, while it was 1500 km in the same case for April 2019. Thus, it may be some more of these objects located at higher altitudes.

04/21

The distribution from this year's campaign is somewhat similar to the one in 2018. This is clear when comparing Figure 7.4d with Figure 7.4a. No apparent trace of the Microsat fragments can be discovered here.

Earlier we introduced that we may have detected the debris associated with the recent fragmentations of the NOAA 17 satellite, as well as the YunHai 1-02. Their inclination values of $\approx 98.5°$ should put them into the SW-regions (see Table 7.1) in the scatter plot. Nothing Figure 7.4a contradicts this, and further investigation of these clusters could probably have identified them with certainty.

8

Conclusion

Most of the debris generated in the 2019 Anti-satellite mission have de-orbited during the two recent years. This is evident when comparing the observations made in April 2021 to the detections captured in 2019. Already during the two months elapsing from April to June 2019 a notable amount of the fragments had been removed from orbit.

In Subsection 3.4.3 we mentioned how the Indian DRDO stated that all of the fragments arising from the collision, were predicted to have decayed two months after the event [Lan19]. This does not align with our findings as the debris cloud still had a clear presence in the June 2019 results. Nor does it agree with the catalog [Uni21], since one of the Microsat fragments are reported to still orbit the planet. Additional of this debris may accompany it, but we have not obtained sufficient evidence that support this theory.

A good portion of the debris ended up in eccentric orbits following the impact. This is evident from the substantial range variation detected short time after the event. The altitude of the parent body was 280 km, however, the corresponding debris particles were observed all the way up to 1500 km in range. This indicates that even collisions taking place at relatively low altitudes may generate a debris cloud distributing across significant heights. Consequently, the ASAT test increased the collision threat for many spacecrafts in LEO. The risk remained for a longer period than estimated, due to the increased orbit lifetime of objects located at higher altitudes.

Following the results, we make one last remark about the relative difference in catalog matches, as summarized in Table 6.1. Evidently, the amount of unknown objects observed in the beam-park experiments seems to be coupled with the evolution of the Microsat fragments. This can be stated seeing how the total number of unknown objects has declined since 2019 to 2021. It does not provide a complete explanation for the relative change, but it serves as an indication of why the distribution of objects in polar orbit is slowly progressing towards the 2018 situation.

8.1 Proposals for future work

A breakup model of the collision would need to be implemented to study this debris cloud further. In turn the Microsat fragments would need to be simulated over the course of two years, to obtain a more detailed description of their evolution. Although beam-park observations provide valuable results, they need to be assisted by proper modelling in order to derive additional evidence towards a valid description about the current situation of the debris cloud. This is particularly important when trying to predict the orbital lifetime of the uncataloged objects.

Bibliography

[BB21] Aaron C. Boley and Michael Byers. Satellite mega-constellations create risks in Low Earth Orbit, the atmosphere and on Earth. *Scientific Reports*, 11(1):10642, 2021. `https://doi.org/10.1038/s41598-021-89909-7`.

[Chr] Christian Wolff. Parabolic Antenna. Webpage. `https://www.radartutorial.eu/06.antennas/Parabolic%20Antenna.en.html` (accessed on 27.05.21).

[EIS10] EISCAT Scientific Association. EISCAT ANNUAL REPORT 2010. 2010. `https://www.eiscat.se/wp-content/uploads/2016/11/EISCAT-report-2010-online.pdf`.

[EIS18] EISCAT Scientific Association. EISCAT ANNUAL REPORT 2017–2018. 2018. `https://eiscat.se/wp-content/uploads/2019/10/EISCAT-report-2017-2018.pdf`.

[ESA20a] ESA. Space debris by the numbers. Webpage, 2020. `https://www.esa.int/Safety_Security/Space_Debris/Space_debris_by_the_numbers`(accessed on 02.04.21).

[ESA20b] ESA. Types of Orbits. Webpage, 2020. `https://www.esa.int/Enabling_Support/Space_Transportation/Types_of_orbits` (accessed on 21.06.2021).

[ESA20c] ESA Space Debris Office. ESA's Annual Space Environment Report. issue 4.0, 2020. (Issue Date 29 September 2020 Ref GEN-DB-LOG-00288-OPS-SD).

[ESA21] ESA Space Debris Office. ESA'S Annual Space Environment Report. Issue 5.0, 2021. (Issue date 27 May 2021, Ref: GEN-DB-LOG-00288-OPS-SD).

[EvZ06] Charles Elachi and Jakob van Zyl. *Introduction to the Physics and*

Techniques of Remote Sensing. John Wiley & Sons, Inc., 2nd edition, 2006.

[GY15] Adrian V. Gheorghe and Daniel E. Yuchnovicz. The Space Infrastructure Vulnerability Cadastre: Orbital Debris Critical Loads. In *International Journal of Disaster Risk Science*, volume 6, pages 359–371. 2015.

[Hou11] Houghton, John M. Spacecraft structures. In Fortescue, Peter and Graham, Swinerd and Stark, John, editor, *Spacecraft Systems Engineering*, chapter 8, pages 251–287. John Wiley & Sons, Ltd, 4th edition, 2011.

[Int20] Interagency Space Debris Coordination Committee (IADC). Space Debris Mitigation Guidelines. IADC–02–01(Revision 2), 2020.

[JKLAM01] N.L. Johnson, P.H. Krisko, J.-C. Liou, and P.D. Anz-Meador. Nasa's new breakup model of evolve 4.0. *Advances in Space Research*, 28(9):1377–1384, 2001. `https://doi.org/10.1016/S0273-1177(01)00423-9`.

[JSL+08] Nicholas L. Johnson, E. Stansbery, J.-C. Liou, M. Horstman, C. Stokely, and D. Whitlock. The characteristics and consequences of the break-up of the fengyun-1c spacecraft. *Acta Astronautica*, 63(1):128–135, 2008. Touching Humanity - Space for Improving Quality of Life. Selected Proceedings of the 58th International Astronautical Federation Congress, Hyderabad, India, 24-28 September 2007. `https://doi.org/10.1016/j.actaastro.2007.12.044`.

[KCP78] Donald J. Kessler and Burton G. Cour-Palais. Collision frequency of artificial satellites: The creation of a debris belt. *Journal of Geophysical Research: Space Physics*, 83(A6):2637–2646, 1978.

[Kli10] Heiner Klinkrad. *Space debris*. Wiley Online Library, 2010.

[KVK+19] D Kastinen, Juha Vierinen, Johan Kero, S Hesselbach, Tom Grydeland, and Holger Krag. Next-generation Space Object Radar Tracking Simulator: SORTS++. In T. Flohrer, R. Jehn, and F. Schmitz, editors, *1st NEO and Debris Detection Conference*, volume 1. ESA Space Safety Programme Office, 2019. `https://conference.sdo.esoc.esa.int/proceedings/neosst1/paper/465`.

[Lan19] Marco Langbroek. Why India's ASAT Test Was Reckless. *The Diplomat*, Apr 2019. `https://thediplomat.com/2019/05/why-indias-`

asat-test-was-reckless/ (accessed on 28.06.2021).

[MLHV02] J. Markkanen, M. Lehtinen, A. Huuskonen, and A. Väänänen. Measurements of small-size debris with backscatter of radio waves. 2002.

[NAS12] NASA. *Orbital Debris Management & Risk Mitigation*. NASA Academy of Program/Project and Engineering Leadership, 2012.

[Nat07] National Aeronautics and Space Administration Orbital Debris Program Office (NASA ODPO). *Orbital Debris Quarterly News*, 11(2), April 2007.

[Nat09] National Aeronautics and Space Administration Orbital Debris Program Office (NASA ODPO). *Orbital Debris Quarterly News*, 13(2), April 2009.

[Nat12] National Aeronautics and Space Administration Orbital Debris Program Office (NASA ODPO). *Orbital Debris Quarterly News*, 12(3), July 2012.

[Nat16] National Aeronautics and Space Administration Orbital Debris Program Office (NASA ODPO). *Orbital Debris Quarterly News*, 20(1–2), April 2016.

[Nat19a] National Aeronautics and Space Administration Orbital Debris Program Office (NASA ODPO). *Orbital Debris Quarterly News*, 23(3), August 2019.

[Nat19b] National Aeronautics and Space Administration Orbital Debris Program Office (NASA ODPO). *Orbital Debris Quarterly News*, 23(1–2), May 2019.

[Nat21] National Aeronautics and Space Administration Orbital Debris Program Office (NASA ODPO). *Orbital Debris Quarterly News*, 25(2), June 2021.

[PK19] Rajat Pandit and C. Kumar. India shoots into star wars club. *The Times of India*, Mar 2019. https://timesofindia.indiatimes.com/india/india-shoots-into-star-wars-club/articleshow/68605713.cms(Published 28.03.2019).

[SIA20] SIA. State of the Satellite Industry Report, 2020.

`https://sia.org/news-resources/state-of-the-satellite-industry-report/` (accessed on 25.04.21).

[Sko08] Skolnik, Merrill I. *Radar Handbook*. The McGraw-Hill Companies, 3rd edition, 2008.

[SS08] C.L. Stokely and E.G. Stansbery. Identification of a debris cloud from the nuclear powered SNAPSHOT satellite with haystack radar measurements. *Advances in Space Research*, 41(7):1004–1009, 2008. `https://doi.org/10.1016/j.asr.2007.03.046`.

[ST11] Ray E. Sheriff and Adrian R. L. Tatnall. Telecommunications. In *Spacecraft Systems Engineering*, chapter 12, pages 395–437. John Wiley & Sons, Ltd, 4th edition, 2011.

[Sta21] Statistisk Sentralbyrå. De 100 mest folkerike kommunene. Webpage, 2021. `https://www.ssb.no/befolkning/artikler-og-publikasjoner/norges-100-mest-folkerike-kommuner?tabell=446939`(accessed on 08.04.21).

[UJO20] Marit Undseth, Claire Jolly, and Mattia Olivari. Space sustainability: The economics of space debris in perspective. *OECD Science, Technology and Industry Policy Papers*, (87), Apr 2020. OECD publication, `https://doi.org/10.1787/a339de43-en`.

[Uni21] United States Space Command. Satellite Catalog, 2021. `https://www.space-track.org` (accessed on 13.04.2021).

[UNO21] UNOOSA and ESA. UNOOSA and ESA space debris infographics and podcasts. Webpage, 2021. `https://www.unoosa.org/oosa/en/informationfor/media/unoosa-and-esa-release-infographics-and-podcasts-about-space-debris.html` (accessed on 11.04.21).

[VKM+19] Juha Vierinen, D Kastinen, Jussi Markkanen, Tom Grydeland, Johan Kero, A Horstmann, S Hesselbach, C Kebschull, Elisabeth Røynestad, and Holger Krag. 2018 Beam-park observations of space debris with the EISCAT radars. 2019.

[VMK+17] J. Vierinen, J. Markkanen, H. Krag, J. Siminski, and A. Mancas. Use of EISCAT 3D for Observations of space debris. In Flohrer, T. and Schmitz F., editor, *7th European Conference on Space Debris*, volume 7, Darmstadt, Germany, 18–21 Apr 2017. ESA Space Debris Office. `https://conference.sdo.esoc.esa.int/proceedings/sdc7/paper/350`.

[Wan05] Gudmund Wannberg. Review of the EISCAT Radar Hardware, 2005. Powerpoint from the EISCAT Radar School in Kiruna, August 15-26.

[Wor21] Worldometer. Countries in the world by population (2021). Webpage, 2021. `https://www.worldometers.info/world-population/population-by-country/`(accessed on 08.04.21).